

博士論文

Geological studies on small-scale surface features of Mars and Phobos
based on high-accuracy digital elevation models

(高精度数値標高モデルに基づく
火星およびフォボス表面の小地形に関する地質学的研究)

逸見 良道

**Geological studies on small-scale surface features of Mars and Phobos
based on high-accuracy digital elevation models**

by

Ryodo Hemmi

A dissertation submitted to the Graduate School of Engineering of
the University of Tokyo

Tokyo, Japan
September 2021

Dedication

This thesis is dedicated to my beloved parents, sister, and her family, who supported me physically and mentally. My dad, Ryoan, who encouraged me all the time and passed away in March 2021, is one of the crucial reasons that made me pursue my studies.

Acknowledgment

During the past ten years, I have worked on this thesis, many people helped me in every way. I would like to express my deepest appreciation to my supervisor, Prof. Hideaki Miyamoto, for supporting me in every respect. My sincere thanks are due to the committee: Dr. Akihiro Nakao, Dr. Kentaro Nakamura, Dr. Kazuo Yonekura, and Dr. Tomokatsu Morota.

I would like to thank the colleagues in the Miyamoto laboratory, Dr. Takafumi Niihara, Dr. Hong Peng, Dr. Naoyuki Hirata, Dr. Hiroshi Kikuchi, Dr. Luyuan Xu, Dr. James M. Dohm, and Dr. Reid Parsons for all you have done.

A special thanks to Trent Hare, Elpitha Howington-Kraus, Dr. Ross Beyer, Dr. Oleg Alexandrov, Zachary Moratto, Dr. Chris H. Okubo, Dr. Dorothy Oehler, and the members of JAXA's Hayabusa2, MMX, and SELENE-R missions for their helpful comments and discussions. I would also like to appreciate the NASA Planetary Data System, MRO HiRISE Science Team, NASA Ames Stereo Pipeline members, U.S. Geological Survey Astrogeology Science Center for their public release of high-quality data sets and open-source software, which are essential for the achievement of my research objectives.

This research would not be possible without supports from TOKYO DOME CORPORATION, JAXA, Disaster Prevention Technology Co., Ltd.

Abstract

Based on recent planetary geological studies, the presence and redistribution of regolith and (near-)surface water is considered to be a major factor in the surface processes of extraterrestrial bodies. This strongly affects the designs, operations, and goals of planetary exploration programs (e.g., development of human bases, mining of resources, search for life, etc.).

Especially for Mars, a future human exploration target, it is important to understand more about the processes of water mass localization and supply to the surface. JAXA's Martian Moons eXploration (MMX), a sample return mission scheduled for launch in 2024, will require an assessment of the stability of the landing sites and their scientific value.

This thesis aims to relate the understanding of the formation of small-scale geological features on Mars and its satellite Phobos to the selection and evaluation of future landing exploration sites in the solar system. This is expected to significantly improve our ability to select sites conducive to future human and life exploration and to constrain the nature of the regolith on the surface of planetary satellites.

While various aspects should be considered to complete the exploration, this thesis focuses on two points: (1) to identify the topography related to the current reservoir at a depth of several meters to several tens of meters, and (2) to establish a method to accurately evaluate the surface condition of the regolith, which is critical for the safety of the landing site.

Here I propose that these can be achieved by developing a digital elevation model (DEM) of the terrain of interest and measuring its morphology. The formation history of hundreds of meter-scale topographic features on Mars and Phobos is more difficult to understand than that of large-scale terrain. This is due to the small number of high-resolution remote sensing data and publicly available DEMs, the limited number of in-situ observations by landing missions, and incomplete models of regolith dynamics.

The work shows that pitted mounds of several hundred meters in size in the southern highlands and northern lowlands of Mars and small craters of less than 1 km in diameter on the surface of Phobos can be morphometrically measured with high accuracy by generating a high-precision digital elevation model (DEM). After preparing a reference DEM, appropriate image processing, bundle adjustment, and stereo-photogrammetry were applied to stereo pairs of telescopic line-scan (push broom) images of Mars orbiters.

This thesis shows that pitted mounds of several hundred meters in size in the southern highlands and northern lowlands of Mars and small craters of less than 1 km in diameter on the surface of Phobos can be morphometrically measured with high accuracy by generating high-precision DEMs. After preparing a reference DEM, appropriate image processing, bundle adjustment, and stereo-photogrammetry were applied to stereo pairs of telescopic line-scan (push broom) images taken by the Mars orbiters.

By comparing the results of topographic measurements of pitted mounds on Mars with those of similar terrains (e.g., pingos, rootless cones, tuff cones, cinder cones, etc.), we were able to constrain the origin of the pitted mounds. The application of crater retention ages allowed us to consider the geological history of the area of interest and its relationship to the stress field. The Bingham fluid model and the mud conduit model were used to test the consistency of mudflow behavior and the depth of the mud source layer, respectively.

The formation of mud volcanoes suggests that there was (or is) a water source directly beneath them, and if they were submarine mud volcanoes, they support a paleoenvironment suitable for life. Mud volcanic areas in the southern highlands, which are scarce compared to the northern lowlands, can be explained by the concentration and over-compaction of liquid water associated with local fault movement. Further analysis is needed to assess the future astrobiological potential and volume of water resources.

Since the surface of Phobos became observable at high resolution, more than 9000 impact craters with diameters greater than 50 m have been identified, as well as grooves and pit chains. The model of impact ejecta re-impacting on Phobos suggested the existence of regolith layers, but the detailed subsurface structure and nature of the regolith are uncertain.

No significant difference was observed in the measured depth-diameter ratio between the blue (relatively fresh) unit and the red (older) unit for craters of several hundred meters in diameter. This indicates that the degree of degradation of small craters in Phobos due to regolith behavior is independent of geological unit (or geological age). The flat or uplifted features at the crater floor suggest a regolith layer and a higher-strength layer directly beneath it, and further evaluation of landing stability on a global scale using high-precision and high-resolution DEM is necessary for MMX landing site selection.

Table of Contents

Dedication.....	ii
Acknowledgment.....	iii
Abstract.....	iv
Chapter 1 General Introduction	1
1.1 Planetary Geology and Space Exploration	1
1.2 Significance of Planetary Topographic Mapping	1
1.3 Topographic Mapping of the Martian Surface.....	3
1.4 Overview of Existing HiRISE DEMs.....	6
1.5 Topographic Mapping of Phobos	9
1.6 Objectives	10
Chapter 2 Extraction of High-accuracy DEMs.....	11
2.1 Significance of Bundle Adjustment and Manual Refinement	11
2.2 Processing of HiRISE Stereo Imagery of Mars	11
2.3 Processing of HiRISE Stereo Imagery of Phobos.....	17
Chapter 3 Distribution, Morphology, and Morphometry of Circular Mounds in the Elongated Basin of Northern Terra Sirenum, Mars.....	21
Chapter 4 High-resolution Topographic Analyses of Mounds in Southern Acidalia Planitia, Mars: Implications for Possible Mud Volcanism in Submarine and Subaerial Environments.....	37
Chapter 5 Morphology and Morphometry of Sub-kilometer Craters on the Nearside of Phobos and Implications for Regolith Properties.....	57
Chapter 6 Summary and Outlook	66
6.1 Summary.....	66
6.2 Outlook	67
References for Chapters 1, 2, and 6.....	68
Appendix	73

Chapter 1

General Introduction

1.1 Planetary Geology and Space Exploration

Planetary bodies (e.g., terrestrial planets, satellites, dwarf planets, asteroids, comets, Kuiper belt objects, etc.) have attracted scientists in search of the origin and evolutionary history of the solar system. Planetary surfaces are commonly covered by geological landforms (e.g., mountain ranges, volcanoes, channels, distributary fans, impact craters, etc.). Most of them are related to lateral/vertical redistribution of regolith and (near-)surface water affected by gravity, atmospheric interaction, tectonic stress, solar activity, geothermal activity, impact cratering, etc. (Melosh, 2011). In particular, Mars has a variety of morphologic characteristics suggestive of aqueous processes on a regional and local scale (e.g., outflow channels, distributary fans, sedimentary mounds, sedimentary textures, etc.) (Carr, 2007). Recent high-resolution spectral observations have identified dense distributions of water-related materials (e.g., sulfates detected within the chasmata of Valles Marineris) with high probability (Ehlmann and Edwards, 2014). In the next twenty years, these features will be of great interest as the primary exploration sites of robotic/human missions to Mars for life-detection tests and resource mining/utilization (International Space Exploration Coordination Group, 2018).

Martian moon Phobos, the target body of Japanese Martian Moons eXploration (MMX) for launch in 2024, can be a candidate sampling site of materials responsible for the origin and evolution of Mars. This is because the in-situ formation scenario suggests the Phobos is originated from the building blocks or juvenile crust/mantle constituents of proto-Mars (Usui et al., 2020), and particles ejected from past large impacts on Mars would have reached the regolith of Phobos (Ramsley and Head, 2013). Thus, the relatively fresh-looking, blue unit of Phobos' nearside is considered to be the primary target of MMX landing/sampling operation.

While sample acquisition from these localized surface/subsurface features on planetary bodies is of great importance in understanding their origins and evolutionary histories, the past landing/roving/sampling sites were selected in terms of safety and guidance constraints, (e.g., slope distributions within a three-sigma landing ellipse, rather than scientific interest. One of the major reasons for this is the large uncertainty about topographic irregularities within areas of interest (from hundreds of kilometers down to the lander/rover scale).

1.2 Significance of Planetary Topographic Mapping

Topographic mapping is a first-choice approach that quantitatively characterizes their geomorphologies at local, regional, and global scales. Global and local topography offer important information about planetary geology (e.g., roughness, geomorphological features, geopotential height, bulk density), geophysical modeling (thermophysical model, hydraulic model, photometric model, radar model), and photogrammetric processing and geographic information system (e.g., orthorectification, terrain shading, three-dimensional visualization). Above all, many of these applications require topographic maps to have as high spatial resolutions and/or vertical accuracies as possible.

Topography (or elevation) data, as well as imaging and laser ranging data, is also in great demand for mission planning/operation (e.g., landing site selection, rover landing positioning, hazard detection, autonomous Guidance, Navigation, and Control (GNC) system, etc.) (Johnson et al., 2015; Johnson et al., 2008). Planetary landing is highly challenging today, as exemplified by the recent landing failures (e.g., the Rosetta Philae lander in 2014, the ExoMars Schiaparelli lander

in 2016, the Israeli Beresheet lander in 2019, the Chandrayaan-2 Vikram lander in 2019, and so forth). Though different causes are responsible for these failures (e.g., spacecraft malfunction, inadequate software, mismanagement), highly accurate topographic maps, with the help of its autonomous navigation technology, can contribute to improving hazard assessment and avoiding topographic obstacles during spacecraft descent/landing phases (e.g., the Mars 2020's Terrain Relative Navigation (TRN) system (Ferguson et al., 2020), Hayabusa2's pinpoint touchdown operation (Kikuchi et al., 2020)).

The three-dimensional topographic information about planetary surfaces is usually represented by either gridded digital elevation models (DEMs, also called "digital terrain models" (DTMs)) for a specific region of interest or numerical shape models for irregularly shaped small bodies. In general, DEMs (and shape models) are generated using the well-known photogrammetric techniques or ranging instruments, including stereo-photogrammetry, photoclinometry, stereo-photoclinometry (SPC), shape-from-shading (SfS), structure-from-motion (SfM), limb profile and occultation observations, radar-clinometry, radar interferometry, radar or laser altimetry by spacecraft near its target and/or ground-based observation, or a combination of them (Hargitai et al., 2019). The applicability of these methods depends on target surface conditions (e.g., the presence/absence of hazes, clouds, or thick atmospheres), the quality/quantity of obtained data (e.g., frame scan or line scan arrays, spatial resolutions, signal-to-noise ratios, the number of images), and other available resources (e.g., electrical power system, data sampling rate, data transfer rate, etc.).

Contrary to the extraterrestrial topographic mapping, topographic maps of the Earth have been commonly generated using active sensors, such as spaceborne/airborne interferometric synthetic-aperture radar (InSAR) (e.g., Shuttle Radar Topography Mission), satellite radar altimeter, and spaceborne/airborne/terrestrial laser scanning (also called light detection and ranging (lidar)) (e.g., Slatton et al., 2007; Tarolli, 2014). Such sensors are advantageous over optical stereo mapping in terms of vertical accuracy (as high as ~ 2.5 cm (Ulaby et al., 2014)), the capability of filtering vegetation/cloud cover, the detectability of low-contrast, shadowed, or smooth featureless areas, etc (e.g., Farr et al., 2007).

Nevertheless, Earth observation satellite/airborne linear pushbroom or frame images are used for DEM generation because they can provide corresponding orthophotos and that their ground sampling distances are generally better than radar/lidar footprint intervals/sizes. Their ground-to-image translation is estimated by using either the rigorous sensor models (RSM; represented by instrument/body rotational matrices) or the rational functional model (RFM; represented as rational polynomial coefficients). Although the RSM has high accuracy for triangulation and physical meaning (i.e., satellite position/attitude), the RFM is preferred for stereo (or tri-stereo) images acquired by pushbroom imagers (e.g., Aati and Avouac, 2020; Jacobsen and Topan, 2015) owing to its efficiency (i.e., computational speed), generality (i.e., sensor-agnostic model), and confidentiality (i.e., no physical meaning). In other words, the RSM is considered to be not practical to solve different exterior orientation parameters of individual scan lines at different observation times (Geng et al., 2019). The RSM is used to implement the bundle adjustment of a set of frame images taken at different camera poses by an uncrewed aerial vehicle during the SfM and multi-view stereo (SfM-MVS) approach (Carrivick et al., 2016).

Most of the abovementioned techniques utilize precise orbit (position and attitude) information determined by the global positioning system (GPS) and/or ground control points (GCPs) provided via either total station or differential GPS surveys. This cannot be simply applied to planetary (extraterrestrial) remote sensing images due to low-accuracy spacecraft position and attitude measurements with limited ground control data. Thus, as discussed in Chapter 2, the RSM is applied to the planetary pushbroom images using specific pushbroom sensor models, as well as the bundle adjustment and triangulation (Geng et al., 2019; Geng et al., 2020).

1.3 Topographic Mapping of the Martian Surface

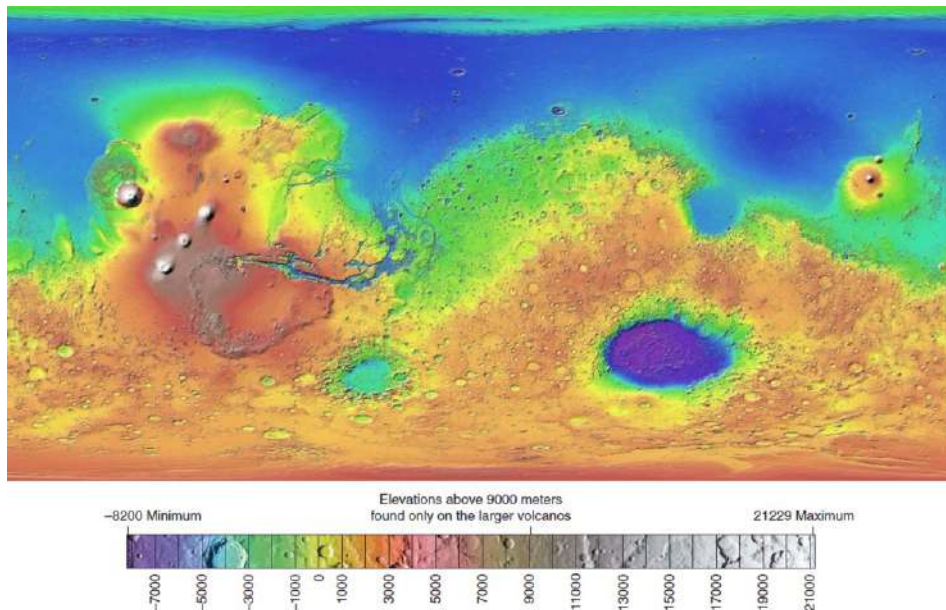


Figure 1.1 MOLA global elevation map (Image credit: USGS Astrogeology Science Center/Goddard Space Flight Center/NASA).

In the case of Mars, the National Aeronautics and Space Administration (NASA) and the European Space Agency (ESA) have led the study of its surface topography from global to local scales by remote sensing within the last decades. Contrary to the early estimates from the occultation measurements of the Mariner 9 and Viking orbiters and Earth-based radar measurements during the 1970s, the Mars Orbiter Laser Altimeter (MOLA) aboard the NASA's Mars Global Surveyor (MGS) obtained, for the first time, the global-scale surface topography of Mars (Smith et al., 2001; Smith et al., 1999), which is currently used as the basis for the spatial analysis of Mars (Figure 1.1).

Each of the MOLA footprints with across-track shot spacings of ~ 4 km (on average at the equator) is composed of ~ 168 -m-diameter laser spots spaced ~ 300 m apart, with vertical and horizontal accuracies of ~ 1 m and ~ 100 m, respectively (Neumann et al., 2001; Smith et al., 2001). More than 600 million measurements, collected between 1999 and 2001, have been adjusted for consistency, interpolated, and merged into DEMs gridded at ~ 463 m/pixel (128 pixels/degree; gridded at ~ 115 m/pixel or 512 pixels/degree for the polar regions). Based on the MOLA topography, the Martian gravitational potential and its geodetic parameters (e.g., mean radius, mean equatorial radius, mean polar radius, etc.) were defined (Smith and Zuber, 1998). This definition has led to the International Astronomical Union (IAU) definitions of the geographic coordinate system (GCS) and the projection parameters of both the reference spheroid and ellipsoid of Mars (known as "Mars IAU 2000"), which are widely used in the GIS interface. The MOLA DEM data are publicly available as the MOLA Mission Experiment Gridded Data Records (MEGDRs) in the NASA Planetary Data System (PDS), as well as the individual MOLA footprints (called the Precision Experiment Data Records (PEDRs)).

From early 2004 to the present, the High Resolution Stereo Camera (HRSC) aboard the ESA's Mars Express (Neukum and Jaumann, 2004) has obtained relatively high-resolution images (down to 10-m ground pixel scale) during individual orbits. This HRSC system is composed of one nadir-looking sensor with a nominal ground resolution of 12.5 m at periapsis (without pixel

binning) and eight off-nadir sensors (two photometry channels with 2×2 pixel binning, two stereo channels with 2×2 pixel binning, and four color-imaging channels (blue, green, red, and infrared) with 4×4 or 8×8 pixel binning), which are designed to produce higher-level products simultaneously at a single observation time. HRSC stereo-derived DEMs, called the HRSC DTMs with a horizontal grid size of down to 50 m, were co-registered to the MOLA DEM (Gwinner et al., 2010; Gwinner et al., 2009). As of 2017, the HRSC imagery at ~ 10 – 20 and < 100 m/pixel resolution has achieved $\sim 76\%$ and $\sim 98\%$ of the surface of Mars, respectively (Kirk et al., 2017). Their associated HRSC DTMs with post spacings of 50 m or worse, however, have been produced for about 40% of the planet with the use of NASA Video Image Communication and Retrieval (VICAR) (Gwinner et al., 2009; Scholten et al., 2005).

In contrast, the number of DEMs ever produced at grid spacings ~ 20 m or better is quite limited. The orbital stereo images at ground pixel sizes better than those of HRSC images have been obtained by the three different cameras on the two Mars spacecraft (the MGS and the NASA's Mars Reconnaissance Orbiter (MRO)):

- MGS narrow-angle Mars Orbiter Camera (MOC-NA; 1997–2006) (Malin et al., 1992; Malin and Edgett, 2001),
- MRO High Resolution Imaging Science Experiment (HiRISE; 2006–present) (McEwen et al., 2007).
- MRO Context Imager (CTX; 2006–present) (Malin et al., 2007),

MOC DEMs (typically 10 m/post) were derived from the MOC-NA images (typically > 3 m/pixel) by stereophotogrammetry and photoclinometry (Kirk et al., 2003; Kirk et al., 2002). In reality, however, owing to large spatiotemporal uncertainties in surface albedo and atmospheric conditions (Kirk et al., 2003), during the last fifteen years, photoclinometry has become less common than stereo-photogrammetry for topographic mapping of Mars. Additionally, the MOC DEMs are not publicly accessible and the number of MOC-NA stereo pairs is quite limited. Instead, most of the MOC coverages are overlapping with the subsequent CTX and HiRISE coverages.

The MRO HiRISE camera is a push-broom telescope with a 50-cm-diameter aperture and an effective focal length of 12 meters, which enables the acquisition of high-resolution orbital images. Its small instantaneous field of view (1 microradian per pixel) offers a ground sampling dimension down to ~ 25 – 35 cm at a nominal altitude of ~ 300 km. A focal plane of the HiRISE camera (Figure 1.2a) is constructed from fourteen color-filtered charge-coupled device detectors (ten RED CCDs: ~ 570 – 830 nm, two BG CCDs: BG: ~ 430 – 580 nm, and two NIR CCDs: ~ 790 – $1,000$ nm in wavelength) (McEwen et al., 2007). Individual CCD filter holds 128 time delay integration (TDI) elements in the along-track direction, which increase an effective exposure time to provide high signal-to-noise ratios even during hazy or dusty atmospheric conditions. The RED CCDs, each with a width of 2048 pixels, overlap each other, which constitutes an effective swath width of $\sim 20,000$ pixels (10% narrower at present due to the failure of the RED9 electronics since August 2011 (McEwen and the HiRISE Science and Operations Team, 2018)), and gives a ground swath with of ~ 6 km (Figure 1.2b). HiRISE stereo observation can acquire two different orbital images capturing the same target with a sufficient convergence angle (i.e., a pair of a nadir image and a $> 10^\circ$ off-nadir image observed at least two weeks apart).



Figure 1.2 Spatial relationship between HiRISE CCD imagers and their resulting images. (a) HiRISE focal plane array (Eliason et al., 2007). (b) Example of ten RED CCD image footprints (colored rectangles) acquired at a single HiRISE orbit. The map-projected view is rendered using ISIS3's *qmos*.

The MRO CTX camera, with a single focal plane of a visible panchromatic (500-700 nm in wavelength), 5000-pixel-wide CCD, is designed to obtain ~30 km-wide, ≥40-km-long images with a ground pixel scale of 5–6.5 m (Malin et al., 2007). Both the CTX and HiRISE instruments located in a relatively fixed position operate simultaneously, which allows a HiRISE image to be map-projected in the middle of its corresponding CTX imaging area.

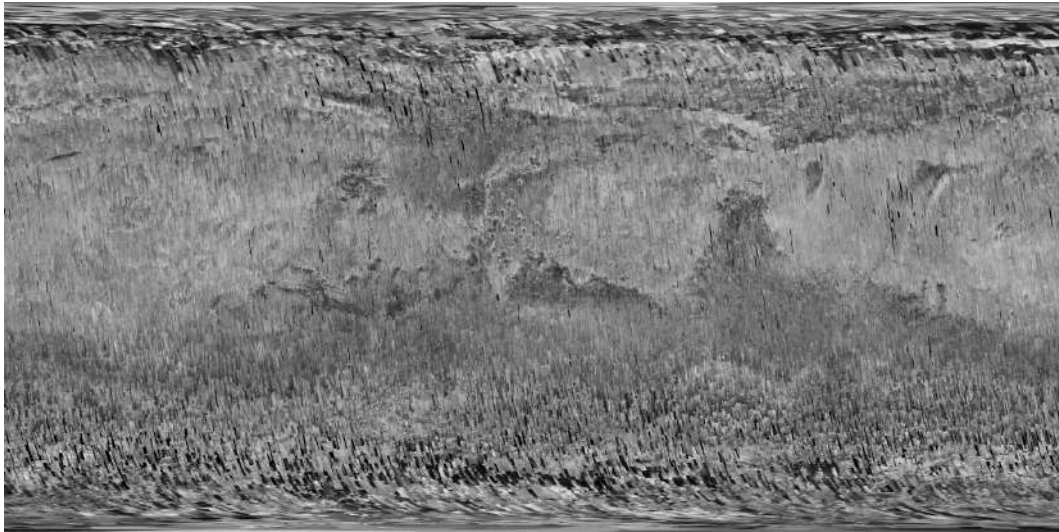


Figure 1.3 Global coverage of nearly 90,000 CTX images acquired between 2006 and 2017 (Image credit: NASA/JPL-Caltech/MSSS).

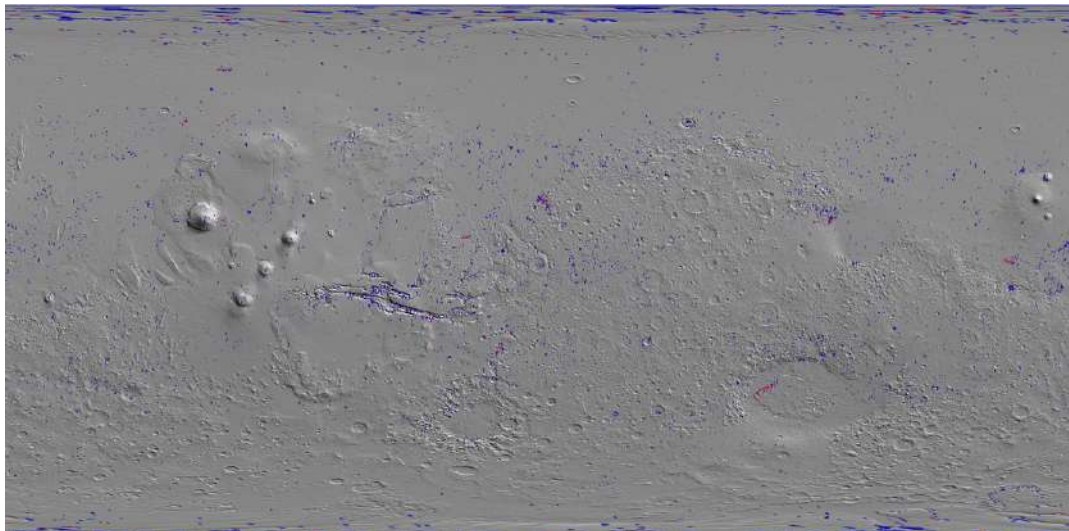


Figure 1.4 Spatial footprints of 13,007 HiRISE stereo-pair images (blue rectangles) and 731 HiRISE DTMs (red rectangles) that are publicly available as of September 2020. Background is the MOLA shaded relief map.

The public availability of high-resolution (better than ~ 20 m/post) DEMs of Mars is constrained by the population of the available stereo pairs of both HiRISE and CTX images. In reality, the multiple CTX observations cover more than 60% surface area as of March 2017 (Figure 1.3), and more than 6,300 HiRISE stereo pairs (<https://www.uahirise.org/stereo/>) are acquired as of 2020 (Figure 1.4). However, at present, there are quite a few official CTX stereo-derived DEMs generated solely for InSight/Mars2020 landing sites and Kasei Valles (Ferguson et al., 2020; Ferguson et al., 2017) (available at <https://planetarymaps.usgs.gov/mosaic/>), and the only ~ 700 official HiRISE stereo DEMs, so-called “HiRISE Digital Terrain Models (HiRISE DTMs)” (Kirk et al., 2008) (available at <https://www.uahirise.org/dtm/>).

1.4 Overview of Existing HiRISE DEMs

Contrary to large-scale morphological features on Mars (e.g., global dichotomy, volcanoes, impact basins, valley networks, outflow channels, paleo shorelines, etc.), most of the major

geological activities that occurred between the recent past and the present (around the Amazonian era) are spatially limited to several hundreds of meters or less. High-resolution (better than several meters per pixel) DEMs are necessary for their morphological analysis. My review article (Hemmi et al., 2018) described the details of the recent (Amazonian-aged) geological features and present-day surface changes on Mars (see Appendix).

The HiRISE DTMs, produced by the University of Arizona (UofA) and the U.S. Geological Survey (USGS) Astrogeology Science Center, are mostly gridded at 1 m/post ($\times 3$ image pixel size; 2 m/post for 2×2 binned images). They have ever contributed to the better understanding of Martian surface evolution, such as stratigraphy (Lewis et al., 2008), current aeolian activity (Bridges et al., 2012), seasonal changes in slope features (McEwen et al., 2011), identification of small mounds (e.g., Hemmi et al., 2018; Miyamoto et al., 2016), as well as the planning and operating spacecraft missions including spatial analysis on candidate landing and roving sites (e.g., Bhardwaj et al., 2019; Chojnacki et al., 2018; Fergason et al., 2017; Kirk et al., 2020) and rover localization (e.g., Tao et al., 2016).

HiRISE DTMs are created by two major pipelines: data pre-processing through the USGS's open-source software, Integrated Software for Imagers and Spectrometers Version 3 (ISIS3), with the help of PERL scripts; and stereo processing via commercial software, SOCET SET ($\text{\textcircled{R}}$ BAE Systems). A series of the pre-processing steps include a collection of position and orientation data of each HiRISE CCD, distortion correction of the HiRISE focal plane, mosaicking of each HiRISE CCD image, jitter evaluation, MOLA MEGDR/PEDR extraction, and data formatting for SOCET SET.

The stereo processing (including image matching, bundle adjustment, control to MOLA tracks, DTM extraction, terrain editing) is executed by the capabilities of the SOCET SET. Even though the SOCET SET is robust for terrain extraction from planetary stereo images, severe elevation uncertainties exist in the SOCET SET DEMs (Kirk et al., 2008). Variation in vertical accuracy results from the extraction of GCPs from sparse MOLA shots and low-resolution MOLA DTMs, in which horizontal spacings (463 m to ~ 4 km) are more than three orders of magnitude larger than the HiRISE ground pixel size (~ 30 cm). Furthermore, horizontal uncertainties stem from changes in cartographic scale (scale distortion increases with the increase of the distance from a projection center, standard parallel).

Moreover, there are relative elevation uncertainties (mostly ascribed to severe artifacts within DEMs) because the stereo matching algorithm fails to find pixels in featureless or shadowed areas (Figure 1.5). The arrangement of the HiRISE RED CCDs (Figure 1.2) is affected by spacecraft jitter, which results in misalignments among the RED CCD images. This is responsible for the linear artifacts that frequently occurred within the resultant DEM (Figure 1.5).

Furthermore, it should be noted that it takes 1—2 weeks per DTM production (plus a six-month proprietary period before its public release) for photogrammetry experts and trained researchers to accomplish the operations by using the roughly \$70,000 SOCET SET workstation (Kirk et al., 2009), which is out of reach for many researchers. In-house (not released through the PDS) MOC-NA DEMs and CTX DEMs have been generated using the SOCET SET workstation within the USGS facility as well, and therefore the production of these DEMs have similar problems to the HiRISE DTMs.

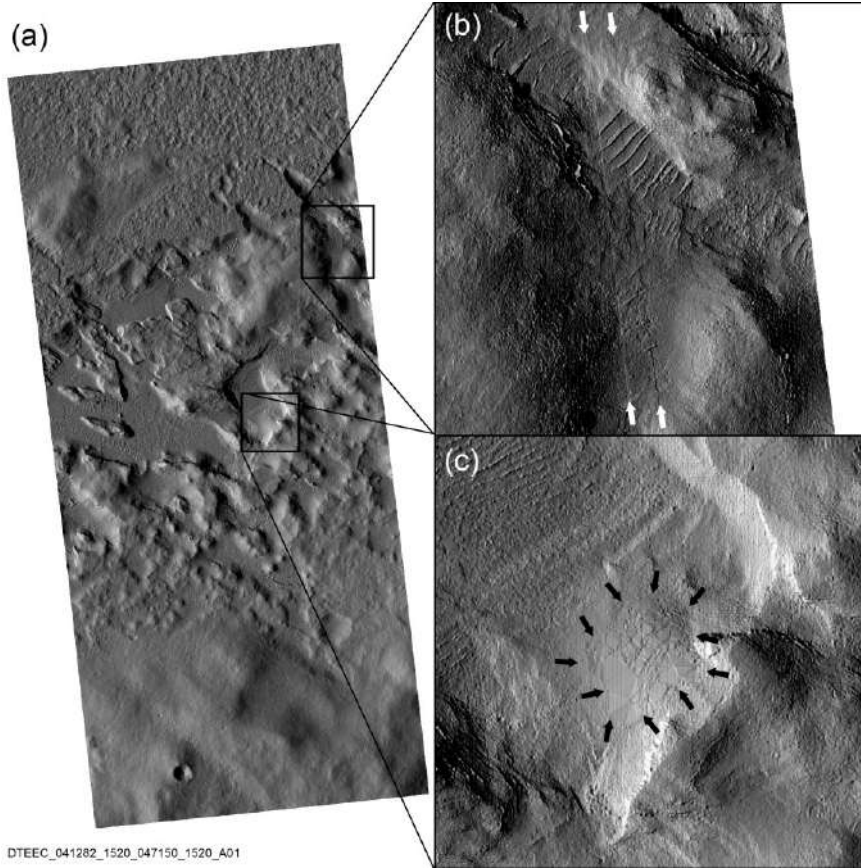


Figure 1.5 Artifacts occurred within the HiRISE DTM. (a) Shaded relief of a HiRISE DTM, (b) close-up of artifacts occurred along the image seams represented by white arrows, (c) close-up of the polygonal matching artifacts surrounded by black arrows (Kirk et al., 2008).

More recently, open-source software for the generic stereo processing of planetary images, the Ames Stereo Pipeline (ASP), has been developed independently by the Intelligent Robotics Group (IRG) at NASA Ames Research Center (Beyer et al., 2018; Broxton and Edwards, 2008; Moratto et al., 2010). The ASP provides a highly automated workflow (including feature extraction, triangulation) with manual processing, which can be run with the help of the ISIS3 and Geospatial Data Abstraction Library (GDAL). The ASP supports a variety of sensors, such as HiRISE, CTX, MOC, Lunar Reconnaissance Orbiter Camera, Apollo Metric, Cassini Imaging Science Subsystem, Galileo Solid-State Imaging experiment, New Horizons Long Range Reconnaissance Imager, DigitalGlobe WorldView-1/2, etc.

Since the first ASP release, many researchers have generated their private CTX/HiRISE stereo DEMs using the ASP applications (e.g., Baker and Head, 2015; Golombek et al., 2017; Harrison et al., 2013; Lefort et al., 2012; Levy et al., 2017; Schorghofer et al., 2019; Stucky de Quay et al., 2019; Öhman and McGovern, 2014). However, details in their data processing workflows are notably different (e.g., the presence or absence of bundle adjustment steps). Therefore their ASP-derived DEMs are likely to be a mixture of good and bad qualities. This issue arises from the scarcity of established methods for generating DEMs. While several researchers proposed the ASP-based procedure for the production of CTX and/or HiRISE DEMs (Hepburn et al., 2019; Kim and Muller, 2009; Mayer and Kite, 2016; Quantin-Nataf et al., 2018; Tao et al., 2018), these studies are intended to implement a fully automated DEM production. This does not allow the manual processing required for the theoretically best accuracies of the DEMs; for example, the

selection of source ground data, the generation of GCPs, the choices of the parameters used in individual ISIS3/ASP's applications.

Unlike previous methods, I propose that the extraction of DEMs with high(-est) absolute accuracy and reproducibility from HiRISE stereo pairs requires (1) the use of an adequate lateral reference that corresponds with the MOLA's vertical reference for bundle adjustment, (2) the use of intermediate products that bridge the resolution gap between MOLA and HiRISE, and (3) the alignment of a resulting point cloud to an intermediate-resolution DEM tied with MOLA footprints. Other issues involving the local vertical precision of DEMs (including artifacts) are not addressed here.

1.5 Topographic Mapping of Phobos

The numerical shape models and the DEMs of the Martian moon Phobos have been generated from images obtained by the spacecraft around Mars. Since the construction of low-resolution numerical shape models calculated from control points and limb/terminator measurements of Viking orbiter images (Thomas, 1993), stereo-photogrammetry, spherical harmonics, or SPC have been chiefly applied to Phobos-2, Viking Orbiter, and HRSC images to derive higher-resolution (down to ~ 100 m/pixel) shape models/DEMs of Phobos (Ernst et al., 2018; Ernst et al., 2015; Gaskell, 2011; Giese et al., 2005; Willner et al., 2010; Willner et al., 2014; Wählisch et al., 2010) (Figure 1.6).

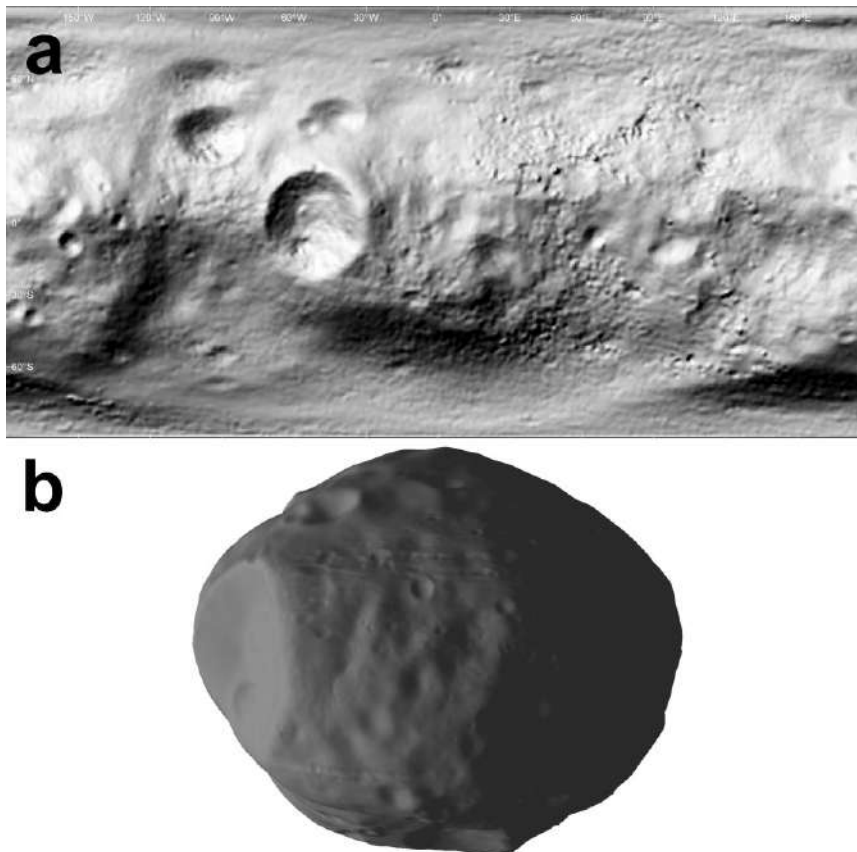


Figure 1.6 Available topographic data of Phobos. (a) Shaded relief of HRSC DTM (Willner et al., 2014), (b) SPC-derived shape model (Gaskell, 2011).

Although the HiRISE camera has already obtained high-resolution (~ 6 m/pixel) stereo-pair images of the nearside of Phobos (Figure 1.7), there is no available HiRISE DEM of Phobos

(Ivanov and Thomas, 2010; McEwen et al., 2010; Thomas et al., 2011). This is probably because of the technical issue inherent in data processing via the SOCET-SET toolchain, and no one has attempted to apply the ASP-based workflow to the HiRISE images of Phobos, except for our earlier work (Hemmi and Miyamoto, 2019).

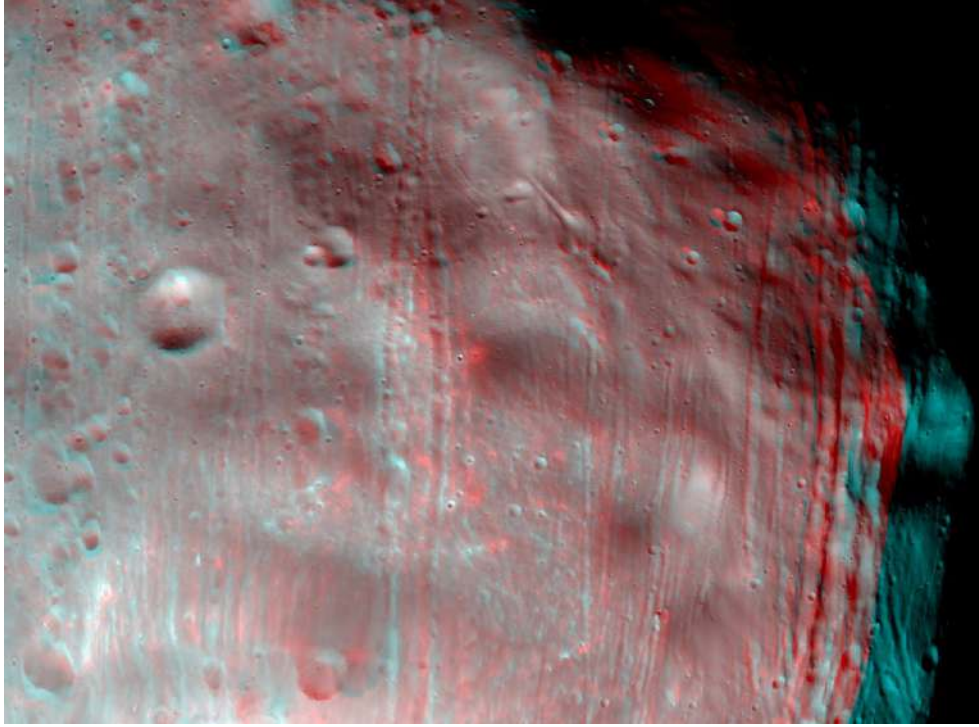


Figure 1.7 Anaglyph of Phobos to demonstrate the DEM extraction from its HiRISE stereo pair (Image credit: NASA/JPL/University of Arizona).

1.6 Objectives

Based on the above, this thesis aims to shed light on the existing issues in the following chapters:

- Establishment of the pipeline to derive high-accuracy DEMs, with horizontal and vertical accuracies comparable to those of the existing DEMs, from CTX/HiRISE stereo pairs of any target area where no high-resolution DEM products are publicly available (Chapter 2),
- Generation of high-resolution stereo-derived HiRISE DEMs of Mars (Chapter 3 and Chapter 4) and Phobos (Chapter 4),
- Demonstration of morphological analysis of small topographic features using the HiRISE DEMs; in particular, the 10s—100s-m-wide mounds in the northern lowlands (Chapter 3) and southern highlands (Chapter 4) on Mars for the assessment of mud eruption hypotheses,
- Characterization of the regolith of the Phobos' surface using the analyses on its sub-kilometer craters based on our HiRISE DEM (Chapter 5).

Chapter 2

Extraction of High-accuracy DEMs

2.1 Significance of Bundle Adjustment and Manual Refinement

The observation data of individual spacecraft missions are stored as “Spacecraft, Planet, Instrument, Camera-matrix, Events (SPICE) kernels” (Acton et al., 2018; Acton, 1996). The SPICE kernels include spacecraft/target body ephemerides (SPK), target body size/shape/orientation (PCK), instrument structure/orientation (IK), spacecraft/camera orientation (CK), spacecraft clock (SCLK), reference frame (FK), leap seconds table (LK), and target body’s shape model (DSK). In reality, they include serious uncertainties in observation geometry, such as spacecraft/camera pointing and position vectors, relative to the target body’s center and its geographic coordinate system. Without any improvement, these uncertainties would cause severe gross and random errors (Polidori and El Hage, 2020) in a resulting DEM (i.e., precision issues) and systematic errors between the DEM and reference data (i.e., accuracy issues).

To refine the spacecraft/target body’s position and pointing of each observation simultaneously, “bundle adjustment” (or “bundle block adjustment”) is commonly used (e.g., Triggs et al., 2000). At the very least, the bundle adjustment step requires image-to-image tie points with point coordinates in each two-dimensional image plane. As for the HiRISE camera, unlike frame cameras, the extraction and optimization of CCD-to-CCD tie points are required as well; that is, two HiRISE images are virtually regarded as twenty different HiRISE RED CCD images in the bundle adjustment step.

To scale, rotate, and translate the camera coordinate system to the so-called world coordinate system (i.e., the geographic coordinate system of Mars/Phobos), it is also necessary to obtain the control points that relate image pixels to known ground point coordinates (“ground control points”, or GCPs). Although most studies relied on the automatic image-to-image tie point extraction only, the extraction of GCPs for HiRISE is still challenging to automate. This is because the image-to-image registration algorithm fails to extract control points among the images observed with different imaging conditions (e.g., different wavelength, image quality, resolution) and/or surface conditions (e.g., temporal surface change). Thus, this thesis emphasizes that manual GCP acquisition/editing steps are indispensable for high-accuracy estimates of spacecraft/surface geometry.

2.2 Processing of HiRISE Stereo Imagery of Mars

This section focuses on the HiRISE data processing pipeline (Figure 2.1) used in Chapter 3 and Chapter 4, which are different from those performed by previous studies. First, high-accuracy GCPs were manually extracted from a pair of reference surface images (latitude and longitude source) and altitude data (radius source). This step is conducted through ISIS3’s *qnet* (Figure 2.1; Figure 2.2 depicts the graphical interface to create and edit GCPs).

In Chapter 3, the author performed two kinds of GCP acquisition steps for minimizing errors in ground coordinates: CTX-to-THEMIS/MOLA (CTX pipeline of Figure 2.1) and HiRISE-to-CTX controls (HiRISE pipeline of Figure 2.1). In the former step, the Mars THEMIS Controlled Mosaics (<https://astrogeology.usgs.gov/maps/mars-themis-controlled-mosaics-and-final-smithed-kernels>) (Ferguson et al., 2013; Ferguson and Weller, 2018) are used, which are so far the best ground-truth map to extract GCPs required for the bundle adjustment of CTX images.

These THEMIS mosaics are 100 m/pixel global maps that are derived from seamlessly co-registered THEMIS images tied to the gridded MOLA data (MEGDRs) within the $\pm 65^\circ$ latitude range. In the next step, GCPs are acquired to tie target HiRISE stereo pairs to the map-projected CTX DEM and its orthoimage which are controlled to the THEMIS/MOLA-based ground truth. The precisions of CTX-THEMIS/MOLA GCPs and HiRISE-CTX GCPs were assumed to be twice as large as the input image/DEM pixel scale, that is, 200/200/200 meters and 12/12/36 meters in longitude/latitude/radius directions, respectively.

In Chapter 4, due to the scarcity of CTX stereo pairs of target areas, instead of using the CTX DEMs/orthoimages tied to the MOLA/THEMIS ground data, GCPs were obtained by controlling HiRISE stereo pairs to the HRSC DTM and its orthoimage (at spatial resolutions of 12.5, 25.0, or 50.0 m/pixel) tied to MOLA.

Second, the bundle adjustment was performed based on GCPs (the ISIS3's *jigsaw* in Figure 2.1) (Edmundson et al., 2012), which supports exterior orientation only. Bundle adjustment generally represents the least-squares optimization of both exterior orientation parameters (i.e., camera pointing and position) and interior orientation parameters (i.e., camera distortions, focal lengths, and optical axis coordinates of frame cameras). However, the optimization of the interior orientation is skipped here. This is because the interior orientation is not applicable for the HiRISE camera due to its irregular optical structure and line-scan imaging system. Instead, the camera distortions and the HiRISE CCD-to-CCD offsets were corrected by post-processing (ISIS3's *noproj* and *hijitreg* internally executed by ASP's *hiedr2mosaic.py*) immediately after executing *jigsaw*.

Here, the *jigsaw*'s bundle adjustment was applied to a set of ten HiRISE RED images to refine camera angles (0.1-degree uncertainty), spacecraft positions (100-m uncertainty), spacecraft velocities (13-m/sec uncertainty), and the coordinate values of the GCPs (planetocentric latitude, longitude, and radius values) at once. The uncertainty values were set to be the corresponding accuracy values used by the USGS's SOCET SET workflow. At each iteration, the *jigsaw* outputs the image coordinate residuals of each GCP in pixels and their *a posteriori* standard deviation of unit weight value in pixels (generally called "*sigma0*"). If one or more incorrect tie points or GCPs are used, the *sigma0* value becomes larger than 1.0 pixels. Thus the tie points/GCPs were manually edited and *jigsaw* was performed for all the stereo pairs until it becomes well below 1.0 (mostly less than ~ 0.5) after manual correction of erroneous tie points (automatically collected by ISIS3's *pointreg*).

Third, DEM extraction (ASP's *stereo* and *point2dem*) was conducted after the bundle adjustment step and the general HiRISE image processing (i.e., correction of HiRISE camera distortions, alignment of HiRISE CCDs, mosaicking of HiRISE CCD images, the normalization between the stereo-pair images). The ASP's *stereo* is mainly constructed from disparity map initialization (its alignment method set to none because of the use of map-projected imagery; correlation kernel sizes respectively set to 25×25 and 21×21 pixels for CTX and HiRISE imagery), sub-pixel refinement (affine window (subpixel-mode 3) and the subpixel-kernel value of 25×25 pixels used for both CTX and HiRISE imagery), outlier rejection/hole filling, and triangulation steps. Unlike the USGS's SOCET SET-based pipeline, to improve stereo correlation and reduce the computation time of triangulation, both map projection (ASP's *cam2map4stereo.py*; in equirectangular projection above the MOLA reference sphere with a radius of 3,396,000 meters) and pyramid correlation (ASP's *sparse_disp* option with a corr-seed-mode value of 3 and a corr-max-levels value of 3) were applied to both CTX and HiRISE stereo pairs.

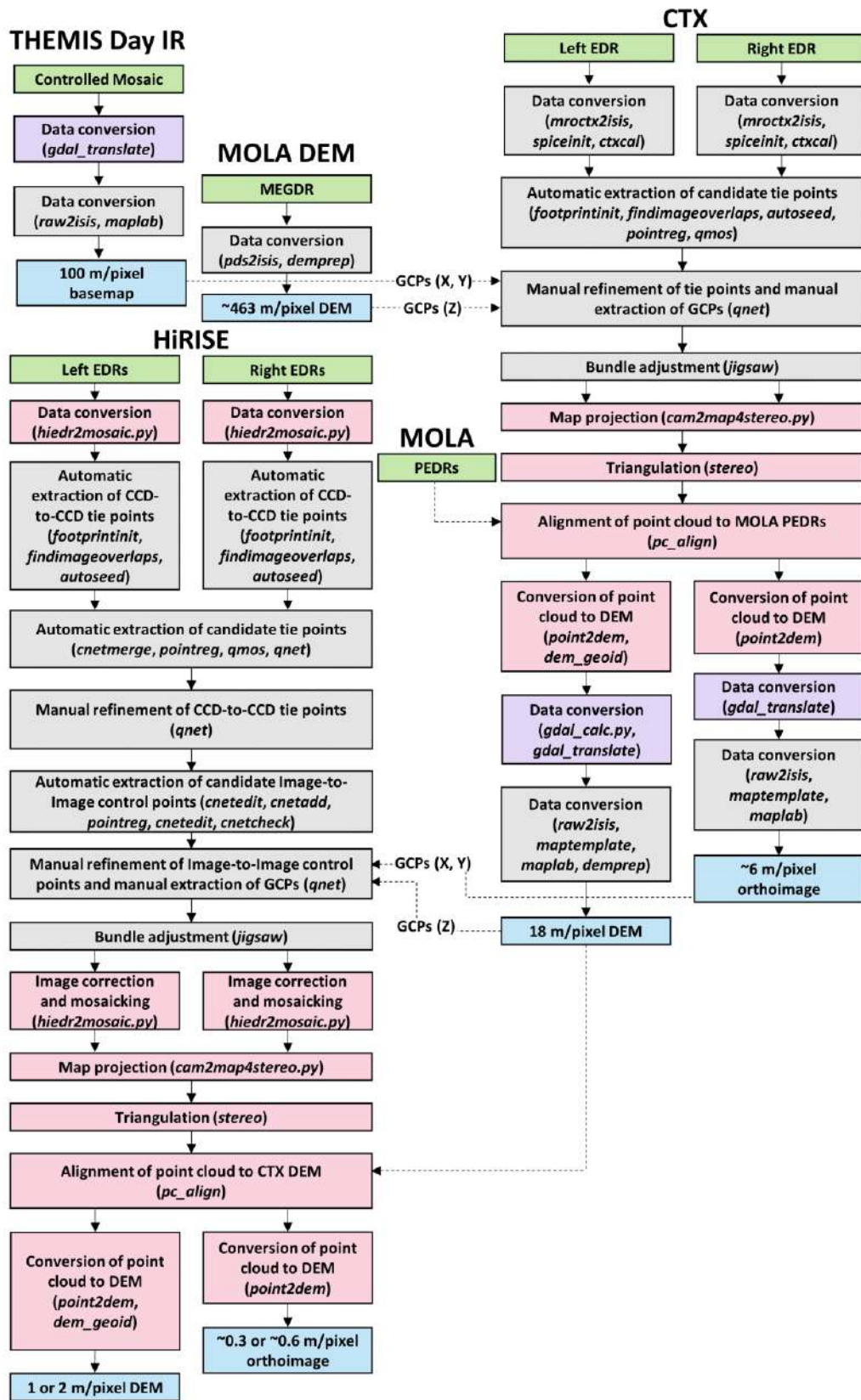


Figure 2.1 Flowchart for the generation of HiRISE and CTX DEMs from stereo pairs. Green and light-blue boxes show data inputs and outputs, respectively. Gray, pink, and purple colors represent the ISIS3, ASP, and GDAL application environments (*command*), respectively.

Table 2.1 Comparison of existing and proposed workflows for deriving HiRISE DEMs.

	Previous workflow for the existing HiRISE DTMs	Proposed workflow for the new HiRISE/CTX DEMs
Input data	MOLA PEDRs, HiRISE EDRs	THEMIS controlled mosaics, MOLA MEGDR and PEDRs, CTX and HiRISE EDRs
GCP acquisition	MOLA PEDRs nearest to HiRISE footprints used as GCPs for horizontal and vertical controls	Manual extraction of GCPs tying both CTX to THEMIS/MOLA DEM and HiRISE to CTX orthoimage/DEM
Sensor models, bundle adjustment, and triangulation	HiRISE raw data processed through both ISIS3 and a supporting script, and epipolar matching performed through SOCET SET's interface	ISIS3's HiRISE/CTX camera models and processing tools used, and template matching of map-projected stereo images performed through ASP's command-line processing
DEM accuracy control toward MOLA PEDRs	Not applicable	Alignments of CTX DEMs to MOLA PEDRs and HiRISE DEMs to CTX DEMs through the ICP method

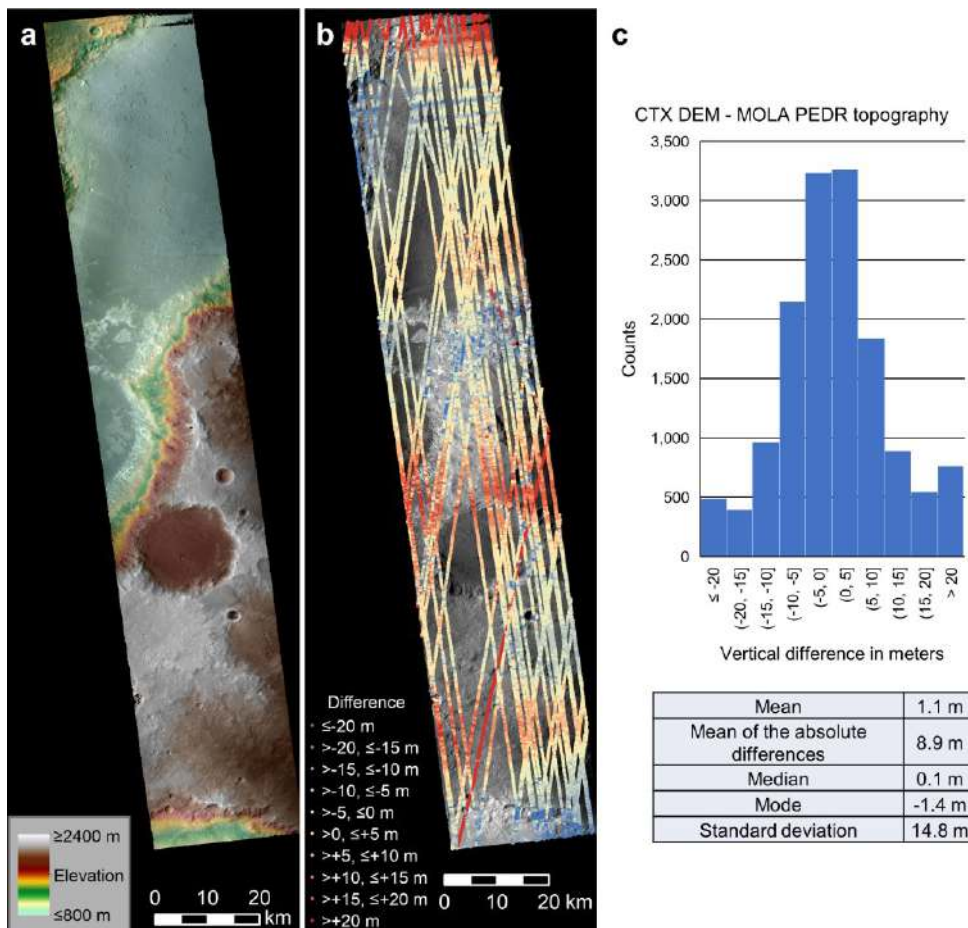


Figure 2.3 A produced CTX DEM (CTX_DEM1 described in Chapter 3) compared with MOLA PEDR footprints (a) A CTX orthoimage overlain with a colorized CTX DEM. (b) Vertical differences (CTX DEM minus MOLA PEDR topography) at individual PEDR points (n=14,520). (c) Frequency distribution of the difference values with statistics.

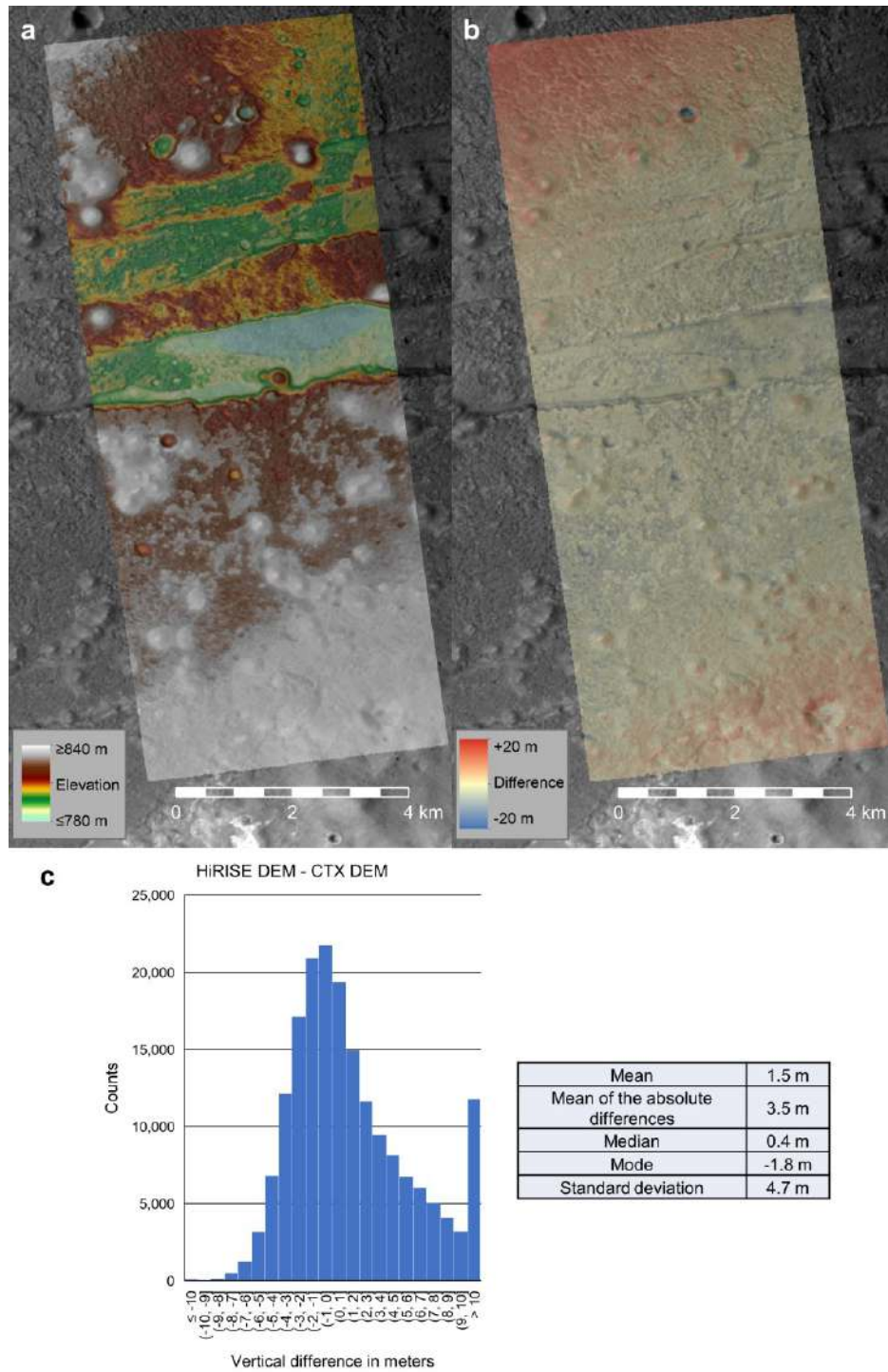


Figure 2.4 A produced HiRISE DEM (DEM1 described in Chapter 3) compared with a produced CTX DEM (Figure 2.3). (a) A CTX orthoimage overlain with a colorized HiRISE DEM. (b) Vertical differences (HiRISE DEM minus CTX DEM) at individual HiRISE DEM pixels ($n=184,508$). (c) Frequency distribution of the difference values with statistics.

2.3 Processing of HiRISE Stereo Imagery of Phobos

This section depicts the DEM generation procedure that is used in Chapter 5. This section mainly consists of the workflow described in the preceding section, except for the input images and reference data sets. Considering that the HiRISE RED channels have roughly a factor of two higher signal-to-noise ratios than those of the other two bands (McEwen et al., 2007), the only two RED band images (RED4 and RED5) are used for stereo-photogrammetry, rather than BG or NIR CCD images. One RED6 channel image, capturing the western rim of Stickney crater (i.e., left side of PSP_007769_9015, Figure 2.5), was not used due to limited area for obtaining control points and the need to mosaic HiRISE RED5 and RED6 images together. All image data sets used in this study are available in the PDS Geosciences Node (https://pds-geosciences.wustl.edu/mex/mex-msa-hrsc-5-refdr-phobos-maps-v1/mexhrs_5001/data/).

Following the aforementioned methods for producing HiRISE DEM of Mars surface, the ISIS3 was used to perform the HiRISE image processing: converting the raw image data (HiRISE Experimental Data Record products) in PDS format to ISIS cube format; radiometric calibration of the image data; normalization of columns in each cube (subtracting the median value from each column); merging a HiRISE channel image pair (channels 0 and 1) of each RED channel to a single RED image (line-by-line equalization and additive component were also applied to correct down-track differences in the channels); importing SPICE kernels (e.g., ephemeris, original spacecraft position, and instrument pointing data recorded during each CCD image acquisition and the user-defined Phobos shape model (Willner et al., 2014)) to each camera cube; and removing noise in the camera pointing.

For bundle adjustment, a total of 23 tie points were manually picked from four HiRISE RED images (Figure 2.5), then obtained ground coordinates of all the points from the global HRSC orthoimage mosaic (Wählisch et al., 2014) (~12.1 m/pixel) and the global radius map (100 m/pixel) derived from HRSC DTM (Willner et al., 2014). A priori sigma values for northing, easting, and radius were taken to be 25 m, 25 m, 100 m, respectively. Using these ground control points, this study performed a bundle adjustment to solve camera angles (0.1-degrees uncertainty), spacecraft positions (100-m uncertainty) and velocities (13-m/sec uncertainty) of the 4 HiRISE RED images and the local radius of each control point.

Following the bundle adjustment and the removal of camera distortion and jitter of each HiRISE RED image, I created a mosaic of HiRISE RED4 and RED5 images for both left and right images of the stereo pair, and applied map projection (equirectangular projection, 11.1 km-radius reference sphere) to them using the ASP version 2.5.1 (Figure 2.6). This process improves image alignment for the following stereo correlation.

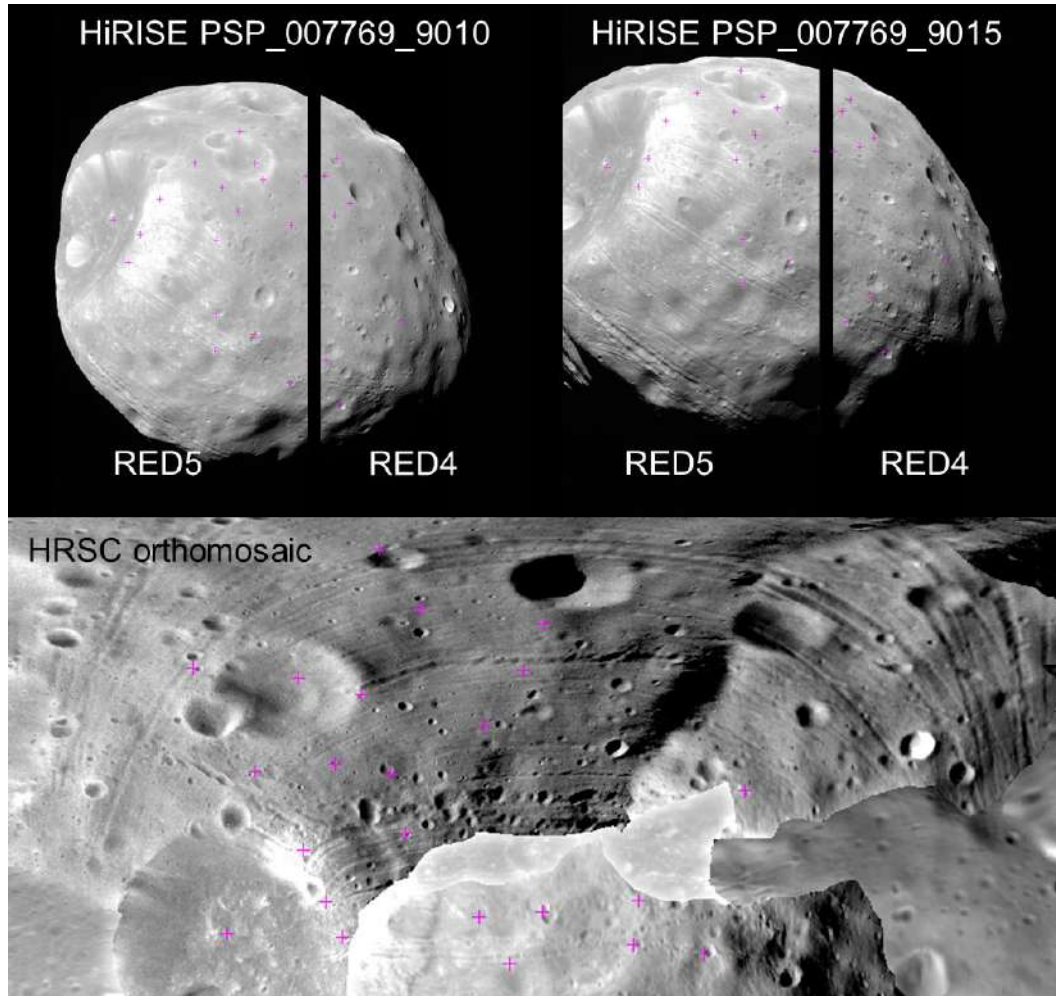


Figure 2.5 A stereo pair of HiRISE images of Phobos (upper left and right images) and a part of HRSC global orthomosaic (lower image). Ground control points are denoted by magenta crosses.

After initializing correlation with "seed-mode 3" (the ASP's `sparse_disp` utility), ASP's two-step pyramid correlation was conducted: a disparity map initialization with $31 \text{ pixels} \times 31 \text{ pixels}$ correlation kernel size and a subpixel refinement with $25 \text{ pixels} \times 25 \text{ pixels}$ correlation kernel size. Finally, the ASP triangulation routine was used to derive a 3D-coordinate at each of the matched pixels from the closest distance between two intersecting rays from sensor orbital positions. A high-resolution ($\sim 6.56 \text{ m/pixel}$) 3D-point cloud generated from the ASP triangulation was converted to the DEM (elevation values relative to an 11.1-km-radius sphere) at a spatial pixel scale of 20 m in equidistant cylindrical (or plate carrée) projection (standard parallel = $\sim 1.720^\circ\text{S}$). Points with triangulation error (i.e., the closest distance of the two rays) larger than 9.0531 m were removed from the point cloud. The corresponding orthoimage with a resolution of $\sim 6.56 \text{ m/pixel}$ was also constructed using the DEM and left image (Figure 2.7). From the three-dimensional observation geometry of emission angles and spacecraft ground azimuths, the parallax-height ratio (dp) was calculated to be ~ 0.343 (Becker et al., 2015). Assuming a 0.2-pixel matching error (Kirk et al., 2008), the vertical accuracy can be estimated at $\sim 4.17 \text{ m}$ from the dp value and a pixel scale of an oblique (lower-resolution) image of the stereo pair ($\sim 7.17 \text{ m}$).

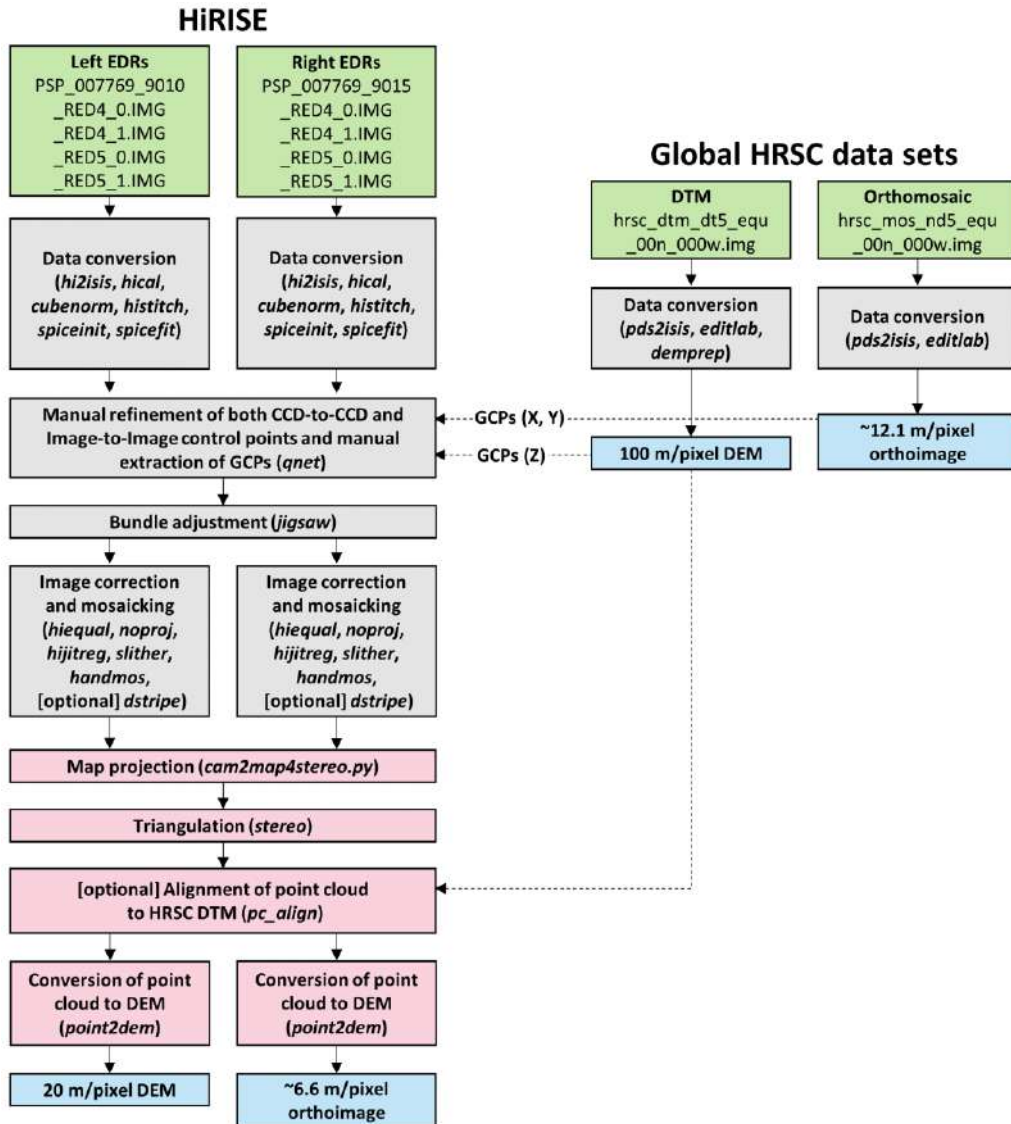


Figure 2.6 Workflow showing image processing and DEM extraction from HiRISE stereo images of Phobos. Green and light-blue boxes show data inputs and outputs, respectively. Gray and pink colors represent the ISIS3 and ASP application environments (*command*), respectively.

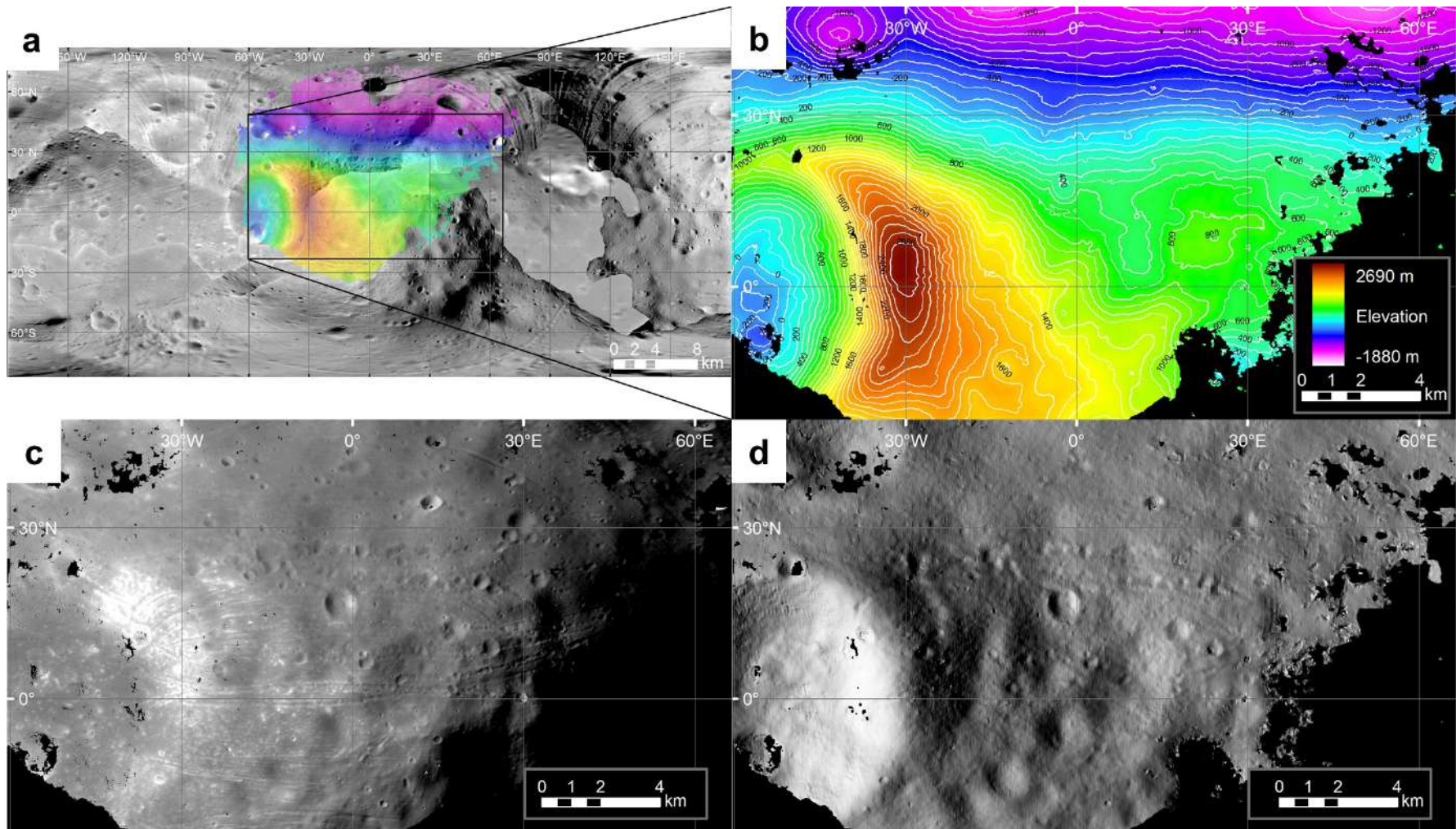


Figure 2.7 The resulting HiRISE stereo-derived DEM of Phobos. (a) Colorized DEM over on a global mosaic of HRSC orthoimages (Wählisch et al., 2014), (b) DEM with 100-m contour intervals, (c) contrast-enhanced orthoimage, (d) shaded relief map derived from the DEM.

Chapter 3

Distribution, Morphology, and Morphometry of Circular Mounds in the Elongated Basin of Northern Terra Sirenum, Mars

The content of this chapter was peer-reviewed and published as a research article in *Progress in Earth and Planetary Science* by SpringerOpen in 2017. The SpringerOpen allows the use of the paper in the author's dissertation, and its published version can be deposited in the author's institutional repository.

Article information:

Hemmi, R., Miyamoto, H., 2017. Distribution, morphology, and morphometry of circular mounds in the elongated basin of northern Terra Sirenum, Mars. *Progress in Earth and Planetary Science*. 4, 26, DOI: 10.1186/s40645-017-0141-x.

RESEARCH ARTICLE

Open Access



Distribution, morphology, and morphometry of circular mounds in the elongated basin of northern Terra Sirenum, Mars

Ryodo Hemmi and Hideaki Miyamoto*

Abstract

An elongated, flat-floored basin, located in the northern part of Terra Sirenum on Mars, holds numerous enigmatic mounds (100 m wide) on the surface of its floor. We investigated their geological context, spatial distribution, morphological characteristics, and morphometric parameters by analyzing a variety of current remote sensing data sets of Mars. Over 700 mounds are identified; mapping of the mounds shows the spatial density of about 21 per 100 km² and appearances of several clusters, coalescence, and/or alignment. Most of the mounds have smoother surface textures in contrast to the rugged surrounding terrain. Some of the mounds display depressions on their summits, meter-sized boulders on their flanks, and distinct lobate features. We also perform high-resolution topographic analysis on 50 isolated mounds, which reveals that their heights range from 6 to 43 m with a mean of 18 m and average flank slopes of most mounds are below 10°. These characteristics are consistent with the deposition and extension of mud slurries with mud breccia and gases extruded from subsurface, almost equivalent to terrestrial mud volcanism. If so, both abundance of groundwater and abrupt increase in pore fluid pressure are necessary for triggering mud eruption. Absolute crater retention ages suggest that the floor of the basin located among middle Noachian-aged highland terrains has been resurfaced during the Late Hesperian Epoch. Because of cross-cutting relationships with the basin and the mounds superposed on the basin floor, the faults and fissures (part of Memnonia Fossae) are thought to have formed during and/or after the period of mound formation. Compressional stress fields which likely formed Memnonia Fossae and Mangala Valles, expected from the dike emplacement model of Wilson and Head (JGR 107:1-1-24, 2002), may have facilitated undercompaction or overpressurization of subsurface fluids, focused pore fluids beneath the basin, and opened conduits along faults for upwelling voluminous sediments and fluids.

Keywords: Mars, Terra Sirenum, Remote sensing, Mud volcanism

Introduction

Across the southern highlands of Mars, potential groundwater and/or hydrothermal circulation during the Noachian to Hesperian or possibly Amazonian ages has been repeatedly suggested, as evidenced by the morphology of valley networks, regional fissures and associated fluvial channels (e.g., Tanaka and Chapman 1990; Wilson and Head 2002), and distinct spectral signatures of phyllosilicates, chlorides, and sulfates (e.g., Glotch et al. 2010; Wray et al. 2011; Michalski et al. 2017). However,

fluxes of groundwater and surface water, the interaction between groundwater activity and heat flux, the presence of a purported cryosphere (Clifford and Parker 2001) or subsurface clathrate of carbon dioxide and methane, and the timing of a halt of possible groundwater activity or whether liquid water is still extant, remain uncertain.

On early Mars (Noachian to Hesperian Periods with approximate absolute age ranging from 4.1 to 3.1 Gyr (Tanaka et al. 2014)), groundwater/hydrothermal systems, estimated from the presence of clay minerals on a global scale (Ehlmann et al. 2013), may have occurred, with diverse evidence including a number of putative mud volcanoes being reported in both the northern

* Correspondence: hm@sys.t.u-tokyo.ac.jp
Department of Systems Innovation, School of Engineering, The University of Tokyo, 7-3-1 Hongo, Bunkyo-ku, Tokyo 113-8656, Japan

lowlands (e.g., Tanaka et al. 2005) and relatively old, southern highlands (e.g., Pondrelli et al. 2011; Okubo 2016). However, the spatial extent of potential mud volcanism on Mars has yet to be fully understood. Moreover, criteria for distinguishing between mud volcanoes and other morphologically similar landforms (e.g., cinder cones, tuff cones, rootless cones, pingos) have yet to be established.

Our study area, an unnamed NNE-SSW elongated depression (25–28°S, 203–205°W; ~150 km long, <~50 km wide), is located on the northern part of Terra Sirenum in the southern highlands of Mars (Fig. 1). This basin was previously mapped as the middle or early Noachian-aged highland units (mNh and eNh units; Tanaka et al. (2014))

which are the same geological units as the surrounding cratered terrain. Based on the analysis of high-resolution hyperspectral data, Wray et al. (2011) suggested that these surrounding impact basins, especially Columbus and Cross craters, contain light-toned layered deposits including sulfates and phyllosilicate minerals, which imply the deep paleolakes, fed by upwelling groundwater, may have existed and formed these deposits during the late Noachian period.

The southern part of Memnonia Fossae, one of the largest graben systems that radially extended from the Tharsis rise, traverses the basin from east to west, where dike intrusions and associated melting of cryosphere may have occurred along these faults (Wilson and Head 2002),

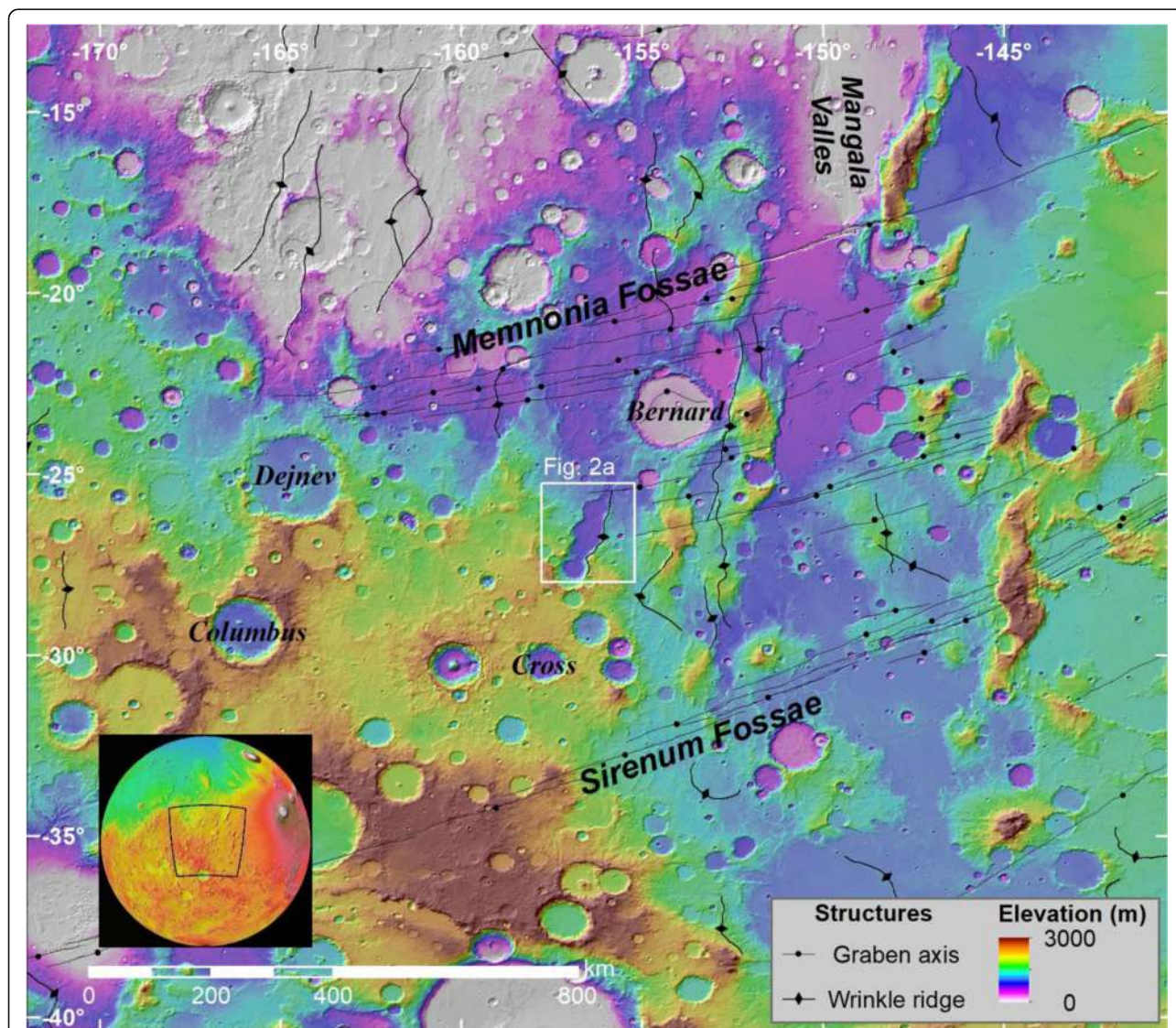
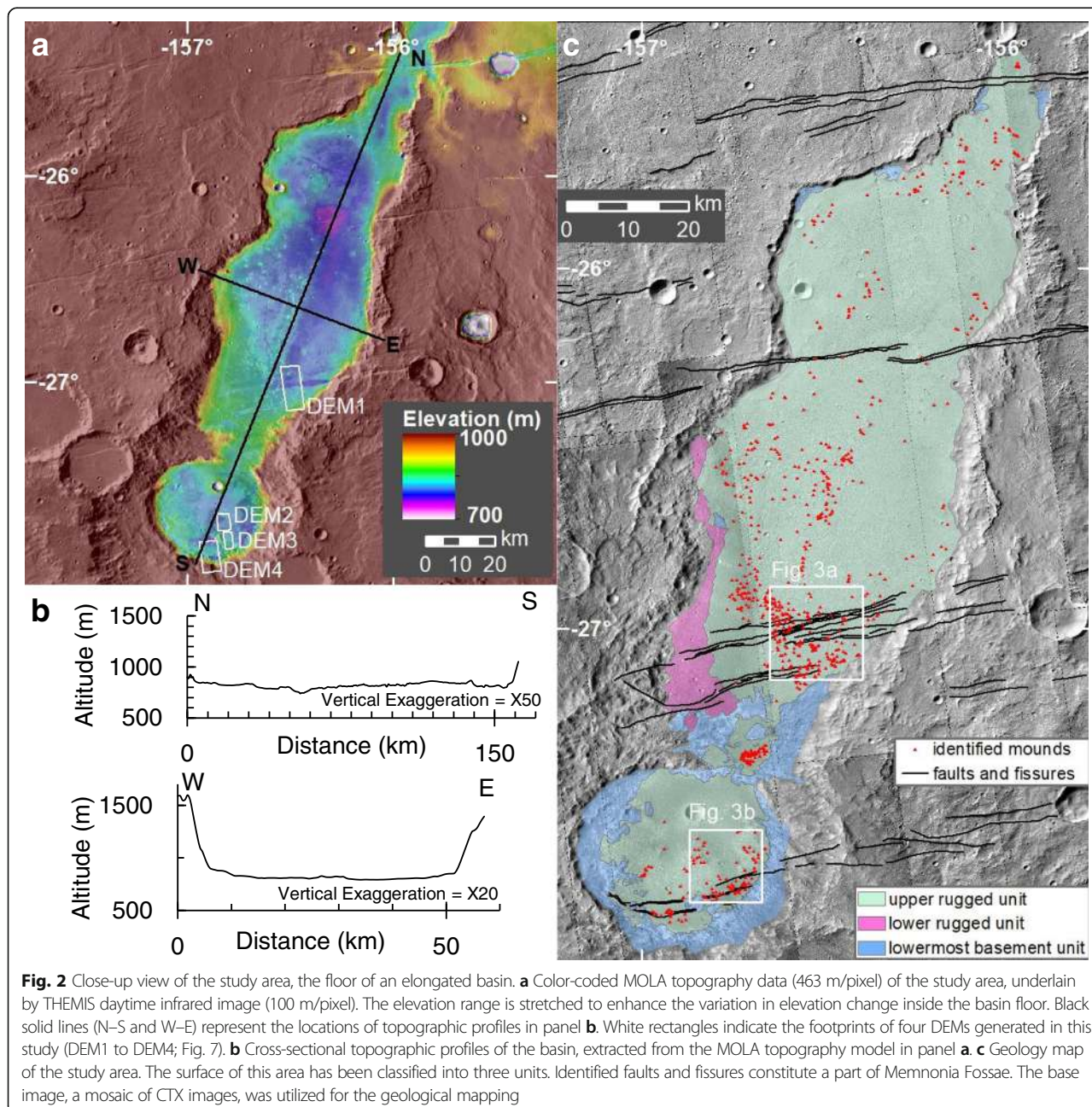


Fig. 1 Color-coded topographic map of the northern part of Terra Sirenum. Base map is the gridded MOLA topography data (512 pixels/degree) overlaying the corresponding MOLA-shaded relief map (Smith et al. 2001) in simple cylindrical projection. Regional structures, interpreted by Tanaka et al. (2014), are drawn as solid black lines with symbols. A white rectangle indicates the location of Fig. 2. The inset shows the location of the study area on MOLA global topography map rendered with the Google Earth

which is supported by the presence of Mangala Valles, the major outflow channel sourced from the northern Memnonia Fossae. Cross-cutting relationship between Memnonia Fossae and the basin shows the activity of Memnonia Fossae followed the basin formation. Wrinkle ridges, with N-S trending axis observed around this region, indicate the circum-Tharsis W-E compressional fields (Head et al. 2002), possibly associated with the Tharsis rise formation on global scale.

The shape of the elongated basin appears to be a chain of several circular sub-basins with flat floors (Fig. 2). This may indicate the integration of multiple impact

craters caused by erosional processes with subsequent crater-filling depositions. Profiles of global topography model (Fig. 2c) show that inside of the basin has a mostly flat-floored surface with a slight variation in elevation (between 800 and 900 m in altitude) surrounded by the mountain ranges with altitudes of more than 1200 m (except the northern part of the basin), while the terrain outside of the basin has an inclined topography on a regional scale: the south of the basin has relatively high altitudes (~ 2000 m) than the north (~ 1000 m). No obvious fluvial channel into this basin exists.



Numerous well-preserved circular mounds are distributed inside this basin floor (Fig. 3), which contrasts to other neighboring regions on Terra Sirenum. Recently acquired high-resolution images enable us to characterize their stratigraphy, morphology, and morphometry. Thus, this study focuses on the characterization of the circular mounds on the elongated basin to reveal their formational mechanisms and their relation to the occurrence of the basin and regional geological structures. We propose that development of faults facilitated the migration and overpressurization of subsurface fluids and triggered mud extrusions. This would lead to better understanding of the evolution of hydrology and structural geology across Terra Sirenum and the assessment of its astrobiological potential.

Methods/Experimental

Data sets and processing tools

The following data products are used in this study (mostly as Geographic Information System (GIS) data

sets provided by the NASA Planetary Data System, Arizona State University, University of Arizona and the United States Geological Survey (USGS) database): the Mars Odyssey's Thermal Emission Imaging System (THEMIS; Christensen et al. 2004) daytime infrared image mosaic for geological mapping and crater counting at 100 m/pixel, the Mars Global Surveyor (MGS) Mars Orbiter Laser Altimeter (MOLA; Smith et al. 2001) high-accuracy altimetry profile data (or Precision Experiment Data Records (PEDRs)) for the alignment of digital elevation models (DEMs) to Mars global topography, MOLA global topography models at 128 pixels per degree (also known as Mission Experiment Gridded Data Records, or MEGDRs) for examining the regional topography (Fig. 1), and the Mars Reconnaissance Orbiter's (MRO) Context Camera (CTX; Malin et al. (2007)) images at ~5–6 m/pixel for geological mapping and the generation of DEMs, and MRO High Resolution Imaging Science Experiment (HiRISE; McEwen et al. (2007)) images at up to ~25 cm/pixel

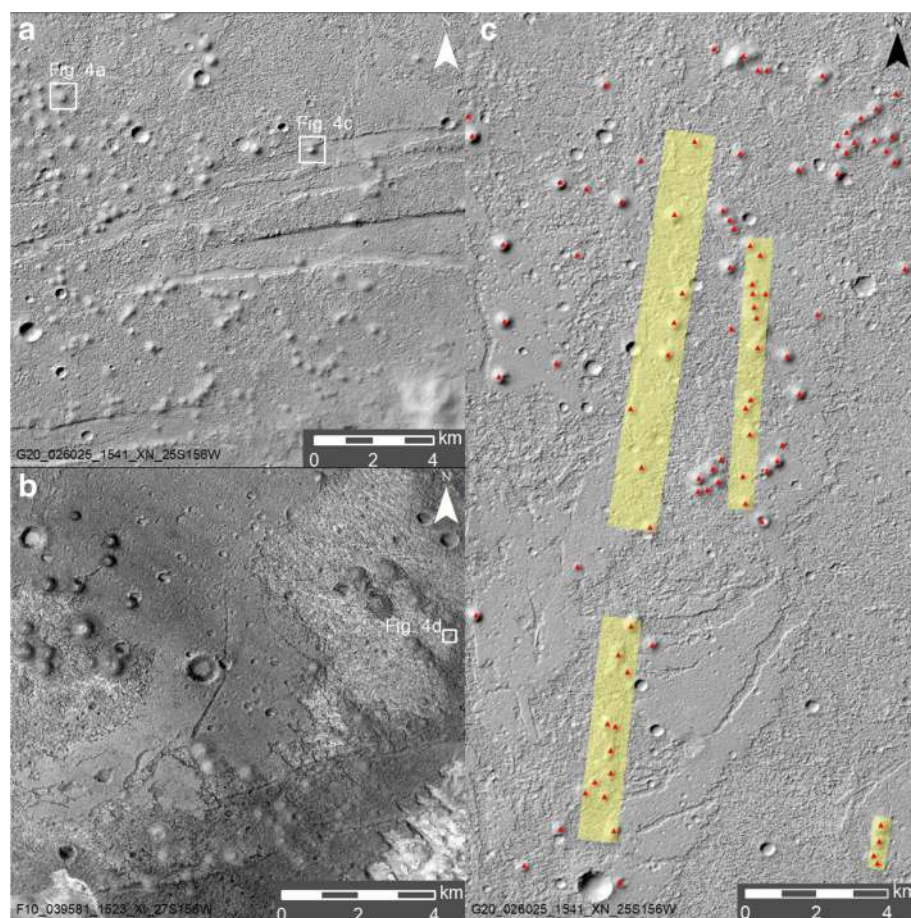


Fig. 3 Example of the mound fields. **a** Mounds located in the middle part of the upper rugged unit. Illumination from the upper left. Part of CTX image. **b** Mounds located in the southern part of the upper rugged unit. Illumination from the upper left. Part of CTX image. **c** Interpreted areas of the alignments (yellow rectangles) of the mounds (red triangles)

for the identification of small-scale morphologies and the generation of DEMs. The Java Mission-planning and Analysis for Remote Sensing (JMARS; <https://jmars.asu.edu/>) software developed by Arizona State University, the USGS Integrated Software for Imagers and Spectrometers (ISIS; <https://isis.astrogeology.usgs.gov/>) and the ESRI ArcGIS 10.2, and the Geospatial Data Abstraction Library (GDAL) were mainly utilized for browsing the datasets, processing raw data products, and analyzing the image data on the GIS platform.

Generation of Digital Elevation Models

The workflow of creating high-resolution DEMs and orthoimages is twofold: (1) generating CTX-derived DEMs (18 m post-spacing) tied to MOLA PEDRs and a cartographically controlled mosaic of THEMIS daytime infrared images (Ferguson et al. 2013) and (2) making HiRISE-derived DEMs (1 or 2 m post-spacing) tied to the CTX-derived DEMs. In either step, photometric calibration, bundle adjustment based on the ground control points collected from the THEMIS mosaic or CTX-derived DEMs with orthoimages, and map projection of stereo images were performed using ISIS's applications, and then, stereophotogrammetric triangulation, orthorectification, and the alignment of the CTX-derived DEMs to MOLA PEDR were performed with the NASA Ames Stereo Pipeline (ASP) (Broxton and Edwards 2008; Moratto et al. 2010; Beyer et al. 2014; Shean et al. 2016). In this study, a total of two CTX-derived DEMs (used only for co-registration of HiRISE-derived DEMs) and four HiRISE-derived DEMs were extracted (Table 1). Vertical accuracy (or expected precision) of each DEM is in the range of 0.19 to 0.90 m, which has been calculated from the product of 0.2 pixel (stereo matching error) and maximum image resolution between the two images, divided by the parallax-height ratio (e.g., Kirk et al. 2008; Becker et al., 2015; Beddingfield et al. 2015).

Measurements of geometric parameters of mounds

Morphometric parameters (basal diameters and maximum mound heights) of the 50 (sub-)circular

mounds were measured using four HiRISE-derived DEMs. Each of the mounds, confirmed in the orthoimages overlaid with the DEMs, was manually delineated using ArcGIS, and then, the mean elevation values along the outlines and the areas and the maximum elevation values inside each outline were measured. Basal diameter and maximum mound height were defined as the diameter of the circle area equivalent to the measured area and the difference between the maximum and mean elevation values, respectively. Highly degraded mounds, irregularly shaped mounds, coalesced mounds, mounds superposed on highly inclined substrata, mounds less than a hundred meters diameter (equivalent to only 5 or 10 DEM pixels), and mounds outside of the valid DEMs were excluded for the measurements due to the difficulty of identifying their outlines and increasing the uncertainty in morphometric parameters. Considering the horizontal resolution and vertical accuracy of each DEM and the variability of manual outlining, errors in basal diameters and maximum mound heights are estimated to be at most ± 8 m and ± 2.0 m, respectively.

Moreover, statistics of slope angles of each mound (mean, minimum, maximum, standard deviation) were also examined using the slope maps (maximum gradient values per pixel scale, in degrees) directly converted from HiRISE-derived DEMs (Table 2). For some mounds, we also extracted the topographic profiles of some mounds in cross-sections as well using the ArcGIS 3D analyst tool.

Estimates of surface formation ages

We followed the commonly accepted techniques of statistical analysis of impact craters on planetary bodies, crater size-frequency distribution (CSFD) (Crater Analysis Techniques Working Group 1979), to estimate the absolute model ages of the formation of the target areas. For mapping and measuring the impact craters on the targeted areas in THEMIS and CTX images, we used the CraterTools software (Kneissl et al. 2011) on the

Table 1 List of the details of four HiRISE-derived DEMs and two CTX-derived DEMs generated in this study

DEM ID	Spatial resolution (m/post)	Vertical accuracy (m)	Stereo pairs used for the generation of DEMs				
			Image 1		Image 2		Parallax-height ratio
			Image ID	Resolution (m/pixel)	Image ID	Resolution (m/pixel)	
DEM1	2.0	0.24	ESP_047862_1525	0.53	ESP_048152_1525	0.52	0.435
DEM2	2.0	0.90	ESP_039370_1520	0.51	ESP_039581_1520	0.25	0.085
DEM3	1.0	0.55	ESP_039581_1520	0.25	ESP_047150_1520	0.26	0.093
DEM4	2.0	0.19	ESP_040293_1520	0.55	ESP_047506_1520	0.26	0.416
CTX_DEM1	18	2.17	F10_039726_1522_XI_27S156W	5.56	F11_040003_1522_XI_27S156W	5.31	0.485
CTX_DEM2	18	12.02	F09_039370_1524_XI_27S156W	5.13	F10_039581_1523_XI_27S156W	5.09	0.084

Table 2 Geometric parameters of 50 mounds measured in this study

DEM used for measurement	Mound ID	Center latitude (°N)	Center longitude (°E)	Basal diameter (m)	Maximum height (m)	Height-width ratio	Slope angles (°)			
							Maximum	Minimum	Median	SD
DEM1	Mound1_1	−26.9533	−156.5379	284	21.5	0.076	35.8	0.2	9.8	3.3
DEM1	Mound1_2	−26.9606	−156.5390	165	8.6	0.052	35.0	0.3	6.6	2.3
DEM1	Mound1_3	−26.9645	−156.5376	234	13.4	0.057	58.2	0.3	8.2	3.7
DEM1	Mound1_4	−26.9673	−156.5329	395	22.2	0.056	51.8	0.1	9.9	4.7
DEM1	Mound1_5	−26.9768	−156.5351	420	35.5	0.084	58.1	0.1	11.6	4.5
DEM1	Mound1_6	−26.9508	−156.5083	160	7.3	0.046	14.5	0.1	5.7	2.4
DEM1	Mound1_7	−26.9594	−156.5057	442	42.9	0.097	48.6	0.1	13.0	5.0
DEM1	Mound1_8	−27.0061	−156.5324	324	26.5	0.082	47.9	0.1	11.2	4.0
DEM1	Mound1_9	−27.0232	−156.4857	205	12.7	0.062	33.9	0.1	7.9	3.1
DEM1	Mound1_10	−27.0236	−156.4804	367	26.6	0.072	66.0	0.1	10.0	4.5
DEM1	Mound1_11	−27.0424	−156.5225	260	17.5	0.067	17.9	0.1	8.9	3.0
DEM1	Mound1_12	−27.0478	−156.5259	205	10.6	0.052	18.2	0.2	6.9	2.8
DEM1	Mound1_13	−27.0521	−156.5224	200	11.6	0.058	35.8	0.1	6.9	3.3
DEM1	Mound1_14	−27.0504	−156.5158	217	11.1	0.051	17.2	0.0	7.8	3.7
DEM1	Mound1_15	−27.0428	−156.5069	203	12.6	0.062	67.0	0.2	8.1	2.9
DEM1	Mound1_16	−27.0316	−156.4589	404	28.6	0.071	49.4	0.0	10.0	4.2
DEM1	Mound1_17	−27.0554	−156.4517	271	18.8	0.070	22.9	0.0	8.8	3.2
DEM1	Mound1_18	−27.0659	−156.4866	367	31.6	0.086	54.4	0.0	10.6	4.0
DEM1	Mound1_19	−27.0683	−156.4712	343	21.1	0.062	34.0	0.0	7.3	3.4
DEM1	Mound1_20	−27.0747	−156.4829	238	17.0	0.071	18.7	0.3	9.1	2.5
DEM1	Mound1_21	−27.0810	−156.4814	331	28.7	0.087	41.8	0.2	10.8	3.6
DEM1	Mound1_22	−27.0836	−156.4749	345	25.2	0.073	33.6	0.1	9.4	3.5
DEM1	Mound1_23	−27.0843	−156.4679	249	15.3	0.062	24.4	0.0	8.3	3.1
DEM1	Mound1_24	−27.0878	−156.4687	184	11.7	0.063	27.8	0.2	7.5	3.0
DEM1	Mound1_25	−27.0851	−156.4642	184	11.9	0.064	24.7	0.1	8.5	3.3
DEM1	Mound1_26	−27.0812	−156.4620	328	24.5	0.075	35.3	0.0	9.3	3.0
DEM1	Mound1_27	−27.0741	−156.4570	212	15.3	0.072	20.2	0.1	8.3	3.1
DEM1	Mound1_28	−27.0893	−156.4569	391	30.1	0.077	36.2	0.2	9.4	3.4
DEM1	Mound1_29	−27.0903	−156.4467	237	13.1	0.055	68.0	0.0	8.2	4.3
DEM1	Mound1_30	−27.0867	−156.5048	230	7.8	0.034	43.2	0.1	5.5	3.1
DEM1	Mound1_31	−27.0994	−156.5155	336	23.6	0.070	58.2	0.1	9.2	3.2
DEM1	Mound1_32	−27.0982	−156.5081	214	9.1	0.043	23.9	0.1	5.9	2.5
DEM1	Mound1_33	−27.1091	−156.5083	209	12.6	0.060	17.3	0.3	7.9	2.5
DEM1	Mound1_34	−27.1069	−156.4880	270	17.4	0.065	18.7	0.1	8.6	2.7
DEM1	Mound1_35	−27.0951	−156.4716	286	17.6	0.062	26.6	0.2	7.9	2.7
DEM1	Mound1_36	−27.0999	−156.4687	276	16.2	0.059	31.2	0.1	7.9	3.4
DEM1	Mound1_37	−27.1021	−156.4605	190	8.5	0.045	17.3	0.1	5.7	2.3
DEM2	Mound2_1	−27.6464	−156.8530	392	28.8	0.073	66.0	0.1	12.6	6.4
DEM2	Mound2_2	−27.6443	−156.8323	301	20.3	0.067	51.1	0.0	10.0	4.9
DEM2	Mound2_3	−27.7031	−156.8175	253	19.0	0.075	59.0	0.1	11.1	6.4
DEM3	Mound3_1	−27.7394	−156.8234	171	8.6	0.050	67.3	0.2	17.4	10.3
DEM3	Mound3_2	−27.7409	−156.8065	276	27.6	0.100	75.7	0.0	19.1	10.7
DEM3	Mound3_3	−27.7376	−156.7896	205	16.6	0.081	75.0	0.1	19.8	11.0

Table 2 Geometric parameters of 50 mounds measured in this study (*Continued*)

DEM3	Mound3_4	− 27.7535	− 156.7985	186	10.6	0.057	76.6	0.1	19.4	11.3
DEM4	Mound4_1	− 27.7796	− 156.9253	265	16.6	0.062	23.1	0.0	8.0	3.0
DEM4	Mound4_2	− 27.7784	− 156.9155	242	17.0	0.070	31.8	0.1	8.2	3.2
DEM4	Mound4_3	− 27.7954	− 156.9167	203	11.5	0.057	17.6	0.1	7.0	2.5
DEM4	Mound4_4	− 27.8110	− 156.9188	207	9.5	0.046	16.8	0.2	6.2	2.3
DEM4	Mound4_5	− 27.8032	− 156.8946	206	13.5	0.065	20.2	0.3	8.0	2.5
DEM4	Mound4_6	− 27.8081	− 156.8855	147	6.0	0.041	13.8	0.1	5.4	2.0

ArcGIS ArcMap platform, due to its advantage of reducing the measurement errors dependent on different map projections. We then utilized the CraterStats II software (Michael and Neukum 2010) to plot the cumulative form of the CSFD. Absolute model ages are based on the crater production function of (Hartmann and Neukum 2001) with the crater chronology function from (Ivanov 2001). Note that we excluded the craters less than 100 m in diameter for these plots to decrease the biases influenced by possible overlooking of numerous smaller craters. In the event that small-diameter craters appeared overprinted by resurfacing events (e.g., erosion, mantling), suggested by a distinct “kink” in the CSFD, the resurfacing correction (Michael and Neukum 2010) was also applied to reconstruct the slopes of the CSFD consistent with the isochrons.

Results and discussion

Geologic classification of the basin floor

Based on the surface textures and stratigraphic relationships identifiable in HiRISE and CTX images, we classified the basin floor into three geological units (Fig. 2c): (1) upper rugged unit (surface area = $\sim 3500 \text{ km}^2$) which has a rugged surface with superposed impact craters and the target mounds, (2) lower rugged unit which has a rugged surface with impact craters much more abundant than the overlying upper rugged unit (surface area = $\sim 180 \text{ km}^2$), (3) lowermost basement unit (surface area = $\sim 530 \text{ km}^2$) which has rocky hillocks or degraded bedrock interbedded with strata of light-toned layered rocks (Wray et al. 2011) in places. This study focuses on the upper rugged unit which includes all of the targeted mounds.

Distribution of the mounds

Using the CTX and HiRISE images, we identified a total of 744 mounds from the upper rugged unit (Fig. 2c), giving the mean of their areal density of ~ 21 per 100 km^2 . The resultant map of the identified mound fields shows the coalescence of adjacent mounds (Fig. 3a), the mounds superimposed just on the faults (Figs. 3a, 4c), and the relatively high spatial density of mounds in certain areas (e.g., 61 mounds in a 13 km^2 area). Interestingly, in the middle part of the basin floor (Fig. 3c), the

four or more individual mounds spacing several hundreds of meters are distributed within the NNE-SSW trending elongated areas, sub-parallel to the long axis of the basin. This characteristic is analogous to the “alignments” of igneous and mud volcanoes on Earth (e.g., Bonini 2012).

Morphology of the mounds

Observations of HiRISE and CTX images show a variety of morphologies of the mounds. One of the most common characteristics of the mounds is a smooth surface texture relative to the surrounding rugged surface covered with blocky materials and dunes (Fig. 4), whereas brightness of the mound surfaces in visible grayscale images vary in places (Fig. 3). For instance, on the one hand, Fig. 3a reveals that the surface brightness of the mounds are almost uniform and similar to that of the surrounding areas. On the other hand, the mounds at the upper left and bottom of Fig. 3b (only several kilometers apart) show relatively dark and bright surfaces, respectively. These suggest that the materials covering the mound surfaces have different albedos on kilometer scale which may have been influenced by different grain sizes, mineral compositions, states of erosion, and etc. In addition, every mound is superposed on the surrounding terrain, supported by the appearance of smooth mound materials embaying the topographic lows of the surrounding rough surface. Some of the mounds have the circular features (mostly depressions) on their summit (Fig. 4b). Along the rims of these summit pits, clusters of meter-scale boulders can be observed.

Several mounds overlying the fissures (Fig. 4c) show the obvious morphology of deformation or degradation. This may indicate that the formation of these fractures followed the formation of the mounds at least in some locations.

A few mounds exhibit distinct flow-like features along their periphery (e.g., Fig. 4d). This is completely different from the morphology of lobate flow-like extension associated with mass movement because of the absence of typical scarps, ridges, or hummocky surfaces.

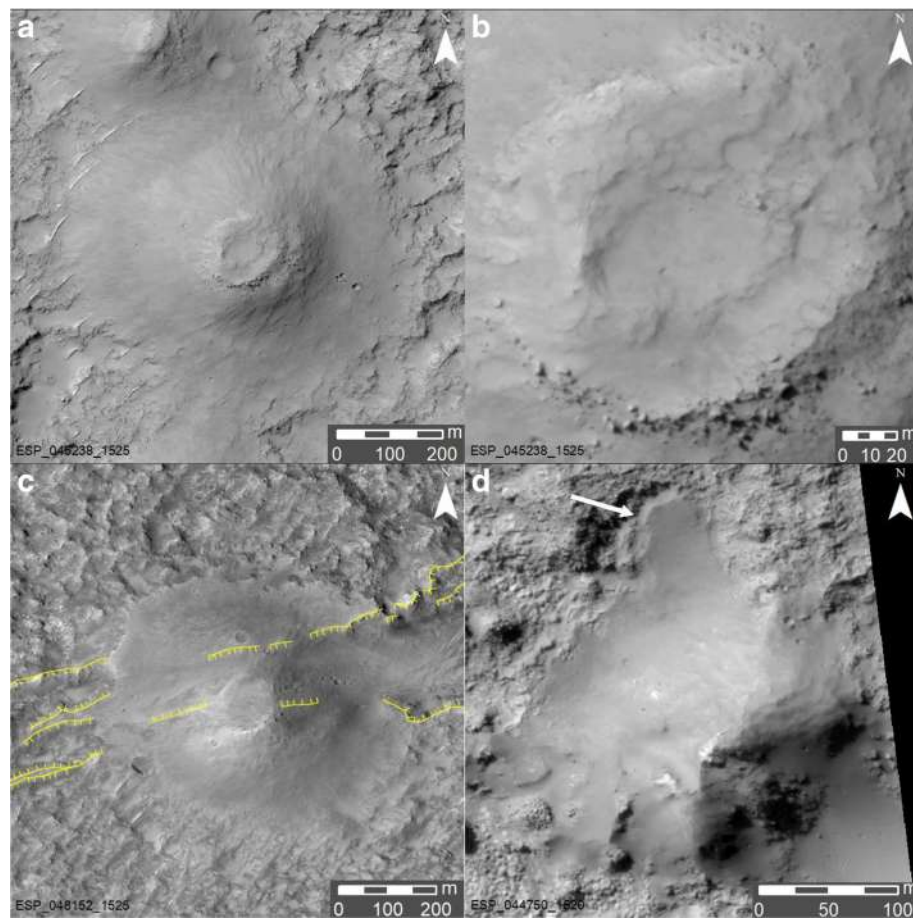


Fig. 4 General morphologic characteristics of the mounds. **a** Smooth surface texture relative to the surrounding terrain. A circular depression observed on the summit of a mound. Part of HiRISE image with illumination from the upper left. **b** Close-up of the summit depression in panel **a**. Clusters of boulders (up to 6 m wide) densely distributed along its rim. **c** A mound deformed by the underlying fissures (yellow lines) determined from the grayscale image and DEM4 (Fig. 5d). Part of HiRISE image with illumination from the upper left. **d** Distinct lobate feature (~70 m long) along the periphery of a mound (pointed by arrow). Part of HiRISE image with illumination from the upper left

Morphometry and geometry of the mounds

Morphometric parameters of 50 mounds (~6.7% of all the mounds) were measured using the four HiRISE-derived DEMs (Fig. 5). We obtained the basal diameters from 147 to 441 m (mean = 265 m, median = 245 m, SD = 77) and the maximum mound heights from 6.0 to 42.9 m (mean = 17.8, median = 16.6, SD = 8.2) with the height-to-diameter ratio of 0.034 to 0.10 (see Fig. 6 and Table 2).

Cross-sectional topographic profiles of mounds show that their summits have a wide variety of shapes: cratered summit (e.g., Fig. 7a, b), truncated summit (e.g., Fig. 7c, d), and conical summit (e.g., Fig. 7e, f). Summit depressions on some mounds have depths up to several meters, which bottoms are higher in elevation than the surrounding plains. Flanks of each mound are gently sloping, some of which are characterized by upward convex geometry (Fig. 7b, d). Slope values of each

mound suggest that most of the mounds have mean slope values lower than ~10° (Table 2), except for locations of impact craters and DEM artifacts.

Possible origin of the mounds

Circular mounds of several hundred meters in diameter sharing similar surface textures as such mounds on Mars can be found on Earth. Proposed terrestrial analog features include impact craters, scoria cones, rootless cones, tuff cones/rings, pingos, and mud volcanoes (e.g., Farrand et al. 2005; Meresse et al. 2008; Burr et al. 2009; de Pablo and Komatsu 2009; Oehler and Allen 2010; Brož et al. 2015).

Impact craters are the sites of past meteor impacts, generally found on planetary surfaces, which is a bowl-shaped depression surrounded by raised rims and radially emanating ejecta deposits. Most of the mounds exist in the absence of these characteristics. Though some of

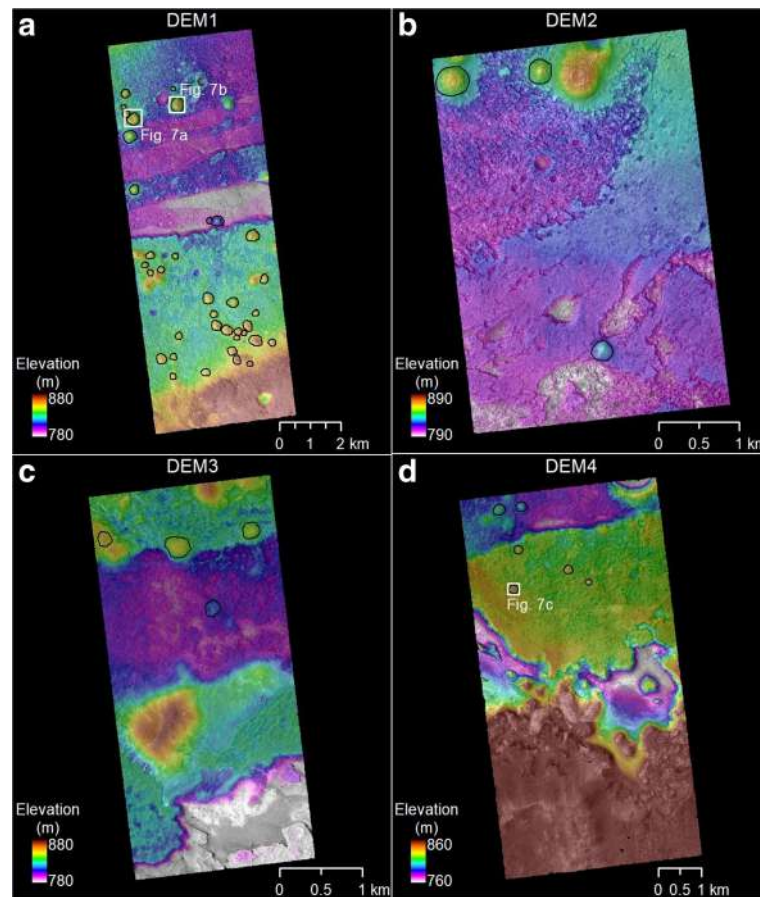


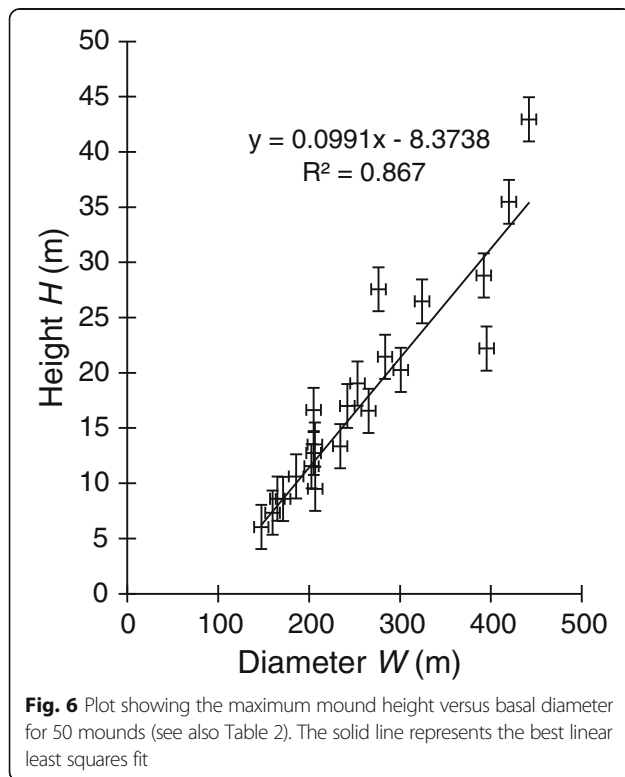
Fig. 5 Four colored DEMs draped over grayscale orthoimages. **a** DEM1. **b** DEM2. **c** DEM3. **d** DEM4. Measured mounds are marked by black outlines. See Fig. 2 and Table 1 for their locations and details, respectively

the mounds show the smooth materials overlying the surrounding terrains and distinct crater on the summit with raised rims having ejecta-like boulders (e.g. Fig. 4) similar to the morphology of typical impact craters, the depths of summit depression are too shallow to reach the elevations of the surrounding plains, which is difficult to explain the pitted mounds by the impact origin. We thus concluded that the impact origin is unlikely.

Scoria cones (also known as cinder cones) are the conical volcanic edifices formed by explosive eruptions and associated deposition of pyroclastics around individual vents. Some of the mounds show similar characteristics of typical scoria cones; however, the results of this study are also inconsistent with the scoria cone scenario. Morphology of circular terrestrial scoria cones have the mean basal diameters of 800 m and mean height of 250 m (Wood 1979), twice or more larger values than those of the mounds measured in this study (Fig. 8). Moreover, steep or flat-floored summit morphology (Fig. 7) hardly occur on the summit of scoria cones on Earth and Mars.

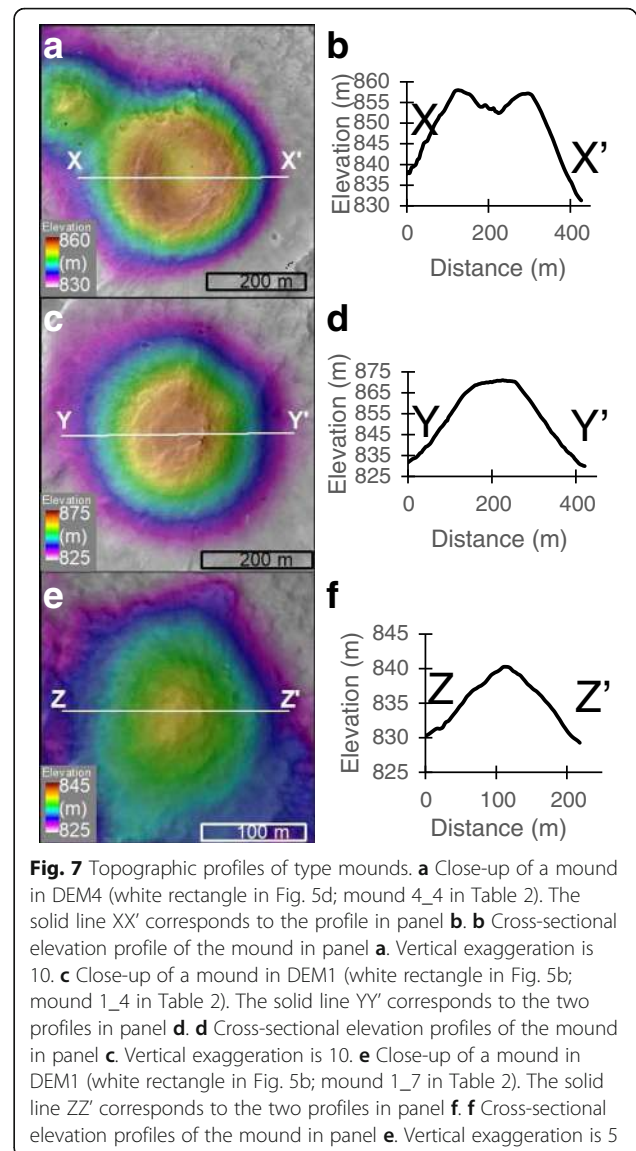
Associated lava flows found on terrestrial and Martian scoria cones (e.g., Meresse et al. 2008) are also lacking in the mound fields of this study. However, there remains the possibility that later erosional or depositional events deformed the original topography of scoria cones and produced the current morphology and topography, which cannot be conclusively determined without accurate in situ observations.

Rootless cones (or pseudo-craters) are conical or ring-like structures formed by the emplacement of lava flows over wet ground and the subsequent explosions (Greeley and Fagents 2001). Although some of the terrestrial rootless cones have the diameter range comparable to the mounds measured in this study (e.g., Noguchi and Kurita 2015; Fig. 8), there is a critical difference between them: whether mound is made of the same material as that of the surrounding plains or not. Rootless cones are constructed by the pyroclasts sourced from the underlying lava flows, so that if they form on the surface of Mars, little clear contrast in surface albedo between the cones and the surrounding plains is expected to be



formed due to their similar basaltic compositions. This contradicts that the surface brightness of some mounds differ to that of the surrounding surface in a single observation (e.g., Fig. 3b). Furthermore, terrestrial rootless cones are morphologically composed of central depressions and associated raised rims, which previously proposed rootless cones on Mars exhibit (e.g., Greeley and Fagents 2001); however, some of the studied mounds do not have any summit depression but rather conical summits (e.g., Fig. 7e, f). Thus, it is not reasonable to interpret all of the target mounds as rootless cones.

Pingos are periglacial landforms formed by uplift of the ground surface due to freezing of groundwater, development of subsurface ice lenses, and subsequent increase in bulk volume (Mackay 1979). The morphometry and summit morphology of pingos, as suggested by Jones et al. (2012), are consistent with these of the mounds in our study. However, these processes of pingo formation are expected to produce domical features with same surface textures as the surrounding plains, which is contrary to the difference in surface texture between the mounds and the basin floor (Fig. 3b). In addition, evident fractured surfaces, which pingo candidates on Mars (Dundas and McEwen 2010) exhibit, were not observed in any of the mounds. Martian equivalent also have 175 m diameter and ~10 to ~20 m height (Dundas and McEwen 2010),



which is slightly higher than the observed mounds with similar diameters in this study. We therefore propose that pingo origin is a less plausible explanation for the formation of the mounds.

Tuff rings, tuff cones, and maars are volcanic craters/cones with topographic rims, which result from phreatomagmatic explosions (i.e., the interaction between groundwater/standing water and magmatic intrusions). These terrestrial cones/rings and Martian tuff rings/cones (Brož and Hauber 2013) have basal diameters one or more orders of magnitude larger than the mounds measured in this study (Fig. 8). Furthermore, large summit craters with high crater-to-base ratios (Pike and Clow 1981) are also not common characteristics in the mounds. Therefore, we concluded the phreatomagmatic

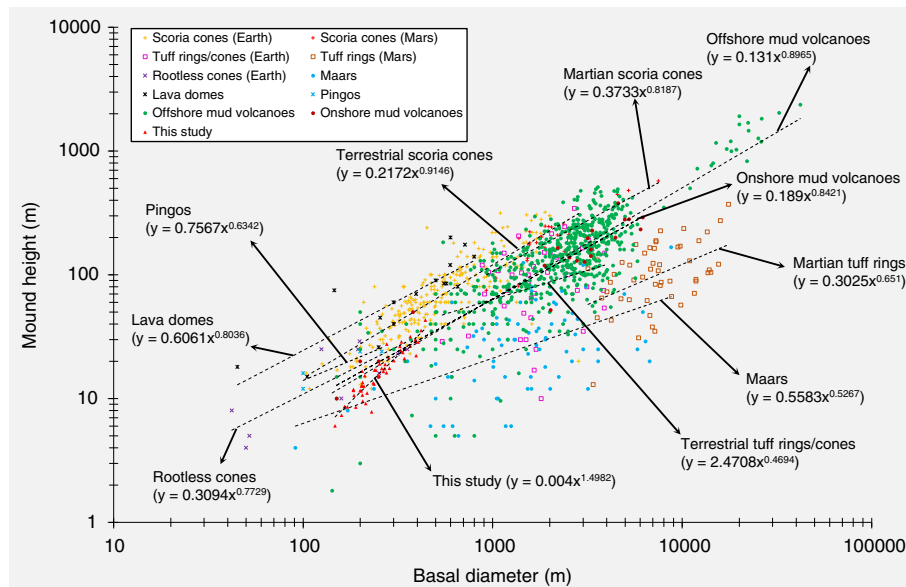


Fig. 8 Morphometric comparison between the measured mounds and other terrestrial analogs. Log-log plots showing mound height versus basal diameter. Dashed lines represent the best linear least squares fits of parameters of each feature. Terrestrial analogs with height and diameter values used for morphometric comparison are offshore mud volcanoes on Earth (Kioka and Ashi 2015; Kirkham et al. 2017), onshore mud volcanoes on Earth (Chigira and Tanaka 1997; Brož and Hauber 2013), potential tuff rings and cones on Mars (Brož and Hauber 2013), potential scoria cones on Mars (Brož et al. 2015), terrestrial maars (Pike 1978), terrestrial lava domes (Pike 1978), terrestrial cinder/scoria cones (Pike 1978; Favalli et al. 2009; Rodríguez et al. 2010), terrestrial pingos (Cabrol et al. 2000), terrestrial tuff rings/cones (Pike 1978), and terrestrial rootless cones (Pike 1978). Morphometric data of elongated (not circular) mounds is not used. Mound maximum height is preferentially used as mound height if available

explosions creating volcanic edifices are less likely origins of the mounds in the basin.

Mud volcanoes are the surface manifestation of mixtures of sediments (e.g., silts, fine sands, brecciated materials) and fluids (i.e., liquid water and gas) migrated upwards from source reservoirs up to several kilometers deep, which can produce a variety of morphologies (e.g., conical mounds, calderas, pools, diapiric intrusions, mud flows) along terrestrial regional compressional fields, mostly subduction zones on a global scale (e.g., Milkov 2000; Kopf 2002). The observations of mound depressions, boulders on the rims, and flow-like features can be interpreted as vent-like structures of the subsurface conduits, mud breccias, and mud flows of typical mud volcanoes on Earth, respectively. The various morphology of cone summits on mud volcanoes in cross-section, reported in Yusifov and Rabinowitz (2004), well correspond to the observations of cone morphologies in Fig. 7.

As summarized in Fig. 8, offshore (submarine) mud volcanoes have the wide range of the morphometric parameters (100 m to 10 km in diameter and several meters to kilometers in height), and these are well consistent with those of onshore mud volcanoes. This suggests that the condition of ambient fluid (i.e., air or liquid water) during mound formation do not affect the final size and topography of the mounds critically. In fact, Murton and

Biggs (2003) argued that mud flow spreading across seafloor is driven by the “reduced gravity” (g') which is proportional to the product of surface gravity and the density contrast between seawater and mud. They theoretically established that the mound radius and height are proportional to the eighth root of g' and inversely proportional to the fourth root of g' respectively, so that the surface gravity and density (or pressure) of ambient materials are minor contributor relative to the other conditions (e.g., rheology of mud, flow rate, eruption duration). Therefore, if mud volcanoes formed on the free air or underwater conditions of Mars by the eruption of mud having the same flux as the terrestrial ones, they are expected to show similar morphometry to those of both subaqueous and subaerial mud volcanoes on Earth. Importantly, the smaller range of both onshore and offshore mud volcanoes (~100 to ~500 m diameters) have the heights of 1 to 50 m, which is consistent with the heights of the investigated mounds of this study (Fig. 8). Thus, if they are of a mud volcanic origin, both subaerial and subaqueous conditions are possible to explain the origin of the investigated mounds on Mars and difficult to distinguish which condition existed during the periods of mound formation.

The inconsistency between the studied mounds and the other analog features are quite difficult to accurately

interpret due to different formation ages, different erosion rates, different properties of terrain underlying the mounds (e.g., thickness, bulk soil density), and different surface gravity; however, at least Martian mud volcanoes would not be expected to plot closely with Martian scoria cones, Martian tuff rings/cones, or Martian maars (if existed) in Fig. 8. This is because under low gravity and low atmospheric pressures on Mars surface, larger cone diameters and lower cone heights than those on Earth are expected due to the wider ranges of scoria distribution by far-reaching ballistic emplacement (Wilson and Head 1994; Brož et al. 2015). Actually, the morphometries of candidates of Martian scoria cones (Brož et al. 2015) and Martian tuff rings/cones (Brož and Hauber 2013) are plotted in the larger diameters than the terrestrial equivalents, and they are plotted in different way from that of the observed mounds in this study (Fig. 8). Although the plots in Fig. 8 do not thoroughly compiled all of the previously obtained data, most of the ranges and the trends would not be expected to change significantly. Though exact locations of potential Martian maars have not been reported ever before, they would be expected to be plotted in the larger diameter ranges if they formed on Mars because of the similar mechanism of spatter emplacement to that of scoria cones under low gravity and thinner atmosphere than those of Earth. Data of terrestrial lava domes, terrestrial rootless cones, and terrestrial pingos are not completely compiled in Fig. 8; however, their morphology are completely different from the that of the mud volcanoes and the targeted mounds of this study, so that they are readily discernable even if they have morphometric parameters to those of the studied mounds.

Based on the above discussions, we propose the mud volcanism best explains the origins of the circular mounds in the study area. If such mounds are formed through mud volcanisms, the large amount of clay minerals, aquifers maintained perhaps under moderate heat fluxes, tectonic stresses, and generation of hydrocarbon gases may have occurred within the subsurface below this basin floor for at least limited periods, which would be of great significance in the context of astrobiology. Hence, this basin and mounds can be one of the best candidate sites for future landing exploration.

Surface model age determination

The cumulative plots of the CSFD, based on the crater counts on the sample region of the southern highlands including the basin (Fig. 9a, b), show the surface model age of 4.0 Ga, well consistent with previously described geological units of early Noachian southern highlands (Platz et al. 2013; Tanaka et al.

2014). In contrast, the model age estimates of the upper rugged unit of the basin floor (Fig. 9c, d) is relatively young. A chronology function fitted to the population of impact craters (more than 1.2 km across) provides the estimated value of 3.5 Ga. This age is comparable to the values of some areas of the surrounding highland plains (Platz et al. 2013). In addition, the application of resurfacing correction to the CSFDs of two smaller diameter ranges, 0.6–1.0 km and 150–500 m, provides the age estimates of 2.9 Ga (Hesperian/Amazonian boundary (Hartmann 2005)) and 1.2 Ga (early Amazonian), respectively (Fig. 9d).

Formational history of the basin environments forming mud volcanoes

Based on the combinations of model ages and the cross-cutting and stratigraphic relationship of geological units and structures, we provide a simple consistent explanation for the formational scenario of Terra Sirenum, the elongated basin, the basin floor, the circular mounds, and the fractures of Memnonia Fossae: (1) heavy bombardment events cratered the northern part of past Terra Sirenum area and formed the chains of several basin structure around ~4.0 Ga (pre-elongated basin), (2) several cratered surfaces were integrated into an elongated trough-like structure at ~3.5 Ga by degradational processes (formation of lowermost basement unit), (3) subsequent infilling of the fluid-laden sediments into the elongated basin, possibly sourced from faults along Memnonia Fossae via upwelling groundwater melted by dike intrusion (Wilson and Head 2002), (4) sedimentary layers with interbedded bright materials (Wray et al. 2011) formed by evaporation (formation of lower rugged unit), (5) local east-west compressional stresses with long-term sediment loading caused overpressurization of groundwater at depth, opened conduits for triggering mud extrusions onto the surface, and deformed some of the mud volcanoes during Hesperian/Amazonian periods, (6) aeolian activities partially buried and excavated the basin interior from Amazonian to date (formation of upper rugged unit).

Additional high-resolution spectral data coverage obtained by the MRO spacecraft in the future will improve mineralogical characterization of the mounds and further discussions of possible diagenetic processes and/or hydrothermal alteration.

Conclusions

We examined the distribution, stratigraphic relationship, morphologies, and morphometric parameters of the circular mounds in the elongated basin of the northern Terra Sirenum. Though an eroded volcanic cone origin cannot

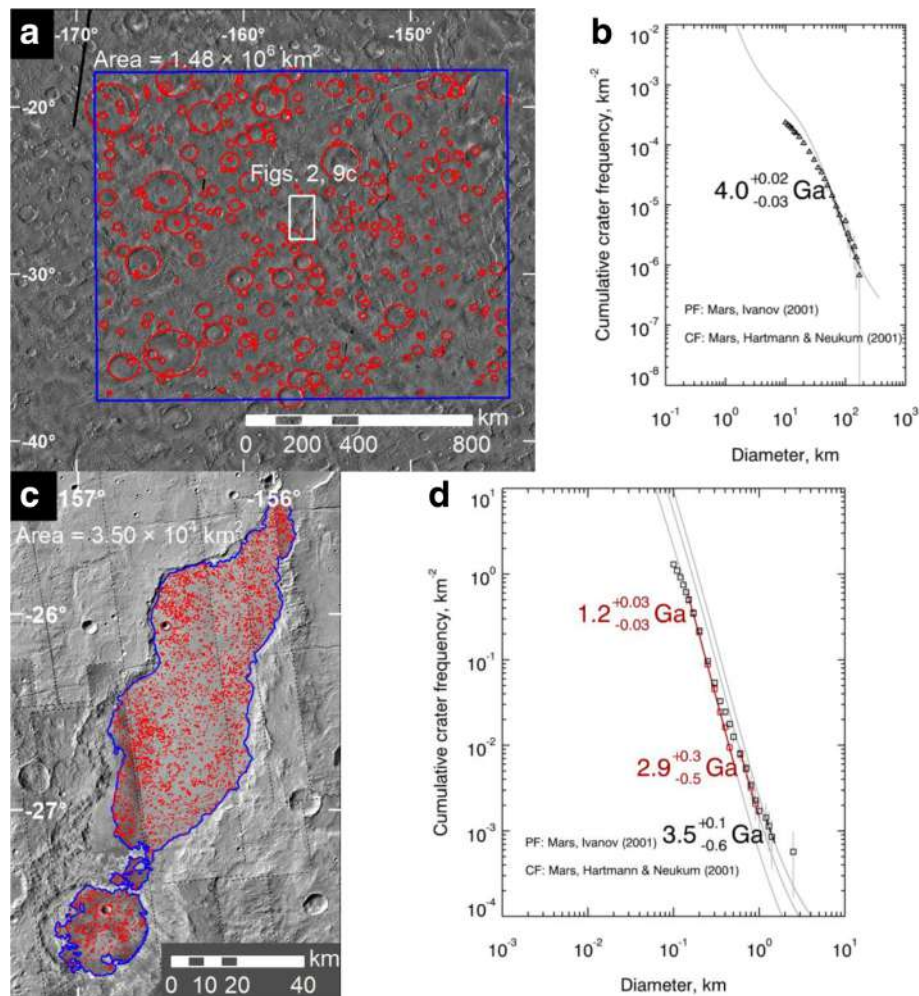


Fig. 9 Crater count-based model age determination. **a, b** Part of northern Terra Sirenum (Fig. 1) (**c, d**), the upper rugged unit (Fig. 2c). **a** Mapped impact craters with diameters > 10 km (red circles) on a sample region (blue rectangle) surrounding the study area (white rectangle). Base map is from the daytime THEMIS infrared image mosaic (100 m/pixel) which was used to mark the craters. Solar illumination is from the left of the scene. **b** Cumulative size-frequency plot of the impact craters of > 100 m diameter ($N = 348$). Production function curve is fitted to the diameter range of 50 to 175 km. **c** Identified impact craters > 100 m diameters (red circles, $N = 4549$) on the upper rugged unit (blue outlines). The CTX image mosaic (base map) was used to map the craters. **d** Cumulative crater size-frequency distribution and absolute model ages. Production functions fitted to the three ranges of the crater diameters: 1.2–1.5 km (black), 0.6–1.0 km (red), and 150–500 m (red). Red plots indicate the resurfacing correction (Michael and Neukum 2010)

be ruled out, the combination of their distribution and meter-scale morphology with their morphometry favors a mud volcano origin. If the mud volcano hypothesis is true, their relatively young surfaces suggest that the formation of source reservoirs and conduit openings along regional fissures for erupting mud and groundwater might have occurred during more recent times than Noachian age. This is consistent with other post-Noachian features in the region such as outflow channels which are linked to faults.

Abbreviations

ASP: Ames Stereo Pipeline; CTX: Context Camera; DEM(s): Digital elevation model(s); GDAL: Geospatial Data Abstraction Library; GIS: Geographic Information System; HiRISE: High Resolution Imaging Science Experiment;

ISIS: Integrated Software for Imagers and Spectrometers; JMARS: Java Mission-planning and Analysis for Remote Sensing; MEGDRs: Mission Experiment Gridded Data Records; MGS: Mars Global Surveyor; MOLA: Mars Orbiter Laser Altimeter; MRO: Mars Reconnaissance Orbiter; NASA: National Aeronautics and Space Administration; PEDRs: Precision Experiment Data Records; THEMIS: Thermal Emission Imaging System; USGS: United States Geological Survey

Acknowledgements

We thank HiRISE and CTX science teams for producing a number of publicly available, high-resolution image datasets. We also appreciate the developers of USGS's ISIS and Arizona State University's JMARS for enabling us to handle Mars image datasets. We are grateful to NASA Ames Stereo Pipeline developers for creating an open-source software used to generate DEMs. We acknowledge Trent Hare, Elphia Howington-Kraus, Ross Beyer, Oleg Alexandrov, and Zachary Morato for their helpful comments on DEM extraction and GIS-based processing, and James M. Dohm for preliminary discussions. The detailed reviews by Chris Okubo and an anonymous reviewer improved the clarity of the

manuscript and are greatly appreciated. This work has been supported by JSPS KAKENHI Grant Numbers 23340126, 25120006, 15K21718, 16K13890, and 17H02953. We appreciate the Space Museum TeNQ/TOKYO DOME CORPORATION for their great support of the branch of Space Exploration, Education, and Discovery (SEED), the University Museum, the University of Tokyo.

Funding

Not applicable.

Authors' contributions

RH proposed the topic, conceived and designed the study, analyzed the data, and interpreted the results. HM collaborated with RH in the discussion and construction of the manuscript. All authors read and approved the final manuscript.

Competing interests

The authors declare that they have no competing interest.

Publisher's Note

Springer Nature remains neutral with regard to jurisdictional claims in published maps and institutional affiliations.

Received: 31 March 2017 Accepted: 31 August 2017

Published online: 11 September 2017

References

- Becker KJ, Archinal BA, Hare TH, Kirk RL, Howington-Kraus E, Robinson MS, Rosiek MR (2015) Criteria for automated identification of stereo image pairs. In: Abstracts of the 46th Lunar and Planetary Science Conference, 2015, The Woodlands, Texas, p 2703.
- Beddingfield CB, Burr DM, Emery JP (2015) Fault geometries on Uranus' satellite Miranda: implications for internal structure and heat flow. *Icarus* 247:35–52. doi:10.1016/j.icarus.2014.09.048
- Beyer RA, Alexandrov O, Moratto ZM (2014) Aligning terrain model and laser altimeter point clouds with the Ames Stereo Pipeline. In: Abstracts of the 45th Lunar and Planetary Science Conference, 2014, The Woodlands, Texas, p 2902
- Bonini M (2012) Mud volcanoes: indicators of stress orientation and tectonic controls. *Earth Sci Rev* 115:121–152. doi:10.1016/j.earscirev.2012.09.002
- Broxton MJ, Edwards LJ (2008) The Ames Stereo Pipeline: automated 3D surface reconstruction from orbital imagery. In: Abstracts of the 39th Lunar and Planetary Science Conference, 2008, League City, Texas, p 2419
- Brož P, Hauber E (2013) Hydrovolcanic tuff rings and cones as indicators for phreatomagmatic explosive eruptions on Mars. *Journal of Geophysical Research: Planets* 118:1656–1675. doi:10.1002/jgre.20120
- Brož P, Čadež O, Hauber E, Rossi AP (2015) Scoria cones on Mars: Detailed investigation of morphometry based on high-resolution digital elevation models. *Journal of Geophysical Research: Planets* 120:1512–1527. doi:10.1002/2015JE004873
- Burr DM, Bruno BC, Lanagan PD, Glaze LS, Jaeger WL, Soare RJ, Tseung J-MWB, Skinner JA, Baloga SM (2009) Mesoscale raised rim depressions (MRRDs) on Earth: a review of the characteristics, processes, and spatial distributions of analogs for Mars. *Planet Space Sci* 57:579–596. doi:10.1016/j.pss.2008.11.011
- Cabrol NA, Grin EA, Pollard WH (2000) Possible frost mounds in an ancient Martian lake bed. *Icarus* 145:91–107. doi:10.1006/icar.1999.6326
- Chigira M, Tanaka K (1997) Structural features and the history of mud volcanoes in southern Hokkaido, northern Japan. *J Geol Soc Jpn* 103:781–791. doi:10.5575/geosoc.103.781
- Christensen PR, Jakosky BM, Kieffer HH, Malin MC, McSween HY, Nealon K, Mehall GL, Silverman SH, Ferry S, Caplinger M (2004) The Thermal Emission Imaging System (THEMIS) for the Mars 2001 Odyssey Mission. *Space Sci Rev* 110:85–130. doi:10.1023/B:SPAC.0000021008.16305.94
- Clifford SM, Parker TJ (2001) The evolution of the Martian hydrosphere: implications for the fate of a primordial ocean and the current state of the northern plains. *Icarus* 154:40–79. doi:10.1006/icar.2001.6671
- de Pablo MÁ, Komatsu G (2009) Possible pingo fields in the Utopia basin, Mars: geological and climatic implications. *Icarus* 199:49–74. doi:10.1016/j.icarus.2008.09.007
- Dundas CM, McEwen AS (2010) An assessment of evidence for pingos on Mars using HiRISE. *Icarus* 205:244–258. doi:10.1016/j.icarus.2009.02.020
- Ehlmann BL, Berger G, Mangold N, Michalski JR, Catling DC, Ruff SW, Chassefière E, Niles PB, Chevrier V, Poulet F (2013) Geochemical consequences of widespread clay mineral formation in Mars' ancient crust. *Space Sci Rev* 174:329–364. doi:10.1007/s11214-012-9930-0
- Farrand WH, Gaddis LR, Keszthelyi L (2005) Pitted cones and domes on Mars: observations in Acidalia Planitia and Cydonia Mensae using MOC, THEMIS, and TES data. *Journal of Geophysical Research: Planets* 110:E05005. doi:10.1029/2004JE002297
- Favalli M, Karátson D, Mazzarini F, Pareschi MT, Boschi E (2009) Morphometry of scoria cones located on a volcano flank: a case study from Mt. Etna (Italy), based on high-resolution LiDAR data. *J Volcanol Geotherm Res* 186:320–330. doi:10.1016/j.jvolgeores.2009.07.011
- Ferguson RL, Lee EM, Weller L (2013) THEMIS geodetically controlled mosaics of Mars. In: Abstracts of the 44th Lunar and Planetary Science Conference, 2013, The Woodlands, Texas, p 1642
- Glotch TD, Bandfield JL, Tornabene LL, Jensen HB, Seelos FP (2010) Distribution and formation of chlorides and phyllosilicates in Terra Sirenum, Mars. *Geophys Res Lett* 37:L16202. doi:10.1029/2010GL044557
- Greeley R, Fagents SA (2001) Icelandic pseudocraters as analogs to some volcanic cones on Mars. *Journal of Geophysical Research: Planets* 106:20527–20546. doi:10.1029/2000JE001378
- Crater Analysis Techniques Working Group (1979) Standard techniques for presentation and analysis of crater size-frequency data. *Icarus* 37:467–474. doi:10.1016/0019-1035(79)90009-5
- Hartmann WK (2005) Martian cratering 8: isochron refinement and the chronology of Mars. *Icarus* 174:294–320. doi:10.1016/j.icarus.2004.11.023
- Hartmann WK, Neukum G (2001) Cratering chronology and the evolution of Mars. *Space Sci Rev* 96:165–194. https://doi.org/10.1023/A:1011945222010
- Head JW, Kreslavsky MA, Pratt S (2002) Northern lowlands of Mars: evidence for widespread volcanic flooding and tectonic deformation in the Hesperian Period. *Journal of Geophysical Research: Planets* 107:3-1-3-29. doi:10.1029/2000JE001445
- Ivanov BA (2001) Mars/moon cratering rate ratio estimates. *Space Sci Rev* 96:87–104. doi:10.1023/A:1011941121102
- Jones BM, Grosse G, Hinkel KM, Arp CD, Walker S, Beck RA, Galloway JP (2012) Assessment of pingo distribution and morphometry using an IfSAR derived digital surface model, western Arctic Coastal Plain, Northern Alaska. *Geomorphology* 138:1–14. doi:10.1016/j.geomorph.2011.08.007
- Kioka A, Ashi J (2015) Episodic massive mud eruptions from submarine mud volcanoes examined through topographical signatures. *Geophys Res Lett* 42:8406–8414. doi:10.1002/2015GL065713
- Kirk RL, Howington-Kraus E, Rosiek MR, Anderson JA, Archinal BA, Becker KJ, Cook DA, Galuszka DM, Geissler PE, Hare TM, Holmberg IM, Keszthelyi LP, Redding BL, Delamere WA, Gallagher D, Chapel JD, Eliason EM, King R, McEwen AS (2008) Ultrahigh resolution topographic mapping of Mars with MRO HiRISE stereo images: meter-scale slopes of candidate Phoenix landing sites. *Journal of Geophysical Research: Planets* 113:E00A24. doi:10.1029/2007JE003000
- Kirkham C, Cartwright J, Hermanrud C, Jebson C (2017) The spatial, temporal and volumetric analysis of a large mud volcano province within the Eastern Mediterranean. *Mar Pet Geol* 81:1–16. doi:10.1016/j.marpetgeo.2016.12.026
- Kneissl T, van Gasselt S, Neukum G (2011) Map-projection-independent crater size-frequency determination in GIS environments—new software tool for ArcGIS. *Planet Space Sci* 59:1243–1254. doi:10.1016/j.pss.2010.03.015
- Kopf AJ (2002) Significance of mud volcanism. *Rev Geophys* 40:2-1-2-52. doi:10.1029/2000RG000093
- Mackay JR (1979) Pingos of the Tuktoyaktuk peninsula area, Northwest territories. *Géog Phys Quatern* 33:3–61. doi:10.7202/1000322ar
- Malin MC, Bell JF, Cantor BA, Caplinger MA, Calvin WM, Clancy RT, Edgett KS, Edwards L, Haberle RM, James PB, Lee SW, Ravine MA, Thomas PC, Wolff MJ (2007) Context Camera investigation on board the Mars Reconnaissance Orbiter. *Journal of Geophysical Research: Planets* 112:E05504. doi:10.1029/2006JE002808
- McEwen AS, Eliason EM, Bergstrom JW, Bridges NT, Hansen CJ, Delamere WA, Grant JA, Gulick VC, Herkenhoff KE, Keszthelyi L, Kirk RL, Mellon MT, Squyres SW, Thomas N, Weitz CM (2007) Mars Reconnaissance Orbiter's High Resolution Imaging Science Experiment (HiRISE). *Journal of Geophysical Research: Planets* 112:E05502. doi:10.1029/2005JE002605
- Meresse S, Costard F, Mangold N, Masson P, Neukum G (2008) Formation and evolution of the chaotic terrains by subsidence and magmatism: Hydrates Chaos, Mars. *Icarus* 194:487–500. doi:10.1016/j.icarus.2007.10.023
- Michael GG, Neukum G (2010) Planetary surface dating from crater size–frequency distribution measurements: partial resurfacing events and statistical age uncertainty. *Earth Planet Sci Lett* 294:223–229. doi:10.1016/j.epsl.2009.12.041

- Michalski JR, Dobrea EZN, Niles PB, Cuadros J (2017) Ancient hydrothermal seafloor deposits in Eridania basin on Mars. *Nat Commun* 8:15978. doi:10.1038/ncomms15978
- Milkov AV (2000) Worldwide distribution of submarine mud volcanoes and associated gas hydrates. *Mar Geol* 167:29–42. doi:10.1016/S0025-3227(00)00022-0
- Moratto ZM, Broxton MJ, Beyer RA, Lundy M, Husmann K (2010) Ames Stereo Pipeline, NASA's open source automated stereogrammetry software. In: Abstracts of the 41st Lunar and Planetary Science Conference, 2010, The Woodlands, Texas, p 2364
- Murton BJ, Biggs J (2003) Numerical modelling of mud volcanoes and their flows using constraints from the Gulf of Cadiz. *Mar Geol* 195:223–236. doi:10.1016/S0025-3227(02)00690-4
- Noguchi R, Kurita K (2015) Unique characteristics of cones in Central Elysium Planitia, Mars. *Planet Space Sci* 111:44–54. doi:10.1016/j.pss.2015.03.007
- Oehler DZ, Allen CC (2010) Evidence for pervasive mud volcanism in Acidalia Planitia, Mars. *Icarus* 208:636–657. doi:10.1016/j.icarus.2010.03.031
- Okubo CH (2016) Morphologic evidence of subsurface sediment mobilization and mud volcanism in Candor and Coprates Chasmata, Valles Marineris, Mars. *Icarus* 269:23–37. doi:10.1016/j.icarus.2015.12.051
- Pike RJ (1978) Volcanoes on the inner planets: some preliminary comparisons of gross topography. In: Proceedings of the 9th Lunar and Planetary Science Conference, 1978, Houston, Texas, pp 3239–3273.
- Pike RJ, Clow GD (1981) Revised classification of terrestrial volcanoes and catalog of topographic dimensions, with new results of edifice volume. U. S. Geological Survey Open-File Report 81–1038
- Platz T, Michael G, Tanaka KL, Skinner JA, Fortezzo CM (2013) Crater-based dating of geological units on Mars: methods and application for the new global geological map. *Icarus* 225:806–827. doi:10.1016/j.icarus.2013.04.021
- Pondrelli M, Rossi AP, Ori GG, Van Gasselt S, Praeg D, Ceramicola S (2011) Mud volcanoes in the geologic record of Mars: the case of Firsoff crater. *Earth Planet Sci Lett* 304:511–519. doi:10.1016/j.epsl.2011.02.027
- Rodríguez SR, Morales-Barrera W, Layer P, González-Mercado E (2010) A quaternary monogenetic volcanic field in the Xalapa region, eastern trans-Mexican volcanic belt: geology, distribution and morphology of the volcanic vents. *J Volcanol Geotherm Res* 197:149–166. doi:10.1016/j.jvolgeores.2009.08.003
- Shean DE, Alexandrov O, Moratto ZM, Smith BE, Joughin IR, Porter C, Morin P (2016) An automated, open-source pipeline for mass production of digital elevation models (DEMs) from very-high-resolution commercial stereo satellite imagery. *ISPRS J Photogramm Remote Sens* 116:101–117. doi:10.1016/j.isprsjprs.2016.03.012
- Smith DE, Zuber MT, Frey HV, Garvin JB, Head JW, Muhleman DO, Pettengill GH, Phillips RJ, Solomon SC, Zwally HJ (2001) Mars Orbiter Laser Altimeter: experiment summary after the first year of global mapping of Mars. *Journal of Geophysical Research: Planets* 106:23689–23722. doi:10.1029/2000JE001364
- Tanaka KL, Chapman MG (1990) The relation of catastrophic flooding of Mangala Valles, Mars, to faulting of Memnonia Fossae and Tharsis Volcanism. *J Geophys Res Solid Earth* 95:14315–14323. doi:10.1029/JB095iB09p14315
- Tanaka KL, Skinner JA, Hare TM (2005) Geologic map of the northern plains of Mars. In: U.S. Geological Survey Scientific Investigations Map 2888
- Tanaka KL, Skinner JAJ, Dohm JM, Irwin Iii RP, Kolb EJ, Fortezzo CM, Platz T, Michael GG, Hare T (2014) Geologic map of Mars, Scale 1:20,000,000. In: U.S. Geological Survey Scientific Investigations Map 3292.
- Wilson L, Head JW (1994) Mars: review and analysis of volcanic eruption theory and relationships to observed landforms. *Rev Geophys* 32:221–263. doi:10.1029/94RG01113
- Wilson L, Head JW (2002) Tharsis-radial graben systems as the surface manifestation of plume-related dike intrusion complexes: models and implications. *Journal of Geophysical Research: Planets* 107:1–1–24. doi:10.1029/2001JE001593
- Wood CA (1979) Monogenetic volcanoes of the terrestrial planets. In: Proceedings of the 10th Lunar and Planetary Science Conference, 1979, Houston, Texas, pp 2815–2840.
- Wray JJ, Milliken RE, Dundas CM, Swayze GA, Andrews-Hanna JC, Baldrige AM, Chojnacki M, Bishop JL, Ehlmann BL, Murchie SL, Clark RN, Seelos FP, Tornabene LL, Squyres SW (2011) Columbus crater and other possible groundwater-fed paleolakes of Terra Sirenum, Mars. *Journal of Geophysical Research: Planets* 116:E01001. doi:10.1029/2010JE003694
- Yusifov M, Rabinowitz PD (2004) Classification of mud volcanoes in the South Caspian Basin, offshore Azerbaijan. *Mar Pet Geol* 21:965–975. doi:10.1016/j.marpetgeo.2004.06.002

Submit your manuscript to a SpringerOpen[®] journal and benefit from:

- Convenient online submission
- Rigorous peer review
- Open access: articles freely available online
- High visibility within the field
- Retaining the copyright to your article

Submit your next manuscript at ► springeropen.com

Chapter 4

High-resolution Topographic Analyses of Mounds in Southern Acidalia Planitia, Mars: Implications for Possible Mud Volcanism in Submarine and Subaerial Environments

The content of this chapter was peer-reviewed and published as a research article in *Geosciences* by MDPI in 2018. The author retains its copyright. MDPI allows the use of the paper in the author's dissertation, and its published version can be deposited in the author's institutional repository.

Article information:

Hemmi, R., Miyamoto, H., 2018. High-resolution topographic analyses of mounds in southern Acidalia Planitia, Mars: Implications for possible mud volcanism in submarine and subaerial environments. *Geosciences*. 8(5), 152, DOI: 10.3390/geosciences8050152.

Article

High-Resolution Topographic Analyses of Mounds in Southern Acidalia Planitia, Mars: Implications for Possible Mud Volcanism in Submarine and Subaerial Environments

Ryodo Hemmi ^{1,*}  and Hideaki Miyamoto ^{1,2}¹ The University Museum, The University of Tokyo, 7-3-1 Hongo, Bunkyo-ku, Tokyo 113-8656, Japan² Department of Systems Innovation, School of Engineering, The University of Tokyo, 7-3-1 Hongo, Bunkyo-ku, Tokyo 113-8656, Japan; hm@sys.t.u-tokyo.ac.jp

* Correspondence: hemmi@seed.um.u-tokyo.ac.jp; Tel.: +81-3-3817-6842

Received: 29 March 2018; Accepted: 25 April 2018; Published: 27 April 2018



Abstract: A northern ocean of Mars is still debated and, if it existed, it may have accompanied valley networks and/or outflow channels, which may have led to the emplacement of a large amount of water to the northern lowlands during the Noachian and/or Hesperian times. However, it is unclear how and under what conditions (submarine or subaerial) geologic features such as mounds and giant polygons formed in the northern lowlands. The densely-distributed mounds in Chryse and Acidalia Planitia, >1000 km-wide basins of the northern plains, were suggested to be ancient mud volcanoes formed in an aqueous setting, which is controversial (i.e., mud vs. igneous and submarine vs. subaerial). However, these mounds have not been quantitatively well characterized, particularly with respect to their detailed topography. Here we generated forty digital elevation models (DEMs) with resolution of up to 1 m/pixel from High Resolution Imaging Science Experiment (HiRISE) stereo image pairs, and we accurately measured the morphometric parameters of ~1300 mounds within the southern part of the Acidalia basin. Their heights and diameters resulted in good accordance with those of mud and igneous volcanoes in submarine/subaerial settings on Earth. Maximum depths of their source reservoirs vary from ~30 to ~450 m for a subaqueous setting and from ~110 to ~860 m for a subaerial setting, both of which are consistent with fluid expulsion from the ~100–4500 m-thick flood deposits (Vastitas Borealis Formation, VBF). On the basis of the morphometric values, we estimated rheological properties of materials forming the mounds and found them consistent with a mud flow origin, which does not rule out an igneous origin. The conditions of possible submarine mud or igneous volcanoes may have harbored less hazardous environments for past life on Mars than those on an ocean-free surface.

Keywords: Mars; Acidalia Planitia; pitted mounds; HiRISE; digital elevation model; mud volcanism; submarine volcanism

1. Introduction

While liquid surface water is physically not stable under the current Martian climate, the former presence of a northern ocean (or northern oceans) has been proposed for the northern lowlands since either the Noachian [1,2] or the Hesperian [2–4]. There are two major views: (1) the valley networks, formed by the long-term hydrological cycle of a warm, wet climate during the Noachian, may have been associated with a persistent ocean [1]; (2) the Hesperian-aged cataclysmic floods, suggested by outflow channels debouching into the northern lowlands [5], may have left behind large amounts of water and sediments forming the northern ocean [6]. Observational evidence for their

marine sediments comes from the Vastitas Borealis Formation (VBF)—a roughly uniform sedimentary unit with an extent approximately equal to the northern lowlands [7–9]. The population of fresh craters superimposing the VBF suggests that it is the late Hesperian in age, and the surface roughness of underlying Hesperian-aged ridged plains indicates that the minimum average thickness of the VBF is ~100 m [9,10]. The lowest putative shoreline (Contact 2 or Deuteronilus shoreline [2–4]) encompasses most of the VBF and is much closer to the current equipotential surface of Mars at around −3760 m [6,11]. Ivanov et al. [12] conducted an extensive analysis of the shoreline and VBF and dated the Deuteronilus contact (VBF) to ~3.6 gigayears (Gyr) ago. Citron et al. [13] estimated the Arabia (the early Noachian period) and Deuteronilus (the early Hesperian period) ocean volumes of $\geq 4.1 \times 10^7 \text{ km}^3$ and $\geq 1.2 \times 10^7 \text{ km}^3$, respectively. Importantly, while various workers have hypothesized and tested these oceans and shorelines, a Noachian ocean does not contradict a Hesperian ocean and how long the northern oceans have persisted is uncertain.

The most prominent outflow channels are distributed around southern Chryse Planitia, and floods were estimated to have formed these circum-Chryse outflow channels and brought at least $6 \times 10^6 \text{ km}^3$ of water (assuming ~40% of sediment by volume) [14] or much more water (assuming lower sediment loads, such as 0.1% by volume of sediment, which is the case on Earth) [15] to the Chryse-Acidalia Embayment [16] (Figure 1). The VBF surfaces within the Acidalia basin have distinct textural features, such as polygonal fractures (or giant polygons) [17], mottled patterns (e.g., bright craters, cones, patches), and mounds with summit pits [6]. The puzzling issues are the conditions, timing, and processes that formed these mounds with this suite of characteristics.

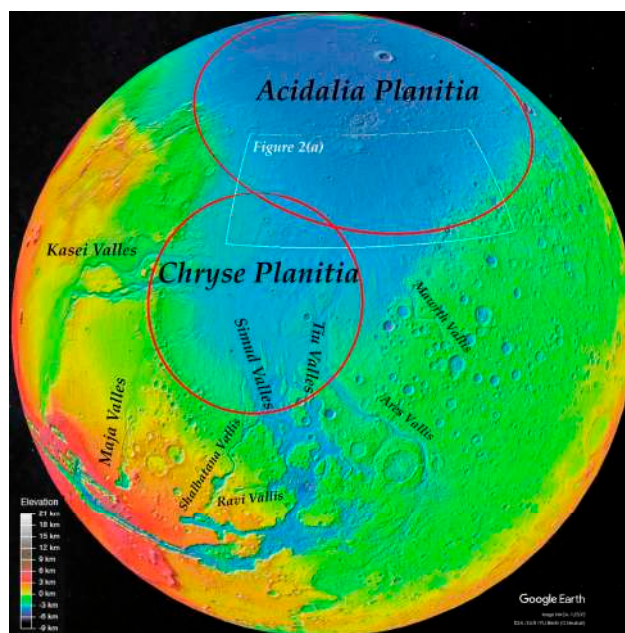


Figure 1. Mars globe overlain by Mars Orbiter Laser Altimeter (MOLA) shaded relief/colorized elevation map (Image credit: Google Earth). Red circles show the approximate outlines of quasi circular depressions (buried impact basins, Chryse and Acidalia Planitia) [18]. Note that all of the named valleys represent circum-Chryse outflow channels.

A number of small-scale (10's of meters to a few kilometers wide), near-circular to irregular-shaped mounds with summit depressions (so-called “pitted mounds” [19–22]; also referred to as pitted cones, cratered cones, pitted domes [23–28]), have been commonly observed within the northern lowlands on Mars, such as Acidalia, Chryse, Isidis, Elysium, and Utopia Planitiae (e.g., [29]). The southern part of Acidalia Planitia (Figure 2) has crater retention ages between ~3.7 and ~3.4 Gyr [30–33] and its surface is geologically interpreted as either Late Hesperian or middle Amazonian lowland units [34]. More

than 18,000 mounds (>300 m diameter) were identified, and >40,000 mounds were estimated over southern Acidalia and northern Chryse regions [21,35,36].

Since pitted mounds in eastern Acidalia Planitia-Cydonia Mensae region were first recognized from Viking Orbiter images, terrestrial analog features of various origins have been proposed to explain their occurrence in the Acidalia basin, namely (1) rootless cones (or pseudocraters) formed by the emplacement of lava flows over wet ground and the subsequent explosions [37–41], (2) pyroclastic cones or cinder cones as a result of explosive eruptions and resultant depositions of pyroclastic materials [38,39,42–46], (3) secondary impact craters with inverted relief [38], (4) pingos caused by a volume increase of ground ice doming terrain surface [3,38,47], (5) tuff rings and tuff cones resulted from phreatomagmatic explosions [25,26], (6) spring mounds originated from evaporate deposits around spring vents [25], (7) mud volcanoes defined as surface manifestation of mud from depth [21,23,25,48–50], and a combination of two or more of the processes above.

Although none of these hypotheses have been proven decisively, the mud volcano hypothesis is considered to have one of the highest astrobiological potential among the above hypotheses. This is because terrestrial mud volcanoes commonly emit not only mud and water to the surface but biotic/abiotic, gaseous hydrocarbons (mostly methane), which, if formed on ancient Mars, is of great significance for interpreting regional magmatic and hydrothermal activity, distributions of clay minerals, present-day detection of atmospheric methane, their interaction with faults and fractures, and possible microbial activity [51]. Mud volcanoes on Earth occur both onshore and offshore, mostly along subduction zones (i.e., lateral tectonic compression zones) and/or in high sedimentation rate sites [52].

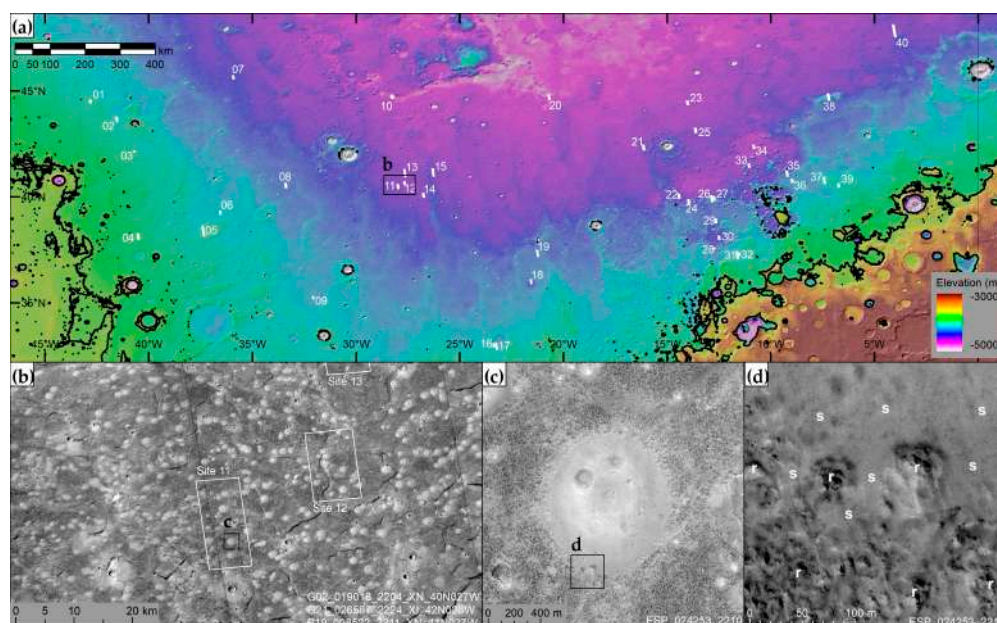


Figure 2. (a) MOLA gridded elevation overlay on MOLA hillshade background (128 pixels per degree) of northern Chryse–southern Acidalia region. The black lines are a -3760 m-contour approximating the Deuteronilus shoreline [2,11]. White-filled numbered rectangles represent the locations of digital elevation models (DEMs) generated in this study (Site 01 to 40, listed in Table 1). (b) Part of a mosaic of Mars Reconnaissance Orbiter (MRO) Context Camera (CTX) images [53], showing the central part of southern Acidalia Planitia. Pitted mounds appear as bright, circular features on the polygonally fractured terrain [17]. Sunlight illuminates the scene from the left. (c) A typical example of a pitted mound. Part of High Resolution Imaging Science Experiment (HiRISE) image ESP_024253_2210. Image credit: NASA/JPL/UA (University of Arizona). North is at the top. (d) Close-up view of the boundary between the mound and the surrounding plains in Figure 2c. Smooth mound materials (labeled as ‘s’) appear to overlie the surrounding terrain with relatively rough surfaces (labeled as ‘r’).

The previous observations in favor of the mud volcano interpretation are the results from geological data. For example, they are spatially related to other flow-related features [32,36]. They exhibit low thermal inertia relative to the surrounding plains measured from Mars Global Surveyor Thermal Emission Spectrometer (TES) [25] and Mars Odyssey Thermal Emission Imaging System (THEMIS) [54] data, which is consistent with finer-grained materials covering the mound surfaces, and the geologic setting of the Chryse-Acidalia Embayment is a depositional basin [16]. High Resolution Imaging Science Experiment (HiRISE) cameras onboard the Mars Reconnaissance Orbiter (MRO) revealed that many of the mounds in southern Acidalia have bright, smooth surface materials outwardly extending from their peripheries over the rough surrounding plains (e.g., Figure 2c,d; [21]), which suggests the expansion of mound materials occurred on the pre-existing surface. Several mounds show distinct flow features emanating from them (e.g., Supplementary Figure S8; [21]), indicating that the materials behaved as fluids during the mound formation. Other common morphologies include summit and flank pits (Figure 2c), concentric crest structures, surrounding moats, smooth surface textures, which are consistent with the mud volcanic features. However, the biggest problem is that all of the above observations do not rule out alternative interpretations (e.g., igneous volcanoes).

It should be noted that most of the mounds are located more than a few hundred meters below the Deuteronilus shoreline level (~ -3760 m; Figure 2a [2,11]). On the basis of a close spatial relationship of giant polygons and pitted mounds (Figure 2b; mounds located just inside polygonal troughs in Supplementary Figures S12 and S13) and its analogy to that of kilometer-sized polygons and terrestrial mud volcanoes in marine settings on Earth [55,56], Oehler and Allen [55] hypothesized that their co-occurrence in the Chryse-Acidalia area may have resulted from fluid expulsion processes of sediment-laden flood water. They suggested that late Hesperian deposition from outflow floods caused a rapid deposition of unconsolidated fine-grained sediments in an aqueous basin, which subsequently developed polygonal fracturing. They also characterized the geometries of submarine mounds and polygons on Earth by using high-resolution 3-D seismic data.

Those of the Martian counterparts were, however, not examined because of lacking high-resolution topographic data. The resolution of the global digital elevation models (DEMs) created based on Mars Global Surveyor (MGS) Mars Orbiter Laser Altimeter (MOLA) is 128 pixels/degree or ~ 463 m/pixel. Each spot (~ 168 m in diameter) of MOLA observation is separated about 300 m along track [57], which is insufficient to determine the shape of these mounds precisely. Thus, although geometric characterization of the Acidalia mounds are critical for quantitatively assessing how they were formed (e.g., modeling of materials for the mounds), the topographic studies of the mounds were limited to Viking image-based (low-resolution), photoclinometric measurements of about 400 mounds (>400 m wide) with unspecified locations in Acidalia and Chryse Planitiae [23,45].

In this study we extracted high-resolution DEMs from HiRISE stereo images of pitted mounds over the entire southern part of Acidalia Planitia (Figure 2a; $\sim 32^{\circ}$ – 49° N, $\sim 317^{\circ}$ – 357° E). We then analyzed the relationship between their heights (a few meters to tens of meters) and diameters (tens of meters to a few kilometers) for almost 1300 mounds (Section 3), then tested consistency with a submarine (or subaerial) mud volcano hypothesis by estimating mud reservoir depths and by making first-order estimates of the rheological parameters of fluid flows (Section 4).

Table 1. List of DEMs derived from HiRISE image pairs at each site.

Site	HiRISE Stereo Pair Image 1 ID	HiRISE Stereo Pair Image 2 ID	Center Longitude ($^{\circ}$ E) ¹	Center Latitude ($^{\circ}$ N) ¹	Resolution (m/Pixel)
01	ESP_019612_2250	ESP_025203_2250	317.1833	44.5086	1.0
02	ESP_024227_2240	ESP_024359_2240	318.4598	43.6649	1.0
03	PSP_002233_2225	PSP_002866_2225	319.2983	42.1368	1.0
04	PSP_009063_2185	PSP_009485_2185	319.4896	38.1269	1.0
05	ESP_037255_2185	ESP_037954_2185	322.6237	38.3876	2.0

Table 1. Cont.

Site	HiRISE Stereo Pair Image 1 ID	HiRISE Stereo Pair Image 2 ID	Center Longitude (°E) ¹	Center Latitude (°N) ¹	Resolution (m/Pixel)
06	PSP_002457_2195	PSP_002536_2195	323.4403	39.2529	1.0
07	ESP_024728_2260	ESP_027207_2260	324.0668	45.6430	1.0
08	ESP_014258_2210	ESP_022974_2210	326.6019	40.5313	2.0
09	ESP_034499_2155	ESP_034934_2155	327.9202	35.2393	1.0
10	ESP_018517_2250	ESP_018649_2250	331.7310	44.7243	1.0
11	ESP_024253_2210	ESP_024530_2210	332.0099	40.4877	1.0
12	ESP_018728_2210	ESP_019018_2210	332.3311	40.6531	1.0
13	ESP_027919_2215	ESP_028064_2215	332.3398	41.1169	2.0
14	ESP_017950_2205	ESP_018583_2205	333.2518	40.0696	1.0
15	ESP_026732_2215	ESP_027431_2215	333.7049	41.1558	2.0
16	ESP_021642_2135	ESP_021919_2135	336.6412	32.9827	1.0
17	ESP_026244_2130	ESP_026521_2130	336.7620	32.9493	1.0
18	ESP_025822_2165	ESP_027101_2165	338.4331	35.9987	1.0
19	ESP_034248_2175	ESP_034314_2175	338.7390	37.3332	2.0
20	ESP_028934_2250	ESP_037716_2250	339.2974	44.6937	2.0
21	PSP_009906_2225	PSP_010196_2225	343.8611	42.3290	1.0
22	PSP_007770_2205	PSP_007981_2205	345.5654	40.0352	1.0
23	ESP_017132_2250	ESP_017633_2250	345.9836	44.4325	2.0
24	PSP_005700_2200	ESP_011818_2200	346.0364	39.7757	1.0
25	ESP_018134_2235	ESP_018411_2235	346.3654	43.1340	1.0
26	ESP_032850_2200	ESP_033641_2200	347.1340	39.9110	1.0
27	PSP_009708_2205	PSP_009985_2205	347.2636	39.9283	1.0
28	PSP_002232_2180	PSP_002377_2180	347.2682	37.5626	1.0
29	ESP_019334_2190	ESP_028380_2190	347.3528	38.8651	2.0
30	ESP_016011_2185	ESP_016499_2185	347.5016	38.0586	1.0
31	ESP_026204_2175	ESP_034762_2175	348.3709	37.2445	1.0
32	ESP_034485_2175	ESP_035698_2175	348.4768	37.2845	2.0
33	ESP_027892_2220	ESP_028182_2220	348.9297	41.4773	2.0
34	ESP_028670_2225	ESP_037465_2225	349.1695	42.3576	2.0
35	PSP_009642_2215	PSP_010143_2215	350.7889	41.1003	1.0
36	PSP_008574_2210	PSP_009497_2210	351.0352	40.7468	1.0
37	ESP_025439_2210	ESP_025518_2210	352.5708	40.7737	1.0
38	ESP_016301_2250	ESP_016578_2250	352.7775	44.7067	1.0
39	ESP_023316_2210	ESP_023606_2210	353.2687	40.5359	2.0
40	ESP_025663_2280	ESP_026362_2280	355.9435	47.8408	4.0

¹ The values of center longitude and latitude of each DEM were used as the central meridian and standard parallel, respectively when DEMs are mapped to an equirectangular projection.

2. Data and Methods

We extracted forty high-resolution DEMs (1.0, 2.0, or 4.0 m/post) and corresponding orthoimages for the areas of pitted mounds in the southern part of Acidalia Planitia (e.g., Figure 3a; see also Table 1 and Supplementary Figures S1 to S40). In generating stereo image DEMs, we followed, with minor differences, the workflows of [22]. First, we performed radiometric calibration, bundle adjustment, shifting, mosaicking, and map projection of the Experimental Data Records (EDRs; ten or nine HiRISE RED-filtered raw image files) of HiRISE stereo pairs [58,59] using the US Geological Survey's Integrated Software for Imagers and Spectrometers (ISIS) 3.4.6 [60–62]. We used HiRISE image pairs that have ideal camera pointing (moderate convergence angle), good image quality (no severe atmospheric hazes or imaging errors), and 1×1 , 2×2 or 4×4 pixel binning as stereo pairs. For the application of bundle adjustment to each pair of HiRISE images, we collected hundreds of image control points between image pairs and three or more ground control points from Mars Express's High Resolution Stereo Camera (HRSC) nadir-channel images at spatial resolutions of 12.5 to 50.0 m/pixel [63]. These HRSC images are map-projected beforehand onto THEMIS geodetically controlled mosaic [64] of the southern Acidalia region using the ISIS software. All raw and calibrated image data are available in National Aeronautics and Space Administration (NASA) Planetary Data System (PDS). We then used a control network of these points to update camera pointing and spacecraft position information of each HiRISE stereo pair with the ISIS's module for bundle adjustment, jigsaw [65].

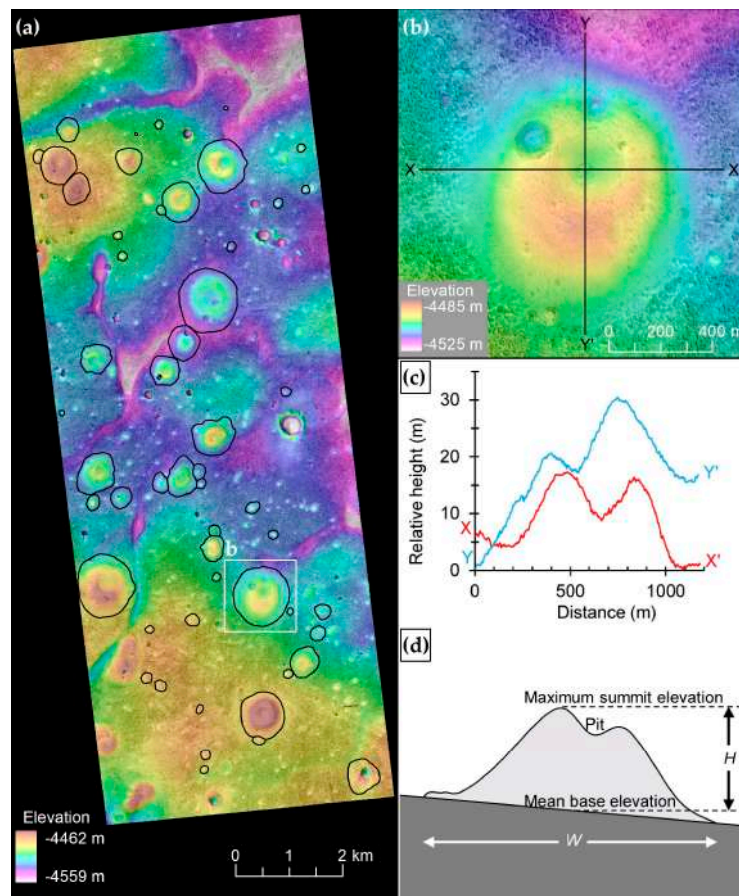


Figure 3. (a) Example of a HiRISE-derived DEM (1 m/pix) overlain on a contrast-enhanced orthoimage (1 m/pix), equivalent to Supplementary Figure S11. The solid black lines outline the periphery of each pitted mound that are manually delineated for the measurements of the basal area and average base elevation. (b) Close-up indicated in Figure 3a. This mound is equivalent to Mound 12 of Site 11. The black lines (X–X' and Y–Y') indicate the location of the topographic profile shown in Figure 2c. North is at the top. (c) Topographic profiles across a pitted mound (as shown in Figure 3b). Vertical exaggeration is about 30 times. (d) Schematic cross-section of a pitted mound and morphologic parameters measured in this study. H : maximum mound height, W : mound basal width. The vertical scale is highly exaggerated.

NASA's Ames Stereo Pipeline (ASP) 2.4.2 [66–68] software was used to perform integer image correlation (match correlation window size of 21×21 pixels), sub-pixel refinement (window size of 25×25 pixels), disparity filtering, stereo triangulation, and generation of a gridded DEM. To minimize vertical differences between DEMs and the global Mars Global Surveyor (MGS) Mars Orbiter Laser Altimeter (MOLA [57]) elevation model (128 pixels/degree or ~ 463 m/pixel), the mean value of height differences between each DEM and resampled (1, 2, or 4 m/pixels) MOLA data are subtracted from each DEM, using the Geospatial Data Abstraction Library (GDAL) 2.0.2 and Environmental Systems Research Institute (ESRI) ArcGIS Desktop ArcMap 10.2.2 software.

The resultant vertical accuracies are expected to be around several tens of centimeters for ASP-derived DEMs. This value is comparable to ASP-derived (non-bundle adjusted) DEMs and BAE Systems' SOCET SET-derived (bundle-adjusted) DEMs (so-called "HiRISE Digital Terrain Model (DTM)"; <https://www.uahirise.org/dtm/>) with vertical accuracy of ~ 20 cm [58,59] (published by the HiRISE Science Team and the USGS), root mean square errors of the discrepancies are better than

0.50 m [69,70]. On the basis of viewing geometry and ground pixel scale [71,72], we also calculated the vertical accuracy values, assuming 0.2-pixel matching error [58,59],

$$\text{Vertical Accuracy} = 0.2 * GSD / (\text{Parallax/Height}) \quad (1)$$

$$\text{Parallax/Height} = \sqrt{(PX_1 - PX_2)^2 + (PY_1 - PY_2)^2} \quad (2)$$

$$PX = -\tan(EA) \cos(SGA) \quad (3)$$

$$PY = \tan(EA) \sin(SGA), \quad (4)$$

where *GSD* is the ground sample distance which in this case is equivalent to the larger ground pixel size between the two images (mostly spatial resolution of more oblique images), the subscripts 1 and 2 refer to the two images, *PX* is a parallax in the X direction, *PY* is a parallax in the Y direction, *EA* is an emission angle, and *SGA* is a sub-spacecraft ground azimuth, which can be extracted by using the ISIS campt application. The resultant values are limited to a range of ~0.1 to 0.6 meters (Table 2).

Table 2. Expected vertical accuracy values for each DEMs.

Site	Image 1		Image 2		Parallax/Height	GSD (m/Pixel)	Vertical Accuracy (m)
	EA (°)	SGA (°)	EA (°)	SGA (°)			
01	3.55	269.47	18.68	265.90	0.28	0.32	0.23
02	25.27	80.30	2.82	271.27	0.52	0.33	0.13
03	6.26	267.21	21.23	265.80	0.28	0.32	0.23
04	7.09	266.57	19.73	265.52	0.23	0.31	0.27
05	5.67	79.01	10.51	265.81	0.28	0.60	0.42
06	30.24	80.45	2.38	73.91	0.54	0.34	0.13
07	7.86	266.68	9.62	80.11	0.31	0.31	0.20
08	7.53	79.97	28.51	80.45	0.41	0.67	0.33
09	16.34	265.43	14.11	80.94	0.54	0.31	0.11
10	2.39	74.13	27.51	266.40	0.56	0.34	0.12
11	2.59	74.54	17.39	265.70	0.36	0.31	0.18
12	2.14	273.24	18.54	80.81	0.37	0.32	0.17
13	20.08	265.81	5.15	267.90	0.28	0.63	0.46
14	5.69	267.40	21.18	265.75	0.29	0.32	0.22
15	4.80	268.29	22.78	265.90	0.34	0.32	0.19
16	0.38	332.34	25.59	265.43	0.48	0.32	0.14
17	3.58	77.33	20.16	265.33	0.43	0.31	0.15
18	5.71	267.33	18.95	81.03	0.44	0.31	0.14
19	2.82	75.36	14.32	265.63	0.30	0.61	0.40
20	7.92	79.78	16.37	265.90	0.43	0.63	0.29
21	8.49	266.32	15.96	80.71	0.43	0.31	0.14
22	7.87	80.06	6.81	266.77	0.26	0.30	0.24
23	7.31	266.79	6.18	79.33	0.24	0.61	0.51
24	0.37	1.48	26.64	265.88	0.50	0.33	0.13
25	19.47	80.65	1.81	275.29	0.38	0.32	0.17
26	7.27	266.60	23.91	80.65	0.57	0.32	0.11
27	15.37	80.82	6.92	266.73	0.40	0.31	0.16
28	6.03	267.20	7.31	80.03	0.23	0.30	0.26
29	0.37	1.10	14.40	265.70	0.26	0.31	0.24
30	28.06	80.68	2.64	75.17	0.49	0.33	0.14
31	1.78	70.93	29.39	265.87	0.59	0.34	0.11
32	2.51	272.02	22.18	80.86	0.45	0.64	0.28
33	17.06	265.77	13.76	80.65	0.55	0.62	0.22
34	6.93	266.97	4.87	78.35	0.21	0.61	0.59
35	1.40	278.59	18.18	80.76	0.35	0.32	0.18
36	4.73	78.50	14.77	265.67	0.35	0.31	0.18
37	1.88	71.29	29.91	80.29	0.54	0.34	0.13
38	4.36	268.48	22.76	266.10	0.34	0.33	0.19
39	1.80	71.28	21.25	80.78	0.36	0.64	0.36
40	4.70	78.03	20.74	266.19	0.46	0.65	0.28

We calculated both the height *H* and basal width *W* for manually delineated individual mounds (e.g., Figure 3; Supplementary Figures S1 to S40) in each DEM. To provide accurate measurements of

each pitted mound, mounds lacking a summit pit, degraded mounds, fully coalesced mounds forming complex topographies, and mounds including invalid DEM pixels have been carefully excluded from our measurements. H is defined as the difference between the maximum summit elevation and average base elevation [73,74] (Figure 3d), and W is the diameter of a circle having the same area as that of an outlined mound area [74,75].

Taking into account the vertical accuracy and post spacing for each DEM, as well as the minor uncertainties in morphometric measurements ascribed to the manual delineations of each mound (Supplementary Figures S1 to S40), maximum errors in height and width are expected to be 0.6 m and 2.0 m for DEMs at 1.0 m/pixel, 1.2 m and 4.0 m for DEMs at 2.0 m/pixel, and 2.4 m and 8.0 m for DEMs at 4.0 m/pixel. To test the validity of our measurements, we have compared H values of 21 mounds in Site 09 extracted from in our DEM (Supplementary Figure S9) with those derived using a HiRISE DTM (Supplementary Figure S41) and confirmed the discrepancies of both values in these two DEMs are within at most 0.6 m (Table 3).

Table 3. Comparisons of morphometric parameters of 21 measured mounds extracted from both our ASP-derived DEM (Figure S9) and a SOCET SET-derived DEM (Figure S41).

Mound	H (m)		Difference (m)
	Our DEM	Published DEM	
1	26.2	26.4	−0.2
2	21.6	21.9	−0.3
3	8.9	9	−0.1
4	11.8	12	−0.2
5	13.1	13.4	−0.3
6	21.1	21.2	−0.1
7	22.5	22.6	−0.1
8	20.5	20.8	−0.3
9	17.4	18	−0.6
10	12.2	12.4	−0.2
11	19.1	19.2	−0.1
12	8.1	8.2	−0.1
13	12.3	12.5	−0.2
14	17.2	17.6	−0.4
15	12.2	12.4	−0.2
16	21	21.4	−0.4
17	19.9	20.1	−0.2
18	13.5	13.9	−0.4
19	4.1	4.4	−0.3
20	10.2	10.2	0
21	14.7	14.7	0

3. Results

Morphometric measurements were performed for 1297 pitted mounds within southern Acidalia Planitia (see Figure 4 and Table S1). The basal diameters W range from 39 to 1406 m, with a mean and median of 367 and 327 m, respectively, and a standard deviation (std. dev.) of 226 m. The mound heights H are in the range of 1.1–69.5 m with a mean (median) and a std. dev. of 15.2 (12.6) ± 10.8 m. The data indicate no substantial dependence on latitude, longitude, or elevation. Previous studies, such as the photoclinometric analysis of over 400 pitted mounds within Cydonia Mensae, part of the Acidalia basin, and Chryse Planitia [23,45] and mound heights derived from three MOLA track data in Acidalia [25], are fairly comparable to our results. The exception being that a 3D photogrammetric analysis of HiRISE stereo pairs involving two pitted mounds by Oehler and Allen [21] (the same two mounds in Site 03) resulted in heights of up to 180 m, which are an order of magnitude larger than those of our results (30.8 and 31.6 m in height). This difference is hard to interpret because the past analysis was not described in detail. The ranges of H and W values and height-to-diameter ratios (H/W) of terrestrial and Martian analogous features for comparison with the mounds measured in this study are summarized in Figure 4 and Table 4.

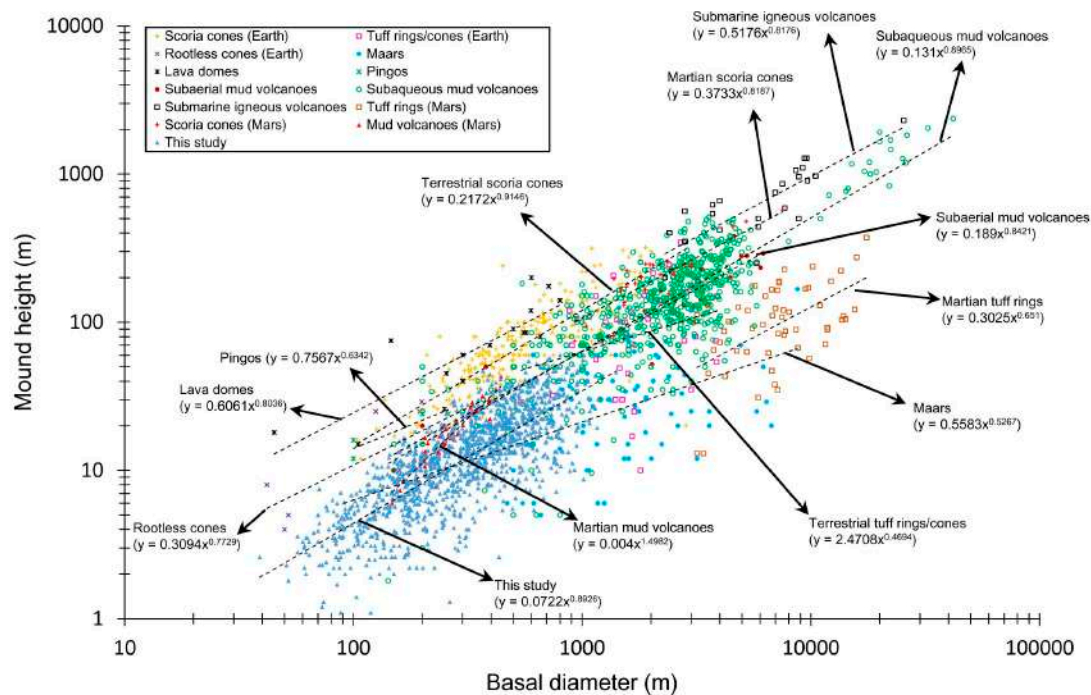


Figure 4. Log-log plot showing the measured maximum height (H) versus basal diameter (W) for 1297 pitted mounds in southern Acidalia Planitia (see also Table S1) and analogous features on Earth and Mars [22,76]. The dashed lines represent the best-fit power regression.

Table 4. A summary of morphometric parameters of the mounds shown in Figure 4.

Feature Type	N	H Range (Average)	W Range (Average)	H/W Range (Average)
Earth				
Scoria cones	241	12–320 m (85 m)	104–2843 m (640 m)	0.007–0.53 (0.137)
Tuff rings/cones	43	10–345 m (104 m)	541–3900 m (1915 m)	0.006–0.15 (0.059)
Rootless cones	10	4–29 m (17 m)	42–355 m (174 m)	0.063–0.20 (0.111)
Maars	77	4–167 m (34 m)	91–8750 m (1900 m)	0.003–0.10 (0.023)
Lava domes	16	15–200 m (83 m)	45–800 m (424 m)	0.104–0.51 (0.213)
Pingos	4	12–24 m (19 m)	100–260 m (165 m)	0.09–0.16 (0.12)
Subaerial mud volcanoes	21	10–380 m (154 m)	150–6200 m (2872 m)	0.026–0.13 (0.061)
Subaqueous mud volcanoes	619	1.8–2365 m (188 m)	142–42000 m (3026 m)	0.006–0.33 (0.067)
Submarine igneous volcanoes	24	200–2300 m (738 m)	2300–25500 m (7010 m)	0.043–0.199 (0.113)
Mars				
Scoria cones	28	75–573 m (218 m)	928–7500 m (2347 m)	0.03–0.14 (0.097)
Tuff rings/cones	52	13–372 m (117 m)	3179–17535 m (8045 m)	0.004–0.037 (0.016)
Mud volcanoes (Terra Sirenum)	50	6–43 m (17.8 m)	147–442 m (265 m)	0.034–0.10 (0.065)
This study	1297	1.1–69.5 m (15.2 m)	39–1406 m (367 m)	0.005–0.13 (0.043)

4. Discussion

4.1. Comparison of Morphometric Parameters among Possible Origins

As shown in Figure 4 and Table 4, some features on Earth and Mars show morphometric parameters similar to those of the mounds measured in this study and the others do not, which may give some clues as to what types of features are less or more likely origins of the mounds in Acidalia. Rootless cones (Earth), maars (Earth), pingos (Earth), subaerial/subaqueous mud volcanoes (Earth), and Martian mud volcanoes (Terra Sirenum) have the ranges of all three parameters relatively consistent with those of the mounds measured in this study. Regarding the ranges of the H values, submarine igneous volcanoes and Martian scoria cones are about one order of magnitude larger than the mounds measured in this study. As for the ranges of the W values, submarine igneous volcanoes, Martian scoria cones, and Martian tuff rings/cones show one or more orders of magnitude larger values than those measured in this study. With regard to the H/W ratio ranges (and average values), terrestrial lava domes show values more than two times higher than those of the other features. It should be noted that different environments (gravity, atmosphere, rock types, compositions, etc.) may have affected the mound formation processes. As suggested by Brož et al. [77], the thin atmosphere and low gravity on Mars are expected to cause far-reaching ballistic emplacement of scoria, creating wider and lower volcanic cones than those on Earth. This does not affect the interpretation that submarine igneous volcanoes, scoria cones and tuff rings/cones on Mars are less likely origins because Martian counterparts are much larger than the Acidalia mounds. However, Wilson and Head [46] proposed that the low gravity of Mars causes cooling-limited lava flows to be ~6 times longer on Earth, which decreases their H/W ratios significantly. That is why lava domes cannot be ruled out in the context of the morphometric parameters. Relative to igneous volcanism, mud volcanism is generally not such an explosive or high temperature process. Hence, the morphometric parameters of mud volcanoes on Mars are expected to be similar to those of terrestrial mud volcanoes, which are consistent with Table 4. However, another potentially serious caveat of the above discussion is that, after formation of the mounds, erosional or alteration processes could have deformed their topography to date and the observed topography can be quite different from the original one, which complicates the comparisons to newly formed analogs on Earth. If the mud volcanoes formed in a subaqueous setting (or under an ocean) 3.6 Gyr ago, several possibilities of significantly altering their topography should be considered: e.g., submarine landslide, wave erosion, outflow channel floods, periglacial deformation, wind erosion, multiple eruptions, dust cover, etc. Estimating to what extent each of these processes contribute to the deformation is hard to determine due to large uncertainties. Therefore, although the comparison of morphometric parameters provides helpful information for distinguishing the possible origins, we cannot fully rely on the results and the interpretation of this analysis.

4.2. Depths of the Sources in Subaqueous or Subaerial Conditions

Oehler and Allen [55] suggested that part of Chryse-Acialia Planitiae hosted oceans and associated marine sediments to cause fluid expulsion producing submarine mud volcanoes during late Hesperian [2,78]. However, subaerial mud volcanism has not been well discussed and ruled out. Here we will assess under which conditions (submarine, subaerial, or both) fluid expulsion caused mud eruptions by using a simple mud eruption model.

In order to operate, mud volcanism would have required subsurface mud reservoirs prior to mud eruptions, and they should have been composed of water-enriched, fine-grained sediments. On Earth, the upwelling of fluidized mud primarily requires the presence of conduits connecting the reservoirs and the surface, and a bulk density inversion between mud reservoirs and overlying materials. As for the former, on Mars, polygonal fractures (or giant polygons) underlying the mounds appear to have acted as the conduits [55,56]. If the other processes that increase the pore pressure of mud reservoirs, such as horizontal compressional forces and additional groundwater, are negligible, an isostatic compensation model to relate the height of a mud volcano (H) to the depth of a putative

mud source (D) can be developed (Figure 5). The balance between the weight of the sediment column with ambient materials (air/water) and that of the mud volcano column constrains the depth to the top of the mud source:

$$D = H(\rho_m - \rho_a) / (\rho_s - \rho_m) \quad (5)$$

where ρ_m is the bulk density of mud, ρ_s is the bulk density of the surface layers which overlies the mud sources, ρ_a is the bulk density of ambient materials during the eruption (1.0 kg/m³ for liquid water and 0.020 kg/m³ for air). This buoyancy-driven model has been applied to igneous volcanoes [79–81] and submarine mud volcanoes [82,83] on Earth for the first-order analyses. Although variations in gas and fluid content can create large density differences in the mud, we assume $\rho_m = 1400$ –2100 kg/m³ to be a plausible range of bulk mud densities because it is comparable to that measured at most submarine and subaerial mud volcanoes on Earth (the density values of 1400 kg/m³ and 2100 kg/m³ correspond to those of clast-free, mousse-like silty clays and clast-bearing mud breccia, respectively) [83–88].

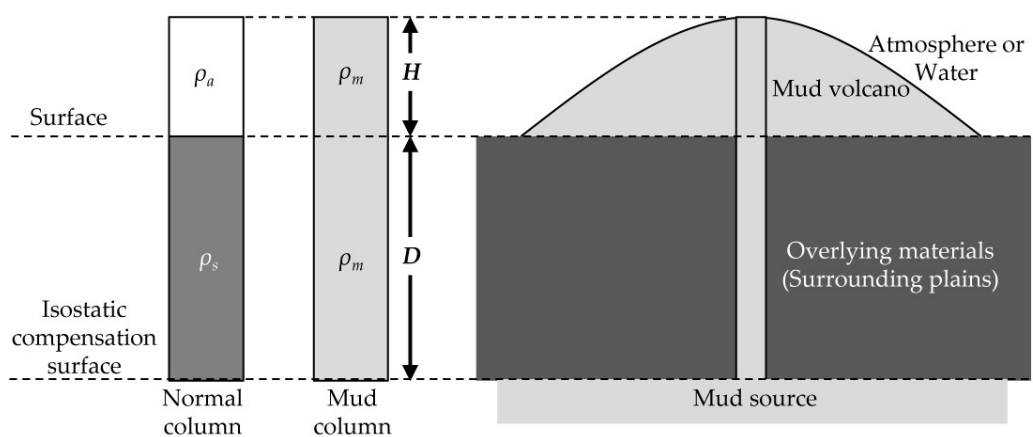


Figure 5. Schematic diagram of a simple buoyancy model of mud volcano formation [83]. D : isostatic compensation depth to the top of the mud source (i.e., thickness of overburden above mud source), ρ_m : bulk density of erupted mud through conduit, ρ_s : bulk density of overlying materials, ρ_a : bulk density of ambient materials.

The bulk density of surface materials (ρ_s) overlying mud source reservoirs within the southern Acidalia region is not readily determined because northern lowlands may consist of stratigraphic layers with different compositions (e.g., aeolian, ejecta, volcanic ash, ice-rich material), and their porosities could be a function of depth [2]. Thus, we assume that a real part of bulk dielectric permittivity (ϵ') is a function of the depth-averaged bulk density (ρ_b) of the dry geologic materials [89]:

$$\epsilon' = 1.96\rho_b \quad (6)$$

Using a value of ϵ' associated with the Vastitas Borealis interior unit [27] (~4.6 [90]), which includes the southern Acidalia region to a depth of 60–80 m [91], we can obtain $\rho_s = 2270$ kg/m³, which is also consistent with bulk densities of modeled country rock with a porosity of 25% at depths of 1 to 2 km [46]. If a subaqueous setting existed during mud eruptions, then source depths D are estimated at 0.5–32.0 m (mean = 7.0 m) to 7.1–449.7 m (mean = 98.3 m) for $\rho_m = 1400$ to 2100 kg/m³. Alternatively, considering a subaerial setting, we calculate $D = 1.8$ –111.8 m (mean = 24.4 m) to 13.6–858.5 m (mean = 187.7 m) for $\rho_m = 1400$ to 2100 kg/m³. While the thickness of the circum-Chryse outflow sediments forming the present VBF surface is uncertain, its thickness estimates range from ~100 m [9] to ~4500 m [92] (summarized in the discussion of [55]). Therefore, in either case, the estimated depths of the mud columns can be explained by fluid expulsions from the at most ~4.5 km-thick VBF sediments. Due to the above reasons, we conclude that, if the Acidalia mounds have been formed by the fluid expulsion

from the late Hesperian-aged flood deposits, either subaqueous or subaerial setting may have existed during the mud eruption.

4.3. Testing the Rheology of Fluid Flows

As previously proposed by Oehler and Allen [21], appearances of smooth surface flows at their peripheries (e.g., Supplementary Figure S8), together with upward doming topographic profiles (Figure 3c), strongly suggest (1) they were formed by emplacement of the fluids with finite yield strengths and plastic viscosities and (2) they are formed through single events (or the final shapes represent the bulk rheological properties throughout their formational events). However, the proposed mud flows creating the mounds have not been quantitatively examined in the context of rheological parameters. In this section, we test this idea by applying their morphometric parameters to fluid flow models and comparing the resultant rheological parameters with those measured at terrestrial mud volcanoes.

A slurry (a high concentration of cohesive clay particles in water) are commonly approximated as Bingham plastic fluids [93]. When a Bingham fluid slowly spreads over a plane it retains a convex-upward geometry in cross-section with its maximum height proportional to the square root of the yield strength multiplied by its basal width (i.e., a parabolic cross-section) [81,94–97]. Assuming that each singular flow of a uniform Bingham fluid formed each of the mounds, and the thickness of the center of this fluid can be approximately equal to the mound height H regardless of a summit depression, the yield strength τ_y of materials forming each mound can be described as,

$$\tau_y = (\rho g H^2) / W \quad (7)$$

where ρ is the bulk density of a fluid and g is the surface gravity on present Mars ($\sim 3.71 \text{ m/s}^2$). Here we take $\rho = 2000 \text{ kg/m}^3$, which was chosen as a typical value within the value range used in Section 4.1.

Substituting the H and W values measured from the mounds into Equation (7), we obtain that the Bingham yield strengths for the fluids were in the range of $4.8 \times 10^1 \text{ Pa}$ to $4.4 \times 10^4 \text{ Pa}$ with a mean (median) value of 5.6 (3.8) $\times 10^3 \text{ Pa}$, as listed in Supplementary Table S2. These yield strength estimates are of similar magnitude to those of samples from submarine mud volcanoes (10^3 – 10^4 Pa [83,98]) and subaerial mud volcanoes (10^1 – 10^5 Pa [87,99]). Thus, pitted mounds may be formed by a mixture of liquid water and loosely cemented, fine-grained sediments (e.g., mud slurries), which may explain the observed high albedo and low thermal inertia rather than the surrounding plains [25,54]. Cross-sectional profiles of pitted mounds in Acidalia (e.g., Figure 3c) are similar in morphology to those of typical mud volcanoes on Earth [100], which can also support the hypothesized mud flows.

If this modeling is acceptable, mud viscosity, a significant factor to constrain flow rate, can be roughly estimated. Both yield strengths (τ_y) and viscosities (η) in fine-grained slurries are known to be functions of volumetric sediment concentrations (C_v),

$$\tau_y = \alpha_1 \exp(C_v \beta_1), \quad (8)$$

$$\eta = \alpha_2 \exp(C_v \beta_2), \quad (9)$$

where α_1 , α_2 , β_1 , and β_2 are empirical constants that vary with the ratio of silt-and-clay ($< 63 \mu\text{m}$ grain size) to sand ($> 63 \mu\text{m}$ grain size) in slurries [101,102]. Inserting the expression for C_v from Equation (8) into Equation (9), we obtain an equation regarding the viscosity as:

$$\eta = \alpha_2 (\tau_y / \alpha_1)^{\beta_2 / \beta_1}. \quad (10)$$

The four empirical constants in Equation (10) were assumed to be comparable to the values of the slurries which have a silt-and-clay to sand ratio of 11:1 ($\alpha_1 = 3.79 \times 10^{-6} \text{ Pa}$, $\alpha_2 = 6.76 \times 10^{-17} \text{ Pa s}$,

$\beta_1 = 33.07$, $\beta_2 = 73.54$ [102]), because several mud samples from different terrestrial mud volcanoes are composed of silt and clay with 1–25% sand [85,87,99,103]. By substituting the results from Equation (6) into Equation (9), the resulting viscosities (η) range from 4.2×10^{-1} Pa s to 1.6×10^6 Pa s with a mean (median) value of 4.3×10^4 Pa s (6.9×10^3 Pa s) (Supplementary Table S2). These values are consistent with the mud viscosities of several mud volcano samples (0.8–1.5 Pa s [86], 100 – 10^3 Pa s [99], 10^5 Pa s [104], and 10^6 Pa s [88]), which come from different bulk densities and/or water contents at different times in different places on Earth. Perhaps a variation of the estimated η values may also represent the temporal and spatial variability of bulk physical properties of muds erupted from different reservoirs on ancient Mars.

4.4. Geological Context of the Mounds in Acidalia Basin

The morphology, topography, morphometry, and modeled rheological properties of the mounds, as stated above, are consistent with both a mud volcano and an igneous volcano origins; though, low or moderate regional gravity data of GSFC Gravity Model (GGM1025) [105,106], relative to Tharsis and Elysium regions, (see Figure 14 of [21]) strongly suggest the absence of high-density igneous bodies (i.e., magma sources) below the Acidalia surface. Moreover, according to Salvatore and Christensen [54], the analyses of THEMIS-derived thermal inertia map revealed that the materials forming the Acidalia mounds and the VBF marginal unit [27] clearly exhibit lower thermal inertia relative to the surrounding terrain (the VBF interior unit [27]), which indicates that the Acidalia mounds were composed of fine-grained sedimentary materials, produced by the expulsion of mud from the shallow subsurface. As a consequence, in the context of non-volcanic geological setting and thermophysical characteristics, we propose that a mud volcano hypothesis is favored over a magmatic hypothesis for the case of the mounds in Acidalia basin.

5. Conclusions

We created high-resolution digital elevation models, measured the accurate morphometry of nearly 1300 mounds in the Acidalia basin of Martian northern lowlands, and quantitatively assessed the possibility of subaerial/subaqueous mud volcanism by using simple mound formation models. In either case, maximum depth estimates of source reservoirs (less than ~860 or ~450 m) are consistent with mud eruptions caused by fluid expulsions of the at most ~4.5-km-thick Hesperian flood deposits (the present-day VBF surface). In a submarine setting, the Noachian-aged valley networks or the Hesperian-aged outflow channels may have provided a vast amount of water and sediments forming the northern ocean, and during this period, a rapid sedimentation could have triggered fluid expulsion processes creating mud volcanoes (e.g., scenario A of [29]). Alternatively, subsequent sublimation of the surface water could have provided ocean-free surfaces during the late Hesperian or the Amazonian period. Perhaps circum-Chryse outflow events were episodically active, which may have never produced the northern oceans. This subaerial setting may have experienced impact-induced seismic shaking and associated fluidization of subsurface reservoirs may have caused mud volcanism (e.g., scenario E of [29]).

Observational evidence, morphometric measurements, and the estimated rheological estimates of mound-forming materials altogether strongly suggest that the mounds were formed by mud volcanism, which does rule out igneous volcanism. However, on the basis of the absence of a subsurface magma source and the mounds having lower thermal inertia relative to the surrounding plains, we propose the mud volcanism is more plausible hypothesis than igneous volcanism. Similar mud volcanism may have occurred in other areas within northern lowlands, such as Utopia and Isidis basins, where both circular mounds and fractures over the Hesperian-aged VBF(-like) surfaces have been observed [32,107–109]. Unlike the potential hazards of terrestrial mud volcano fields in onshore (e.g., LUSI mud volcano, East Java, Indonesia, triggered by drilling operations [110]) and offshore settings [111], the potential oceans and associated mud volcanoes on ancient Mars may have provided the inventory of a significant amount of liquid water and dissolved gasses, which is also the case for submarine igneous volcanism

(e.g., a seamount of Izu–Bonin Arc [112]). In a submarine setting, ocean(s) may have provided more habitable environments for a relatively long period of time than those in a subaerial setting because a large standing body of water possibly protects life against various threats, such as cosmic ray irradiation [113] and UV radiation [114]. Because terrestrial mud volcanic provinces generally provide favorable environments of methane emission and microbial life [115], sediments beneath mud volcano features on Mars may preserve extant aquifers and/or gas hydrate systems, and perhaps traces of past life, which can be one of the most suitable sites for future Mars landing missions.

Supplementary Materials: The following are available online at <http://www.mdpi.com/2076-3263/8/5/152/s1>, Figures S1–S40: Color-coded, high-resolution DEM draped over a contrast-enhanced grayscale orthoimage for Site 01 to Site 40, Figure S41: a published HiRISE DTM used for the comparison of morphometric parameters of mounds, Table S1: Morphometric parameters of the 1297 pitted mounds at 40 study sites, Table S2: Estimated yield strengths and reservoir depths for all the mounds.

Author Contributions: R.H. and H.M. conceived and designed research; R.H. analyzed data; R.H. and H.M. wrote the paper.

Acknowledgments: This work was supported by JSPS KAKENHI Grant Numbers JP16K13890 and JP17H02953. We appreciate the TOKYO DOME CORPORATION for their great support of the Space Museum TeNQ and the branch of Space Exploration Education and Discovery (SEED), the University Museum, the University of Tokyo. We thank HiRISE science team for producing publicly available, high-resolution image datasets. We also appreciate the developers of USGS Integrated Software for Imagers and Spectrometers for enabling us to handle Mars image datasets. We are grateful to NASA Ames Stereo Pipeline developers for creating open source software used to generate DEMs. Elpitha Howington-Kraus was very helpful answering questions about generation of SOCET SET-derived DEMs and theoretical estimates of vertical accuracy of DEMs. We acknowledge Zachary Morrato, Ross Beyer, Oleg Alexandrov, and Trent Hare for their helpful comments on the extraction of DEMs and relevant GIS processing and Reid Parsons for helpful corrections. The authors also would like to thank three anonymous reviewers for greatly improving the manuscript.

Conflicts of Interest: The authors declare no conflict of interest.

References

1. Baker, V.R.; Strom, R.G.; Gulick, V.C.; Kargel, J.S.; Komatsu, G.; Kale, V.S. Ancient oceans, ice sheets and the hydrological cycle on mars. *Nature* **1991**, *352*, 589. [CrossRef]
2. Clifford, S.M.; Parker, T.J. The evolution of the martian hydrosphere: Implications for the fate of a primordial ocean and the current state of the northern plains. *Icarus* **2001**, *154*, 40–79. [CrossRef]
3. Parker, T.J.; Gorsline, D.S.; Saunders, R.S.; Pieri, D.C.; Schneeberger, D.M. Coastal geomorphology of the martian northern plains. *J. Geophys. Res. Planets* **1993**, *98*, 11061–11078. [CrossRef]
4. Parker, T.J.; Stephen Saunders, R.; Schneeberger, D.M. Transitional morphology in west deuterionilus mensae, mars: Implications for modification of the lowland/upland boundary. *Icarus* **1989**, *82*, 111–145. [CrossRef]
5. Baker, V.R.; Milton, D.J. Erosion by catastrophic floods on mars and earth. *Icarus* **1974**, *23*, 27–41. [CrossRef]
6. Carr, M.H. *The Surface of Mars*; Cambridge University Press: Cambridge, UK, 2007.
7. Scott, D.H.; Tanaka, K.L. *Geologic Map of the Western Equatorial Region of Mars*; USGS: Reston, VA, USA, 1986.
8. Tanaka, K.L.; Scott, D.H. *Geologic Map of the Polar Regions of Mars*; USGS: Reston, VA, USA, 1987.
9. Kreslavsky, M.A.; Head, J.W. Fate of outflow channel effluents in the northern lowlands of mars: The vastitas borealis formation as a sublimation residue from frozen ponded bodies of water. *J. Geophys. Res. Planets* **2002**, *107*, 4-1–4-25. [CrossRef]
10. Head, J.W.; Kreslavsky, M.A.; Pratt, S. Northern lowlands of mars: Evidence for widespread volcanic flooding and tectonic deformation in the hesperian period. *J. Geophys. Res. Planets* **2002**, *107*, 3-1–3-29. [CrossRef]
11. Head, J.W.; Hiesinger, H.; Ivanov, M.A.; Kreslavsky, M.A.; Pratt, S.; Thomson, B.J. Possible ancient oceans on mars: Evidence from mars orbiter laser altimeter data. *Science* **1999**, *286*, 2134–2137. [CrossRef] [PubMed]
12. Ivanov, M.A.; Erkeling, G.; Hiesinger, H.; Bernhardt, H.; Reiss, D. Topography of the deuterionilus contact on mars: Evidence for an ancient water/mud ocean and long-wavelength topographic readjustments. *Planet. Space Sci.* **2017**, *144*, 49–70. [CrossRef]
13. Citron, R.I.; Manga, M.; Hemingway, D.J. Timing of oceans on mars from shoreline deformation. *Nature* **2018**, *555*, 643–646. [CrossRef] [PubMed]
14. Carr, M.H. *Water on Mars*; Oxford University Press: New York, NY, USA, 1996.

15. Turbet, M.; Forget, F.; Head, J.W.; Wordsworth, R. 3D modelling of the climatic impact of outflow channel formation events on early mars. *Icarus* **2017**, *288*, 10–36. [[CrossRef](#)]
16. Oehler, D.Z.; Allen, C.C. Focusing the search for biosignatures on mars: Facies prediction with an example from acidalia planitia. In *Sedimentary Geology of Mars*; Grotzinger, J.P., Milliken, R.E., Eds.; SEPM (Society for Sedimentary Geology): Tulsa, OK, USA, 2012.
17. Lucchitta, B.K.; Ferguson, H.M.; Summers, C. Sedimentary deposits in the northern lowland plains, mars. *J. Geophys. Res. Solid Earth* **1986**, *91*, E166–E174. [[CrossRef](#)]
18. Frey, H. Ages of very large impact basins on mars: Implications for the late heavy bombardment in the inner solar system. *Geophys. Res. Lett.* **2008**, *35*, L13203. [[CrossRef](#)]
19. Martínez-Alonso, S.; Mellon, M.T.; Banks, M.E.; Keszthelyi, L.P.; McEwen, A.S.; Team, T.H. Evidence of volcanic and glacial activity in chryse and acidalia planitiae, mars. *Icarus* **2011**, *212*, 597–621. [[CrossRef](#)]
20. Ramsdale, J.D.; Balme, M.R.; Conway, S.J.; Gallagher, C.; van Gasselt, S.A.; Hauber, E.; Orgel, C.; Séjourné, A.; Skinner, J.A.; Costard, F.; et al. Grid-based mapping: A method for rapidly determining the spatial distributions of small features over very large areas. *Planet. Space Sci.* **2017**, *140*, 49–61. [[CrossRef](#)]
21. Oehler, D.Z.; Allen, C.C. Evidence for pervasive mud volcanism in acidalia planitia, mars. *Icarus* **2010**, *208*, 636–657. [[CrossRef](#)]
22. Hemmi, R.; Miyamoto, H. Distribution, morphology, and morphometry of circular mounds in the elongated basin of northern terra sirenum, mars. *Prog. Earth Planet. Sci.* **2017**, *4*, 26. [[CrossRef](#)]
23. Tanaka, K.L. Sedimentary history and mass flow structures of chryse and acidalia planitiae, mars. *J. Geophys. Res. Planets* **1997**, *102*, 4131–4149. [[CrossRef](#)]
24. Carr, M.H.; Head, J.W. Oceans on mars: An assessment of the observational evidence and possible fate. *J. Geophys. Res. Planets* **2003**, *108*. [[CrossRef](#)]
25. Farrand, W.H.; Gaddis, L.R.; Keszthelyi, L. Pitted cones and domes on mars: Observations in acidalia planitia and cydonia mensae using moc, themis, and tes data. *J. Geophys. Res. Planets* **2005**, *110*, E05005. [[CrossRef](#)]
26. McGill, G.E. *Geologic Map of Cydonia Mensae—Southern Acidalia Planitia, Mars, Quadrangles MTM 40007, 40012, 40017, 45007, 45012, and 45017*; U.S. Geological Survey Geologic Investigations Series I-2811; USGS: Reston, VA, USA, 2005.
27. Tanaka, K.L.; Skinner, J.A.; Hare, T.M. Geologic map of the northern plains of mars. In *U.S. Geological Survey Scientific Investigations Map 2888*; USGS: Reston, VA, USA, 2005.
28. Dundas, C.M.; Keszthelyi, L.P.; McEwen, A.S.; Team, H. Initial hirise observations of cratered cone groups on mars. In Proceedings of the 38th Lunar and Planetary Science Conference, League City, TX, USA, 12–16 March 2007; p. 2116.
29. Skinner, J.A.; Mazzini, A. Martian mud volcanism: Terrestrial analogs and implications for formational scenarios. *Mar. Pet. Geol.* **2009**, *26*, 1866–1878. [[CrossRef](#)]
30. Werner, S.C.; Tanaka, K.L.; Skinner, J.A. Mars: The evolutionary history of the northern lowlands based on crater counting and geologic mapping. *Planet. Space Sci.* **2011**, *59*, 1143–1165. [[CrossRef](#)]
31. Platz, T.; Michael, G.; Tanaka, K.L.; Skinner, J.A.; Fortezzo, C.M. Crater-based dating of geological units on mars: Methods and application for the new global geological map. *Icarus* **2013**, *225*, 806–827. [[CrossRef](#)]
32. Ivanov, M.A.; Hiesinger, H.; Erkeling, G.; Reiss, D. Evidence for large reservoirs of water/mud in utopia and acidalia planitiae on mars. *Icarus* **2015**, *248*, 383–391. [[CrossRef](#)]
33. Warner, N.H.; Gupta, S.; Calef, F.; Grindrod, P.; Boll, N.; Goddard, K. Minimum effective area for high resolution crater counting of martian terrains. *Icarus* **2015**, *245*, 198–240. [[CrossRef](#)]
34. Tanaka, K.L.; Skinner, J.A.J.; Dohm, J.M.; Irwin Iii, R.P.; Kolb, E.J.; Fortezzo, C.M.; Platz, T.; Michael, G.G.; Hare, T. Geologic map of mars, scale 1:20,000,000. In *U.S. Geological Survey Scientific Investigations Map 3292*; USGS: Reston, VA, USA, 2014.
35. Amador, E.S.; Allen, C.C.; Oehler, D.Z. Regional mapping and spectral analysis of mounds in acidalia planitia, mars. In Proceedings of the 41st Lunar and Planetary Science Conference, The Woodlands, TX, USA, 1–5 March 2010; p. 1037.
36. Skinner, J.A. Constraining the origin of pitted cones in chryse and acidalia planitiae, mars, based on their statistical distributions and marginal relationships. In Proceedings of the 43rd Lunar and Planetary Science Conference, The Woodlands, TX, USA, 19–23 March 2012; p. 2905.
37. Frey, H.; Lowry, B.L.; Chase, S.A. Pseudocraters on mars. *J. Geophys. Res. Solid Earth* **1979**, *84*, 8075–8086. [[CrossRef](#)]

38. Lucchitta, B.K. Mars and earth: Comparison of cold-climate features. *Icarus* **1981**, *45*, 264–303. [[CrossRef](#)]
39. Frey, H.; Jarosewich, M. Subkilometer martian volcanoes: Properties and possible terrestrial analogs. *J. Geophys. Res. Solid Earth* **1982**, *87*, 9867–9879. [[CrossRef](#)]
40. Carr, M.H. Mars: A water-rich planet? *Icarus* **1986**, *68*, 187–216. [[CrossRef](#)]
41. Fagents, S.A.; Lanagan, P.; Greeley, R. Rootless cones on mars: A consequence of lava-ground ice interaction. *Geol. Soc. Lond. Spec. Publ.* **2002**, *202*, 295–317. [[CrossRef](#)]
42. Ann Hodges, C.; Moore, H.J. The subglacial birth of olympus mons and its aureoles. *J. Geophys. Res. Solid Earth* **1979**, *84*, 8061–8074. [[CrossRef](#)]
43. Wood, C.A. Monogenetic volcanoes of the terrestrial planets. In Proceedings of the 10th Lunar and Planetary Science Conference, Houston, TX, USA, 19–23 March 1979; pp. 2815–2840.
44. Greeley, R.; Spudis, P.D. Volcanism on mars. *Rev. Geophys.* **1981**, *19*, 13–41. [[CrossRef](#)]
45. Davis, P.A.; Tanaka, K.L. Morphometries and possible terrestrial analogs of small martian volcanoes. In Proceedings of the 25th Lunar and Planetary Science Conference, Houston, TX, USA, 14–18 March 1994; p. 317.
46. Wilson, L.; Head, J.W. Mars: Review and analysis of volcanic eruption theory and relationships to observed landforms. *Rev. Geophys.* **1994**, *32*, 221–263. [[CrossRef](#)]
47. Rossbacher, L.A.; Judson, S. Ground ice on mars: Inventory, distribution, and resulting landforms. *Icarus* **1981**, *45*, 39–59. [[CrossRef](#)]
48. Komar, P.D. Mud volcanoes on mars. In *Reports of Planetary Geology and Geophysics Program, 1990*; NASA: Washington, DC, USA, 1991; pp. 539–541.
49. Keszthelyi, L.P.; Jaeger, W.L.; Dundas, C.M.; Martínez-Alonso, S.; McEwen, A.S.; Milazzo, M.P. Hydrovolcanic features on mars: Preliminary observations from the first mars year of hirise imaging. *Icarus* **2010**, *205*, 211–229. [[CrossRef](#)]
50. McGowan, E. Spatial distribution of putative water related features in southern acidalia/cydonia mensae, mars. *Icarus* **2009**, *202*, 78–89. [[CrossRef](#)]
51. Oehler, D.Z.; Etiopie, G. Methane seepage on mars: Where to look and why. *Astrobiology* **2017**, *17*, 1233–1264. [[CrossRef](#)] [[PubMed](#)]
52. Milkov, A.V. Worldwide distribution of submarine mud volcanoes and associated gas hydrates. *Mar. Geol.* **2000**, *167*, 29–42. [[CrossRef](#)]
53. Malin, M.C.; Bell, J.F.; Cantor, B.A.; Caplinger, M.A.; Calvin, W.M.; Clancy, R.T.; Edgett, K.S.; Edwards, L.; Haberle, R.M.; James, P.B.; et al. Context camera investigation on board the mars reconnaissance orbiter. *J. Geophys. Res. Planets* **2007**, *112*, E05S04. [[CrossRef](#)]
54. Salvatore, M.R.; Christensen, P.R. On the origin of the vastitas borealis formation in chryse and acidalia planitiae, mars. *J. Geophys. Res. Planets* **2014**, *119*, 2437–2456. [[CrossRef](#)]
55. Oehler, D.Z.; Allen, C.C. Giant polygons and mounds in the lowlands of mars: Signatures of an ancient ocean? *Astrobiology* **2012**, *12*, 601–615. [[CrossRef](#)] [[PubMed](#)]
56. Allen, C.C.; Oehler, D.Z.; Etiopie, G.; Van Rensbergen, P.; Baci, C.; Feyzullayev, A.; Martinelli, G.; Tanaka, K.; Van Rooij, D. Fluid expulsion in terrestrial sedimentary basins: A process providing potential analogs for giant polygons and mounds in the martian lowlands. *Icarus* **2013**, *224*, 424–432. [[CrossRef](#)]
57. Smith, D.E.; Zuber, M.T.; Frey, H.V.; Garvin, J.B.; Head, J.W.; Muhleman, D.O.; Pettengill, G.H.; Phillips, R.J.; Solomon, S.C.; Zwally, H.J. Mars orbiter laser altimeter: Experiment summary after the first year of global mapping of mars. *J. Geophys. Res. Planets* **2001**, *106*, 23689–23722. [[CrossRef](#)]
58. McEwen, A.S.; Eliason, E.M.; Bergstrom, J.W.; Bridges, N.T.; Hansen, C.J.; Delamere, W.A.; Grant, J.A.; Gulick, V.C.; Herkenhoff, K.E.; Keszthelyi, L.; et al. Mars reconnaissance orbiter's high resolution imaging science experiment (hirise). *J. Geophys. Res. Planets* **2007**, *112*, E05S02. [[CrossRef](#)]

59. Kirk, R.L.; Howington-Kraus, E.; Rosiek, M.R.; Anderson, J.A.; Archinal, B.A.; Becker, K.J.; Cook, D.A.; Galuszka, D.M.; Geissler, P.E.; Hare, T.M.; et al. Ultrahigh resolution topographic mapping of mars with mro hirise stereo images: Meter-scale slopes of candidate phoenix landing sites. *J. Geophys. Res. Planets* **2008**, *113*, E00A24. [[CrossRef](#)]
60. Gaddis, L.; Anderson, J.; Becker, K.; Becker, T.; Cook, D.; Edwards, K.; Eliason, E.; Hare, T.; Kieffer, H.; Lee, E.M. An overview of the integrated software for imaging spectrometers (ISIS). In Proceedings of the 28th Lunar and Planetary Science Conference, Houston, TX, USA, 17–21 March 1997; p. 1226.
61. Torson, J.M.; Becker, K.J. ISIS—A software architecture for processing planetary images. In Proceedings of the 28th Lunar and Planetary Science Conference, Houston, TX, USA, 17–21 March 1997; p. 1219.
62. Anderson, J.A.; Sides, S.C.; Soltesz, D.L.; Sucharski, T.L.; Becker, K.J. Modernization of the integrated software for imagers and spectrometers. In Proceedings of the 35th Lunar and Planetary Science Conference, League City, TX, USA, 15–19 March 2004; p. 2039.
63. Neukum, G.; Jaumann, R. Hrsc: The high resolution stereo camera of mars express. In *Mars Express: The Scientific Payload*; ESA: Noordwijk, The Netherlands, 2004; Volume SP-1240, pp. 17–35.
64. Ferguson, R.L.; Lee, E.M.; Weller, L. Themis geodetically controlled mosaics of mars. In Proceedings of the 44th Lunar and Planetary Science Conference, The Woodlands, TX, USA, 18–22 March 2013; p. 1642.
65. Edmundson, K.L.; Cook, D.A.; Thomas, O.H.; Archinal, B.A.; Kirk, R.L. Jigsaw: The ISIS3 bundle adjustment for extraterrestrial photogrammetry. *ISPRS Ann. Photogramm. Remote Sens. Spat. Inf. Sci.* **2012**, *1-4*, 203–208. [[CrossRef](#)]
66. Broxton, M.J.; Edwards, L.J. The ames stereo pipeline: Automated 3d surface reconstruction from orbital imagery. In Proceedings of the 39th Lunar and Planetary Science Conference, League City, TX, USA, 10–14 March 2008; p. 2419.
67. Moratto, Z.M.; Broxton, M.J.; Beyer, R.A.; Lundy, M.; Husmann, K. Ames stereo pipeline, nasa's open source automated stereogrammetry software. In Proceedings of the 41st Lunar and Planetary Science Conference, The Woodlands, TX, USA, 1–5 March 2010; p. 2364.
68. Shean, D.E.; Alexandrov, O.; Moratto, Z.M.; Smith, B.E.; Joughin, I.R.; Porter, C.; Morin, P. An automated, open-source pipeline for mass production of digital elevation models (dems) from very-high-resolution commercial stereo satellite imagery. *ISPRS J. Photogramm. Remote Sens.* **2016**, *116*, 101–117. [[CrossRef](#)]
69. Re, C.; Roncella, R.; Forlani, G.; Cremonese, G.; Naletto, G. Evaluation of area-based image matching applied to dtm generation with hirise images. *ISPRS Ann. Photogramm. Remote Sens. Spat. Inf. Sci.* **2012**, *1-4*, 209–214. [[CrossRef](#)]
70. Watters, W.A.; Geiger, L.M.; Fendrock, M.; Gibson, R. Morphometry of small recent impact craters on mars: Size and terrain dependence, short-term modification. *J. Geophys. Res. Planets* **2015**, *120*, 226–254. [[CrossRef](#)]
71. Becker, K.J.; Archinal, B.A.; Hare, T.H.; Kirk, R.L.; Howington-Kraus, E.; Robinson, M.S.; Rosiek, M.R. Criteria for automated identification of stereo image pairs. In Proceedings of the 46th Lunar and Planetary Science Conference, The Woodlands, TX, USA, 16–20 March 2015; Volume 46, p. 2703.
72. Beddingfield, C.B.; Burr, D.M.; Emery, J.P. Fault geometries on uranus' satellite miranda: Implications for internal structure and heat flow. *Icarus* **2015**, *247*, 35–52. [[CrossRef](#)]
73. Settle, M. The structure and emplacement of cinder cone fields. *Am. J. Sci.* **1979**, *279*, 1089–1107. [[CrossRef](#)]
74. Kervyn, M.; Ernst, G.G.J.; Carracedo, J.C.; Jacobs, P. Geomorphometric variability of “monogenetic” volcanic cones: Evidence from mauna kea, lanzarote and experimental cones. *Geomorphology* **2012**, *136*, 59–75. [[CrossRef](#)]
75. Favalli, M.; Karátson, D.; Mazzarini, F.; Pareschi, M.T.; Boschi, E. Morphometry of scoria cones located on a volcano flank: A case study from mt. Etna (Italy), based on high-resolution lidar data. *J. Volcanol. Geotherm. Res.* **2009**, *186*, 320–330. [[CrossRef](#)]
76. Batiza, R.; Vanko, D. Volcanic development of small oceanic central volcanoes on the flanks of the east pacific rise inferred from narrow-beam echo-sounder surveys. *Mar. Geol.* **1983**, *54*, 53–90. [[CrossRef](#)]
77. Brož, P.; Čadež, O.; Hauber, E.; Rossi, A.P. Scoria cones on mars: Detailed investigation of morphometry based on high-resolution digital elevation models. *J. Geophys. Res. Planets* **2015**, *120*, 1512–1527. [[CrossRef](#)]
78. Jakosky, B.M.; Phillips, R.J. Mars' volatile and climate history. *Nature* **2001**, *412*, 237–244. [[CrossRef](#)] [[PubMed](#)]
79. Vogt, P.R. Volcano height and plate thickness. *Earth Planet. Sci. Lett.* **1974**, *23*, 337–348. [[CrossRef](#)]
80. Smith, D.K.; Cann, J.R. Building the crust at the mid-Atlantic ridge. *Nature* **1993**, *365*, 707–715. [[CrossRef](#)]
81. Melosh, H.J. *Planetary Surface Processes*; Cambridge University Press: Cambridge, UK, 2011.

82. Henry, P.; Le Pichon, X.; Lallemand, S.; Foucher, J.-P.; Westbrook, G.; Hobart, M. Mud volcano field seaward of the barbados accretionary complex: A deep-towed side scan sonar survey. *J. Geophys. Res. Solid Earth* **1990**, *95*, 8917–8929. [[CrossRef](#)]
83. Murton, B.J.; Biggs, J. Numerical modelling of mud volcanoes and their flows using constraints from the gulf of Cadiz. *Mar. Geol.* **2003**, *195*, 223–236. [[CrossRef](#)]
84. Volgin, A.V.; Woodside, J.M. Sidescan sonar images of mud volcanoes from the mediterranean ridge: Possible causes of variations in backscatter intensity. *Mar. Geol.* **1996**, *132*, 39–53. [[CrossRef](#)]
85. Lance, S.; Henry, P.; Le Pichon, X.; Lallemand, S.; Chamley, H.; Rostek, F.; Faugères, J.-C.; Gonthier, E.; Olu, K. Submersible study of mud volcanoes seaward of the barbados accretionary wedge: Sedimentology, structure and rheology. *Mar. Geol.* **1998**, *145*, 255–292. [[CrossRef](#)]
86. Rifai, R. *Spatial Modelling and Risk Assessment of Sidoarjo Mud Volcanic Flow*; Gadjah Mada University: Yogyakarta, Indonesia, 2008.
87. Kopf, A.; Stegmann, S.; Delisle, G.; Panahi, B.; Aliyev, C.S.; Guliyev, I. In situ cone penetration tests at the active dashgil mud volcano, Azerbaijan: Evidence for excess fluid pressure, updoming, and possible future violent eruption. *Mar. Pet. Geol.* **2009**, *26*, 1716–1723. [[CrossRef](#)]
88. Kopf, A.; Behrmann, J.H. Extrusion dynamics of mud volcanoes on the mediterranean ridge accretionary complex. *Geol. Soc. Lond. Spec. Publ.* **1999**, *174*, 169. [[CrossRef](#)]
89. Ulaby, F.T.; Bengal, T.; East, J.; Dobson, M.C.; Garvin, J.; Evans, D. *Microwave Dielectric Spectrum of Rocks*; 23817-1-T; University of Michigan: Ann Arbor, MI, USA, 1988.
90. Mouginot, J.; Pommerol, A.; Beck, P.; Kofman, W.; Clifford, S.M. Dielectric map of the Martian northern hemisphere and the nature of plain filling materials. *Geophys. Res. Lett.* **2012**, *39*. [[CrossRef](#)]
91. Mouginot, J.; Pommerol, A.; Kofman, W.; Beck, P.; Schmitt, B.; Herique, A.; Grima, C.; Safaeinili, A.; Plaut, J.J. The 3–5 MHz global reflectivity map of mars by marsis/mars express: Implications for the current inventory of subsurface H₂O. *Icarus* **2010**, *210*, 612–625. [[CrossRef](#)]
92. Zuber, M.T.; Solomon, S.C.; Phillips, R.J.; Smith, D.E.; Tyler, G.L.; Aharonson, O.; Balmino, G.; Banerdt, W.B.; Head, J.W.; Johnson, C.L.; et al. Internal structure and early thermal evolution of mars from mars global surveyor topography and gravity. *Science* **2000**, *287*, 1788. [[CrossRef](#)] [[PubMed](#)]
93. Liu, K.F.; Mei, C.C. Slow spreading of a sheet of bingham fluid on an inclined plane. *J. Fluid Mech.* **1989**, *207*, 505–529. [[CrossRef](#)]
94. Nye, J.F. The mechanics of glacier flow. *J. Glaciol.* **1952**, *2*, 82–93. [[CrossRef](#)]
95. Hulme, G. The interpretation of lava flow morphology. *Geophys. J. R. Astron. Soc.* **1974**, *39*, 361–383. [[CrossRef](#)]
96. Coussot, P.; Piau, J.M. On the behavior of fine mud suspensions. *Rheol. Acta* **1994**, *33*, 175–184. [[CrossRef](#)]
97. Blake, S. Viscoplastic models of lava domes. In *Lava Flows and Domes: Emplacement Mechanisms and Hazard Implications*; Fink, J.H., Ed.; Springer: Berlin/Heidelberg, Germany, 1990; pp. 88–126.
98. Phipps, S.P. Rheology of serpentinite muds in the mariana-izu-bonin forearc. *Proc. Ocean Drill. Program Sci. Results* **1992**, *125*, 363–372. [[CrossRef](#)]
99. Rudolph, M.L.; Manga, M. Mud volcano response to the 4 April 2010 el mayor-cucapah earthquake. *J. Geophys. Res. Solid Earth* **2010**, *115*, B12211. [[CrossRef](#)]
100. Yusifov, M.; Rabinowitz, P.D. Classification of mud volcanoes in the south caspian basin, offshore Azerbaijan. *Mar. Pet. Geol.* **2004**, *21*, 965–975. [[CrossRef](#)]
101. O'Brien, J.S.; Julien, P.Y. Laboratory analysis of mudflow properties. *J. Hydraul. Eng.* **1988**, *114*, 877–887. [[CrossRef](#)]
102. Major, J.J.; Pierson, T.C. Debris flow rheology: Experimental analysis of fine-grained slurries. *Water Resour. Res.* **1992**, *28*, 841–857. [[CrossRef](#)]
103. Kopf, A.J. Significance of mud volcanism. *Rev. Geophys.* **2002**, *40*, 2-1–2-52. [[CrossRef](#)]
104. Rudolph, M.L.; Karlstrom, L.; Manga, M. A prediction of the longevity of the lusi mud eruption, Indonesia. *Earth Planet. Sci. Lett.* **2011**, *308*, 124–130. [[CrossRef](#)]
105. Smith, D.E.; Lerch, F.J.; Nerem, R.S.; Zuber, M.T.; Patel, G.B.; Fricke, S.K.; Lemoine, F.G. An improved gravity model for mars: Goddard mars model 1. *J. Geophys. Res. Planets* **2012**, *98*, 20871–20889. [[CrossRef](#)]
106. Konopliv, A.S.; Yoder, C.F.; Standish, E.M.; Yuan, D.-N.; Sjogren, W.L. A global solution for the mars static and seasonal gravity, mars orientation, phobos and deimos masses, and mars ephemeris. *Icarus* **2006**, *182*, 23–50. [[CrossRef](#)]

107. Ivanov, M.A.; Hiesinger, H.; Erkeling, G.; Hielscher, F.J.; Reiss, D. Major episodes of geologic history of isidis planitia on mars. *Icarus* **2012**, *218*, 24–46. [[CrossRef](#)]
108. Ghent, R.R.; Anderson, S.W.; Pithawala, T.M. The formation of small cones in isidis planitia, mars through mobilization of pyroclastic surge deposits. *Icarus* **2012**, *217*, 169–183. [[CrossRef](#)]
109. McGowan, E.M. The utopia/isidis overlap: Possible conduit for mud volcanism on mars. *Icarus* **2011**, *212*, 622–628. [[CrossRef](#)]
110. Davies, R.J.; Brumm, M.; Manga, M.; Rubiandini, R.; Swarbrick, R.; Tingay, M. The east java mud volcano (2006 to present): An earthquake or drilling trigger? *Earth Planet. Sci. Lett.* **2008**, *272*, 627–638. [[CrossRef](#)]
111. Pelletier, B.R. Review of surficial geology and engineering hazards in the Canadian offshore. *Atl. Geol.* **1979**, *15*, 55–91. [[CrossRef](#)]
112. Tsunogai, U.; Ishibashi, J.; Wakita, H.; Gamo, T.; Watanabe, K.; Kajimura, T.; Kanayama, S.; Sakai, H. Peculiar features of suiyo seamount hydrothermal fluids, izu-bonin arc: Differences from subaerial volcanism. *Earth Planet. Sci. Lett.* **1994**, *126*, 289–301. [[CrossRef](#)]
113. Pavlov, A.A.; Vasilyev, G.; Ostryakov, V.M.; Pavlov, A.K.; Mahaffy, P. Degradation of the organic molecules in the shallow subsurface of mars due to irradiation by cosmic rays. *Geophys. Res. Lett.* **2012**, *39*, L13202. [[CrossRef](#)]
114. Cleaves, H.J.; Miller, S.L. Oceanic protection of prebiotic organic compounds from UV radiation. *Proc. Natl. Acad. Sci. USA* **1998**, *95*, 7260–7263. [[CrossRef](#)] [[PubMed](#)]
115. Etiope, G.; Oehler, D.Z.; Allen, C.C. Methane emissions from earth's degassing: Implications for mars. *Planet. Space Sci.* **2011**, *59*, 182–195. [[CrossRef](#)]



© 2018 by the authors. Licensee MDPI, Basel, Switzerland. This article is an open access article distributed under the terms and conditions of the Creative Commons Attribution (CC BY) license (<http://creativecommons.org/licenses/by/4.0/>).

Chapter 5

Morphology and Morphometry of Sub-kilometer Craters on the Nearside of Phobos and Implications for Regolith Properties

The content of this chapter was peer-reviewed and published as a research article in *Transactions of the Japan Society for Aeronautical and Space Sciences* by the Japan Society for Aeronautical and Space Sciences (JSASS) in 2020, and its copyright is held by JSASS. JSASS allows the use of the paper in the author's dissertation, and its published version can be deposited in the author's institutional repository.

Article information:

Hemmi, R., Miyamoto, H., 2020. Morphology and Morphometry of Sub-kilometer Craters on the Nearside of Phobos and Implications for Regolith Properties. *Transactions of the Japan Society for Aeronautical and Space Sciences*. 63(4), 124-131, DOI: 10.2322/tjsass.63.124.

Morphology and Morphometry of Sub-kilometer Craters on the Nearside of Phobos and Implications for Regolith Properties*

Ryodo HEMMI^{1)†} and Hideaki MIYAMOTO^{1),2)}

¹⁾The University Museum, The University of Tokyo, Tokyo 113–0033, Japan

²⁾Department of Systems Innovation, The University of Tokyo, Tokyo 113–8656, Japan

Estimating the regolith properties of Phobos' surface is of critical importance for the landing and performance of the Martian Moons eXploration (MMX) sample return mission. Regolith physical properties such as strength, regolith thickness, and the presence of regolith layers are related to morphologies of superposing impact craters. However, the accurate depths of Phobos' sub-kilometer-diameter craters including irregularly shaped craters have not yet been fully characterized. Here, by using our high-resolution (20 m/pixel) digital elevation model of the nearside (or the sub-Mars side) of Phobos, we investigate the topographic profiles of the sub-kilometer craters. We confirm the presence of crater rims, and bowl-shaped, central-mound, and flat-floored crater geometries. The topography of one flat-floored crater is consistent with a boundary of regolith layers at a depth of ~160–180 meters. Morphometric measurements of 35 sub-kilometer craters show that their depth-to-diameter (d/D) ratios are in the range of 0.037 and 0.174 (mean value = 0.089, median value = 0.093). This suggests either a surface layer composed of rocky debris that effectively dissipates impact energy and causes a reduction in crater depth, or subsequent resurfacing events changed the original crater topography.

Key Words: Phobos, MMX, Space Science, Remote Sensing, Space Exploration

Nomenclature

d : crater depth, m

D : crater diameter, m

D_A : apparent crater diameter, m

t : regolith layer thickness, m

1. Introduction

For safe operation, determining the surface conditions of target bodies has been crucial to the planning of touchdown/landing for sample-return missions to small bodies (e.g., Hayabusa, Phobos-Grunt, Rosetta, Hayabusa2, OSIRIS-REx, etc.). For instance, Hayabusa2 spacecraft encountered an unprecedented amount of irregular-shaped boulders, ranging in 100s of meters to 10s of centimeters in scale, forming the entire rugged surface of the asteroid Ryugu,^{1–3)} forcing its first touchdown to be rescheduled to allow for additional engineering evaluations of all potential sampling sites. Additionally, the thruster firing at its first touchdown entrained a large number of particles, impairing the Hayabusa2 Optical Navigation Camera by decreasing its light sensitivity. This example illustrates how the dynamic behavior of regolith particles is of great importance when planning for future landing missions.

The Martian Moons eXploration (MMX) mission is planned to land on the surface of Phobos and collect more

than 10 g of samples from depths >2 cm at two separate sites.^{4,5)} High-resolution images (up to several meters per pixel), obtained by spacecraft orbiting Mars revealed that Phobos' surface is mostly covered by impact craters, grooves, pit chains, and boulders (Fig. 1). Craters and boulders smaller than the resolutions of previous images are expected. For the MMX spacecraft design, orbit planning, landing site selection, and landing operation, these densely-distributed topographic obstacles should be fully characterized using existing datasets before launch in 2024. In addition, the properties of regolith layer(s) (e.g., behavior of the surface materials when the lander foot pads and thruster plumes interact with the Phobos regolith, and the strength and packing density of regolith affecting stability of lander legs) should be estimated as accurately as possible.

In the case of Phobos, previous studies have identified two different spectral regions ("red and blue units"^{6–8)}; Fig. 2(a)), a range of morphologies of impact craters, or grooves. The cross-cutting and superposition relationships of these features strongly suggests that there were resurfacing events which produced regolith layers over time. Impact experiments and observations of lunar craters have shown that the contrast of mechanical properties between a loose regolith layer and its substrate affect the morphology of a superposed crater. In particular, changes in regolith thickness are to some extent responsible for changes in the crater morphology (i.e., bowl-shaped, flat-floored, central-mound, or concentric craters).^{9–11)} Crater morphology can therefore provide insights into the properties of subsurface structures (see, for example, Basilevsky et al.¹²⁾), which has not been well demonstrated due to the lack of accurate topography data of planetary surfaces other than the Moon and Mars.

© 2020 The Japan Society for Aeronautical and Space Sciences

*Presented at the 32nd International Symposium on Space Technology and Science, 15–21 June 2019, Fukui, Japan.

Received 30 June 2019; final revision received 29 January 2020; accepted for publication 18 March 2020.

†Corresponding author, hemmi@seed.um.u-tokyo.ac.jp

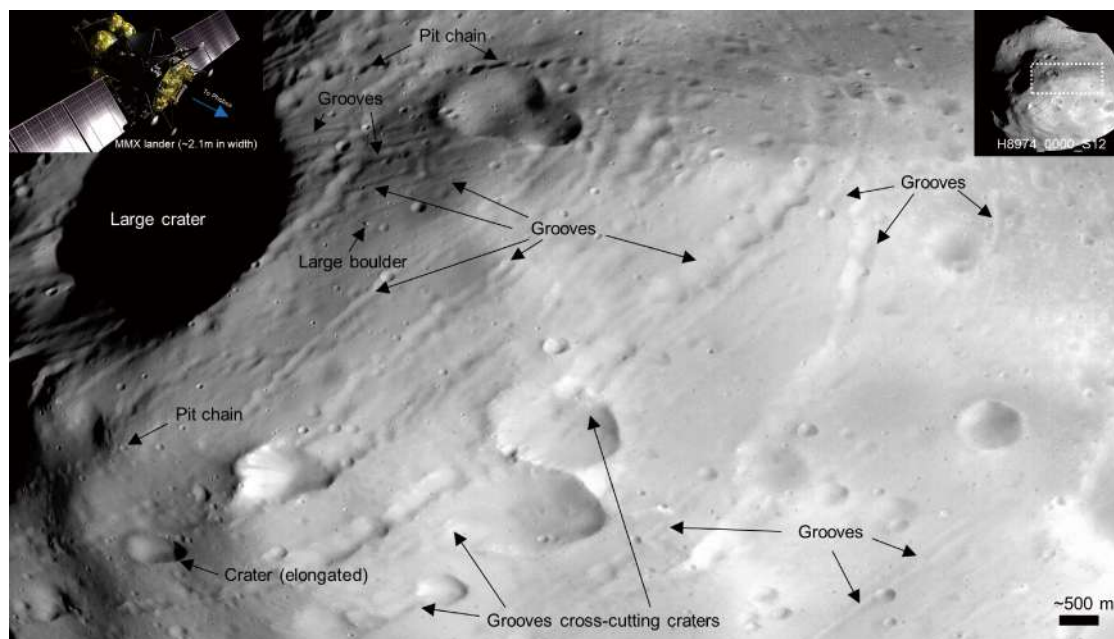


Fig. 1. Close-up view of geomorphological features on the Phobos' surface.
Part of HRSC image H8974_0000_S12. The upper left inset shows a drawing of the MMX spacecraft (Image credit: JAXA).

2. Impact Crater Morphology and Relation to Regolith Layering of Phobos

More than 9,000 craters larger than 50 m in diameter have been counted from the images of the Phobos surface.¹³⁾ Most of them exhibit a bowl-shaped geometry with different degrees of degradation (e.g., shallow crater depths, degraded crater rims, etc.). Some craters are associated with well-preserved elevated rims or rays (Fig. 2(b)), indicating that they were formed by impact rather than internal processes (e.g., drainage of regolith into fractured bedrock).

Morphologies of concentric, flat-floored, and central-mound interiors (e.g., Figs. 2(c)–2(e)) have been observed in craters with diameters ranging from 100s of meters to a few kilometers.^{12,14)} Though Thomas et al.¹⁴⁾ provided first-order estimates of the thickness of a loose surface layer above a mechanically stronger substrate from the diameter of flat-floored or concentric craters,¹¹⁾ their presence and geometry have not been confirmed by accurate topographic profiles using remote sensing data sets recently obtained. Therefore, for example, Basilevsky et al.¹²⁾ interpreted the crater in Fig. 2(e) as a central-mound crater, whereas, Thomas et al.¹⁴⁾ interpreted the same crater as being a flat-floor crater. Morphometric measurements of the craters with $D > 1$ km show that the larger crater depth-to-diameter (d/D) ratios are associated with a larger maximum steepness of the inner slopes.¹²⁾ This, as well as the presence of brighter or darker albedo streaks (Fig. 2(f)) and a landslide deposit (Fig. 2(g)), indicates downslope movement of loose materials in a surficial regolith layer.^{12,15,16)} These findings lead to a range of implications regarding the ages of geological events, the effects of shaking, the thickness of loose regolith layer and/or the characteristics of the subsurface materials.¹²⁾ The potential presence of an upper loose regolith layer would preferen-

tially affect the morphology of the smaller, shallower craters,¹⁷⁾ and yet, the d/D ratios of the Phobos sub-kilometer diameter craters are, so far, uncertain. Therefore, in this study, we extract topographic profiles of small craters with irregular shapes and measure the d/D ratios of craters with $D < \sim 1$ km to constrain the properties of regolith within ~ 100 m of the surface.

3. Data and Methods

3.1. High-resolution digital elevation model of Phobos

We use our recently developed digital elevation model (DEM) of Phobos derived from the application of bundle adjustment and triangulation to HiRISE stereo pair images (Fig. 3(a)).^{18–21)} Our DEM and its orthoimage are tied to a global HRSC Phobos dataset consisting of its own DEM and orthomosaic,^{22,23)} which are projected on a reference sphere having a 11.1 km radius (i.e., the DEM elevations are relative to this sphere) with equidistant cylindrical projection at pixel scales of ~ 20 m and ~ 6.56 m, respectively. With a vertical accuracy of ~ 4.17 m, our DEM covers the areas ranging from $\sim 60^\circ$ W to $\sim 60^\circ$ E (sub-Mars side) and from $\sim 30^\circ$ S to $\sim 70^\circ$ N, including the eastern rim of Stickney Crater, grooves, impact craters, and the red and blue units.²¹⁾

3.2. Measurements of crater diameters and depths

At least 1,000 sub-kilometer craters are present in the DEM coverage area, and we selected 35 craters with diameters from ~ 200 m to ~ 1 km (i.e., they can be resolved using $> 10 \times 10$ DEM pixels). Using the DEM and the orthoimage with the DEM-derived shaded relief map, we first mapped the crater rim-to-rim line passing through the center of each crater in the longitudinal direction (i.e., scale is true along the meridians in a plate carrée projection) (Fig. 3(b)). Topo-

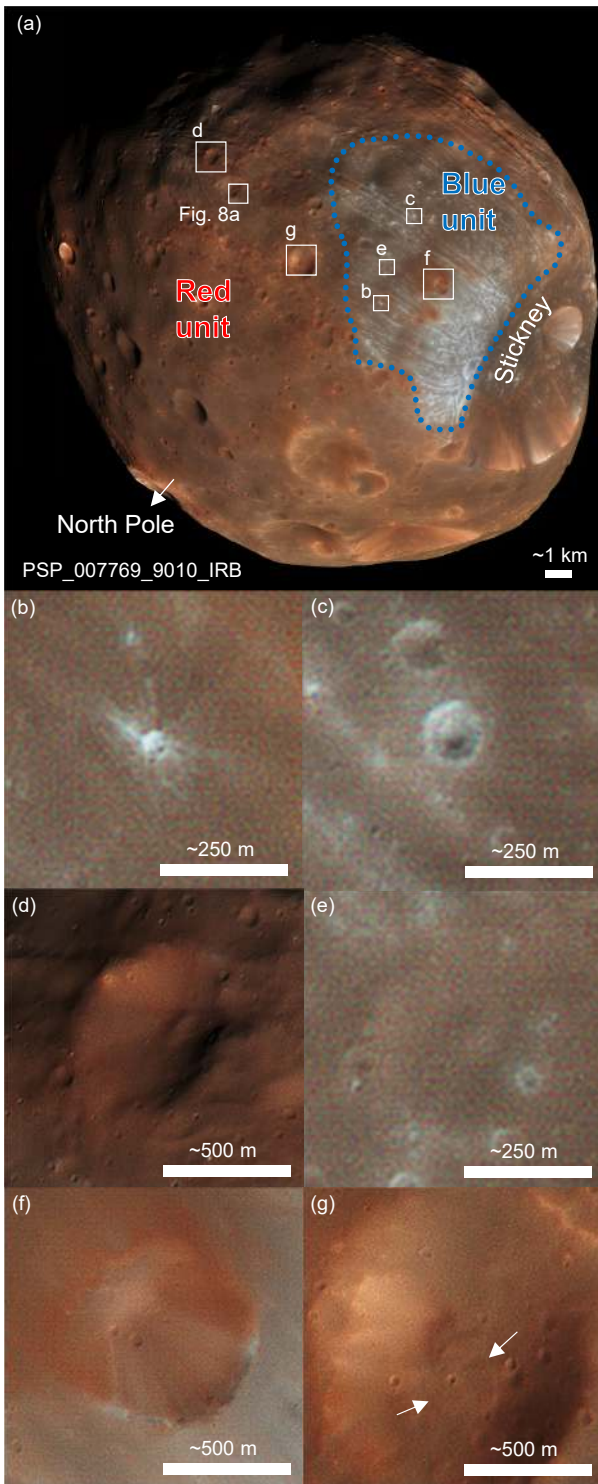


Fig. 2. Color-enhanced HiRISE image of Phobos (Image credit: NASA/JPL/University of Arizona).

(a) Red and blue units. Blue dotted outline depicts an approximate boundary of the blue unit. (b) Rayed crater. (c) Concentric crater. (d) Central-mound crater. (e) Flat-bottomed (or central-mound) crater. (f) Albedo streaks. (g) Landslide deposit (arrows).

graphic profiles were extracted for 35 craters in the DEM using the 3D Analyst tool in ArcGIS (ArcMap 10.2.2). In this study, the D value is defined as the length of a straight line connecting the northern and southern rim crests (i.e., the start and end of the profile), and the d value is calculated as the

length of the longest normal from the rim-to-rim line to the topographic profile. We then corrected the topography-related distortion of the D value, which comes from deviations between the actual surface and the reference sphere.²⁴⁾

4. Results

4.1. Topographic profiles of small craters

As shown in Fig. 4, we obtained topographic profiles of the six small craters (mostly less than 1 km in diameter). The most common morphology is a raised rim on the periphery of each crater, and the absence of the raised rim on one side (Fig. 4(d)) is identified as well. The profile of the crater previously interpreted as a central-mound (or a flat-floored) crater (Fig. 4(b)) exhibits a bowl-shape but has a slightly flat floor.^{12,14)} However, this observation does not exclude the potential presence of a central mound, which was not revealed using our DEM. While the DEM appears to provide an accurate geometry of a bowl-shaped crater (Fig. 4(a)), the elevation profile of a concentric crater (Fig. 4(c)) does not resolve the interior concentric depression seen in the imagery (Fig. 2(c)). This is probably because the vertical and horizontal resolutions of our DEM are insufficient to depict the detailed geometry. A flat-bottomed geometry associated with the crater in Fig. 4(d) is clearly shown in its topographic profile. Topographic profiles of the two central-mound craters (Figs. 4(e) and 4(f)) reveal obvious central mounds with heights reaching ~5 m to ~10 m.

The topography of the ~200 m-long landslide deposit and the associated scarp (Figs. 2(g), 4(d)) reveals its depleted zone/scarp (maximum slope of ~33 deg) on the crater wall and its accumulated zone (~2–4 m-thick landslide body) on the crater floor.^{12,25)}

4.2. Crater depths and diameters

Based on the topographic profiles extracted from the 35 sub-kilometer craters, we find that they have depths of 6.5 m to 136 m (mean = 44.2 m, median = 30.8 m, std. dev. = 35.9 m), and diameters from 177 m to 1,274 m (mean = 440.4 m, median = 376.9 m) (Fig. 5; Table 1). Their d/D ratios are in the range of 0.037 to 0.174 (mean = 0.089, median = 0.093, std. dev. = 0.039). There is no significant difference in the value of d between craters in the red and blue units; but this does not exclude the potential difference in d or d/D values between red and blue units for the sub-kilometer craters not measured in this study or the ones less than 100 m in diameter.

5. Discussion

5.1. Thickness of the regolith layers

The regolith of Phobos should have formed by the excavation, transportation, and mixing of materials at different depths by numerous impacts of different sizes. These processes could have left multi-layered structures within the Phobos regolith.¹⁷⁾ Impact experiments simulating complex craters formed on a loose surficial layer overlying a substrate showed that the ratio of their apparent crater diameters

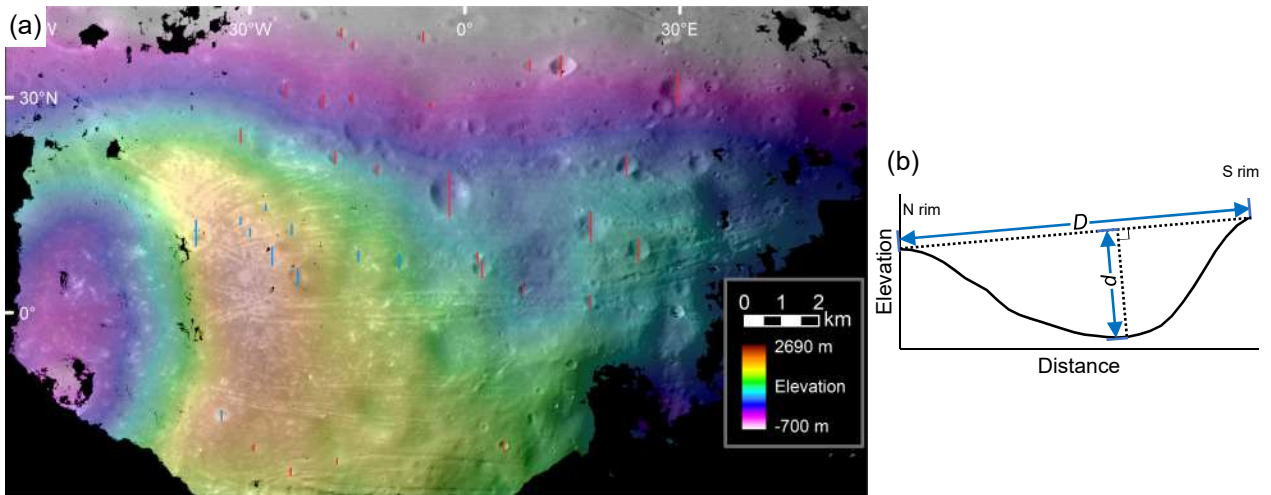


Fig. 3. Morphometric measurements of sub-kilometer craters.

(a) 35 sectional lines through each crater center. Red and blue line colors correspond to craters within the red and blue units, respectively. Base map is HiRISE DEM overlaid on its orthoimage. (b) Diagram showing lengths of d and D values determined from the topographic profile and the rimcrest-to-rimcrest line of each crater.

(i.e., planform diameter) to the layer thickness (D_A/t) can be related to the crater morphology: normal (bowl-shaped) craters at $D_A/t < 3.8$ – 4.2 , flat-bottomed craters (including central-mound craters) at 3.8 – $4.2 < D_A/t < 8$ – 10 , and concentric craters at $D_A/t > 8$ – 10 (Fig. 6).¹¹⁾ We tested this relationship using our high-resolution DEM and orthoimage of Phobos' nearside.

The largest crater measured in this study (Figs. 2(g) and 4(d)) has a flat floor, which may correspond to a boundary between an upper less-compressed (loose) layer and a more compacted substrate.¹¹⁾ From its topographic profile, the elevation difference between the crater floor and the surface outside the crater ($D_A = \sim 1,050$ m) is approximately 160 m–180 m. Treating this depth as the thickness of the overlying regolith layer gives $D_A/t = \sim 5.8$ – 6.6 , which falls within the expected range for flat-bottomed craters. If this analysis is true, then in at least one location, the maximum thickness of the regolith layer is larger than the previous estimate of the maximum layer depth of ~ 100 m derived from the morphology of grooves.^{12,14)} The other three topographic profiles of the ~ 400 m-scale craters (Figs. 4(b), 4(e), 4(f)) suggest ~ 20 m– 25 m as an estimated thickness of potential layer(s); however, their D_A/t values (~ 20 – 25) are greater than those expected for central-mound/flat-bottomed craters. Alternatively, the formation of these complex crater geometries can be explained by post-crater regolith migration and infilling into the crater floors (e.g., ejecta deposits originating from other sites, mass wasting at crater inner walls, etc.), decreasing crater depths and leaving either a flat floor or a central mound. Still, the thickness of the uppermost loose surficial layer may be less than several meters as suggested by the “painted-on” appearance of the red and blue units (Fig. 2(a)), small concentric crater (Fig. 2(c)) and surficial albedo streaks (Fig. 2(f)), which is difficult to determine precisely due to the resolution limit of our DEM (Fig. 4(c)).

5.2. Strengths of the upper loose surface layer

The strengths of regolith layers generally increase with depth, which is not quantitatively understood. The d/D ratios of the 35 sub-kilometer craters ($\sim 0.09 \pm 0.04$) are similar to those of sub-kilometer crater candidates on small (i.e., less than 1 km) asteroids such as Itokawa ($\sim 0.08 \pm 0.03$)²⁶⁾ and Ryugu ($\sim 0.07 \pm 0.03$),²⁷⁾ but are smaller than those of fresh craters on other large (i.e., several kilometers in size) asteroids (0.13 to 0.15).²⁶⁾ Basilevsky et al.¹²⁾ and Karachevtseva et al.²⁸⁾ found that the Phobos craters with $D > \sim 1$ km and $D > 1.5$ km have d/D ranges of ~ 0.02 – 0.21 and 0.04 – 0.21 , respectively (Fig. 7), both of which are larger than the d/D range of sub-kilometer craters (0.04–0.17). This suggests that there may be a change in regolith properties (e.g., spatial variations in regolith strength due to a fractured or rubble-pile interior) at the floors of the craters with diameters of ~ 1 km– 2 km (i.e., ~ 100 m– 300 m below the surrounding plains), which is consistent with the aforementioned layer boundary at depths of ~ 160 m– 180 m.

Moreover, as shown in Fig. 7, most of the craters analyzed with $D < 300$ m have d/D ratios well below 0.10 (i.e., depths $< \sim 30$ m). This may be ascribed to (i) a pre-crater regolith layer boundary (and the associated change in strength) causing the central-mound or flat-bottomed craters, (ii) a pre-existing layer loose rock debris within ~ 30 m of the surface that efficiently dissipates impact energy and results in very shallow craters, or (iii) post-crater processes that reduce crater depths.²⁹⁾ Figure 8(a) shows the profile of extremely shallow crater depths with a flat-floor geometry. Figure 8(b) represents a very gentle slope associated with downslope bright streaks on one side and a very steep slope on the other side. Both crater profiles are suggestive of later depositional events that reduce the depths of these small craters located within both red and blue units. Thus, we favor the two latter interpretations because the first interpretation is at odds with

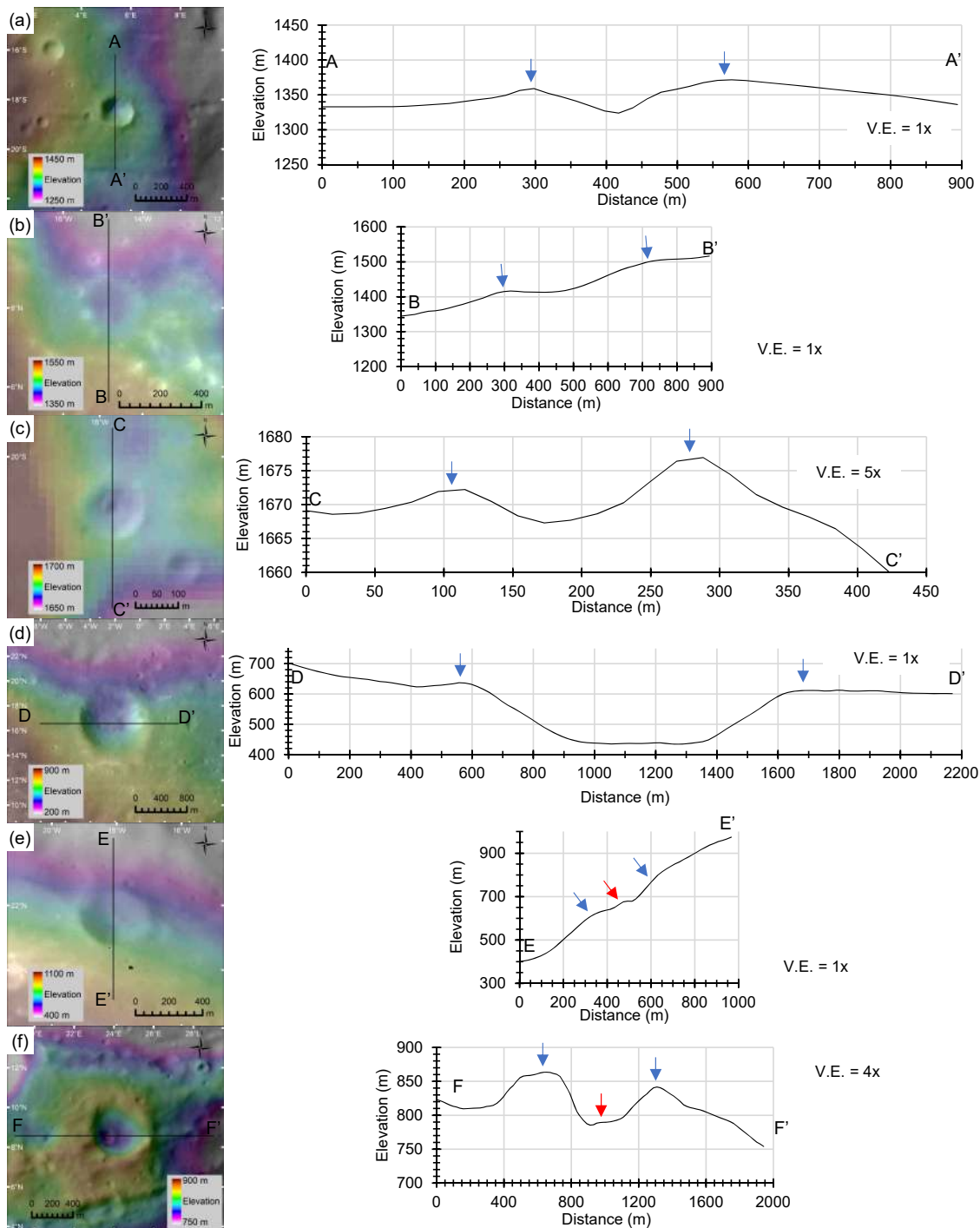


Fig. 4. Topographic profiles (right) for six small craters extracted from map-projected DEMs (left).

Positions of crater rims and central mounds are marked by blue and red arrows in plots, respectively. (a) Bowl-shaped crater. (b) Crater previously interpreted as a flat-floored/central-mound crater. The same crater in Fig. 2(e). (c) Concentric crater. The same crater in Fig. 2(c). (d) Flat-floored crater. The same crater in Fig. 2(g). (e) Central-mound crater. (f) Central-mound crater. The same crater in Fig. 2(d).

the above-described analyses of the D_A/t ratios of the ~ 400 m-sized complex craters.

6. Conclusion

Using the new high-resolution DEM, we extracted the topographic profiles and morphometric parameters of the sub-kilometer diameter craters of Phobos. Topographic profiles of the small flat-bottomed and central-mound craters

provide evidence for: (1) the presence of a boundary between the upper loose regolith layer with a thickness of ~ 160 m– 180 m and a more competent substrate, and (2) post-crater events reducing crater depths and forming flat floors or central mounds. Additionally, a pre-existing loose regolith layer with a thickness of $< \sim 30$ m may have caused a reduction in crater depth during crater formation. Crater depth-to-diameter ratios are comparable to craters on asteroids, which can be explained by a fragmental surface layer

effectively expending impact energy during excavation. In addition, the areas covered by the loose surface layers could have caused landslides on a local scale. These geomorphological aspects should be taken into consideration during the spacecraft design, landing site selection, and landing operation phases of the MMX mission.

To improve the precision of the estimates of this study, in the future, we will investigate (1) the extraction of morphologies of craters tens of meters in diameter, which must be related to a surface layer less than a few meters thick, by developing the much higher-resolution (i.e., several meters per pixel) DEM; (2) high-resolution topographic mapping of the sub-kilometer craters located outside of the study area (i.e., the anti-Mars, leading, trailing, and southern hemi-

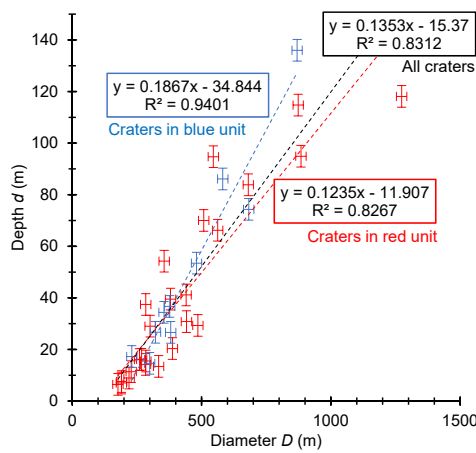


Fig. 5. Morphometric parameter plots of the 35 craters measured.

Red and blue colors represent craters in the red and blue units, respectively.

Table 1. Morphometric parameters of the 35 sub-kilometer craters.

Crater	Longitude	Latitude	d	D	d/D	Unit
00	-24.258	-21.847	11.4	228	0.050	Red
01	-17.834	-20.784	6.5	177	0.037	Red
02	9.126	34.186	15.5	284	0.055	Red
03	-5.778	38.101	29.0	301	0.096	Red
04	-17.238	38.775	16.1	260	0.062	Red
05	-24.951	30.489	30.8	442	0.070	Red
06	17.546	1.400	54.2	355	0.153	Red
07	8.157	2.839	39.5	380	0.104	Red
08	24.234	7.959	83.9	681	0.123	Red
09	29.679	30.224	94.9	884	0.107	Red
10	22.562	19.797	66.2	562	0.118	Red
11	17.594	11.150	114.8	874	0.131	Red
12	5.426	-18.439	37.4	284	0.132	Red
13	2.387	5.621	70.0	508	0.138	Red
14	-31.222	24.392	29.3	486	0.060	Red
15	-12.136	19.761	13.4	334	0.040	Red
16	-29.450	-18.673	7.6	191	0.040	Red
17	-33.900	-14.045	34.4	355	0.097	Blue
18	-14.815	7.432	26.6	381	0.070	Blue
19	13.462	33.777	94.7	546	0.174	Red
20	-4.613	28.934	7.0	190	0.037	Red
21	-15.626	29.676	14.2	283	0.050	Red
22	-15.527	37.088	9.0	220	0.041	Red
23	-19.756	29.165	20.3	387	0.053	Red
24	1.766	7.483	16.2	268	0.060	Red
25	-9.101	6.565	53.5	481	0.111	Blue
26	-23.294	4.744	86.1	582	0.148	Blue
27	-2.144	15.032	118.1	1274	0.093	Red
28	-18.103	21.287	41.1	440	0.093	Red
29	-37.448	11.573	136.0	869	0.156	Blue
30	-24.152	11.258	36.7	377	0.097	Blue
31	-26.863	7.169	74.3	682	0.109	Blue
32	-31.262	12.653	14.6	299	0.049	Blue
33	-29.943	10.959	26.7	322	0.083	Blue
34	-27.738	14.458	17.3	230	0.075	Blue

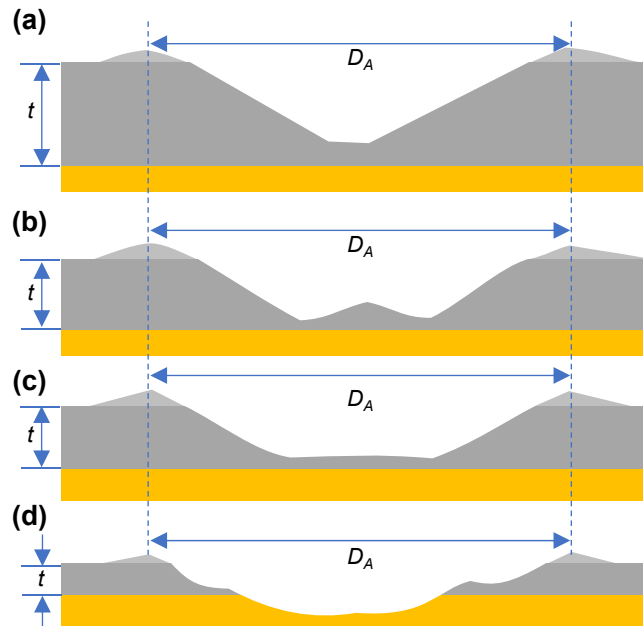


Fig. 6. Diagram showing the cross-sections of normal and complex craters formed on the loose unconsolidated layer (gray) overlying cohesive substrate (orange), which relates an apparent crater diameter of crater (D_A) to the layer thickness (t). Redrawn from Quaide and Oberbeck (1968).¹¹⁾

(a) Bowl-shaped crater ($D_A/t < 3.8-4.2$). (b) Central-mound crater ($3.8-4.2 < D_A/t < 8-10$). (c) Flat-bottomed crater ($3.8-4.2 < D_A/t < 8-10$). (d) Concentric crater ($D_A/t > 8-10$).

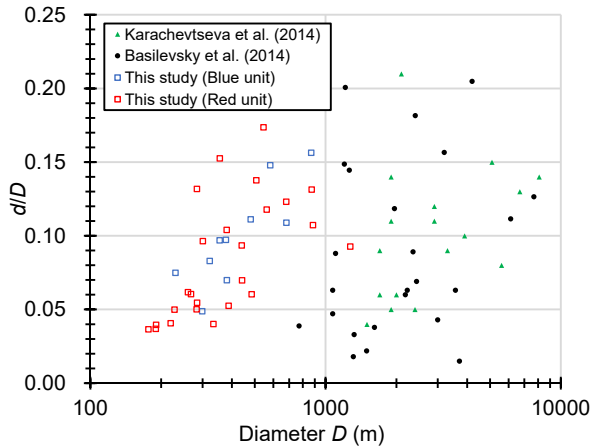


Fig. 7. Comparison of d/D ratios between the sub-kilometer craters and the previously-studied larger craters ($D > 1$ km).

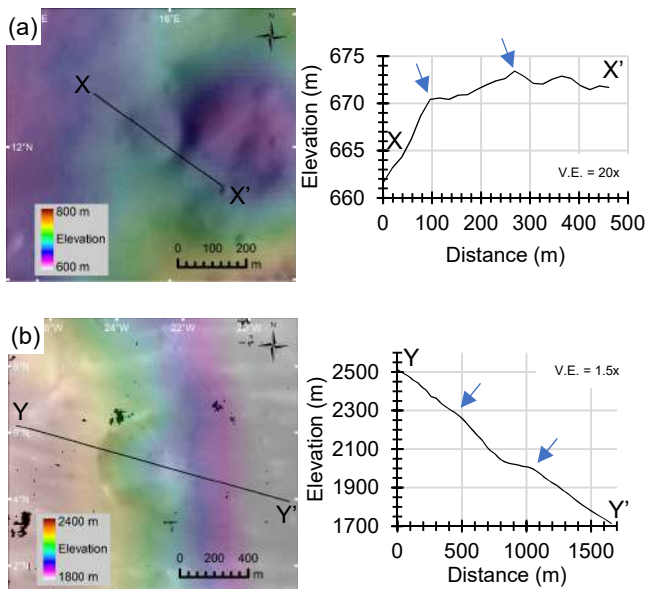


Fig. 8. Profiles of sub-kilometer craters with decreased crater depths.

(a) A flat-floored crater with very shallow interior. This crater is located within the red unit. (b) A crater with bright streaks on its western slope (Fig. 2(f)) showing an asymmetry of its interior profile. This crater is located within the blue unit.

spheres, and higher-latitude areas); and (3) integrating the morphometric measurements of the small craters, grooves, and other features (e.g., grooves, pit chains, albedo streams, etc.), including those automatically identified by MMX's TENGGO/OROCHI images with lossy compression,³⁰ into a criteria or a hazard risk map based on regolith property estimates and a dynamic slope map for evaluating the safety of prospective landing sites.

Acknowledgments

We are grateful to an anonymous referee for his/her helpful comments. We wish to express our sincere appreciation to the MMX Landing Operation Working Team (LOWT), the TOKYO DOME CORPORATION, and the NTT DATA Corporation for their great support. We also thank Dr. Reid Parsons for his helpful comments on the manuscript.

References

- 1) Sugita, S., Honda, R., Morota, T., Kameda, S., Sawada, H., Tatsumi, E., Yamada, M., Honda, C., Yokota, Y., Kouyama, T., Sakatani, N., Ogawa, K., Suzuki, H., Okada, T., Namiki, N., Tanaka, S., Iijima, Y., Yoshioka, K., Hayakawa, M., Cho, Y., Matsuoka, M., Hirata, N., Miyamoto, H., Domingue, D., Hirabayashi, M., Nakamura, T., Hiroi, T., Michikami, T., Michel, P., Ballouz, R. L., Barnouin, O. S., Ernst, C. M., Schröder, S. E., Kikuchi, H., Hemmi, R., Komatsu, G., Fukuhara, T., Taguchi, M., Arai, T., Senshu, H., Demura, H., Ogawa, Y., Shimaki, Y., Sekiguchi, T., Müller, T. G., Hagermann, A., Mizuno, T., Noda, H., Matsumoto, K., Yamada, R., Ishihara, Y., Ikeda, H., Araki, H., Yamamoto, K., Abe, S., Yoshida, F., Higuchi, A., Sasaki, S., Oshigami, S., Tsuruta, S., Asari, K., Tazawa, S., Shizugami, M., Kimura, J., Otsubo, T., Yabuta, H., Hasegawa, S., Ishiguro, M., Tachibana, S., Palmer, E., Gaskell, R., Le Corre, L., Jaumann, R., Otto, K., Schmitz, N., Abell, P. A., Barucci, M. A., Zolensky, M. E., Vilas, F., Thuillet, F., Sugimoto, C., Takaki, N., Suzuki, Y., Kamiyoshihara, H., Okada, M., Nagata, K., Fujimoto, M., Yoshikawa, M., Yamamoto, Y., Shirai, K., Noguchi, R., Ogawa, N., Terui, F., Kikuchi, S., Yamaguchi, T., Oki, Y., Takao, Y., Takeuchi, H., Ono, G., Mimasu, Y., Yoshikawa, K., Takahashi, T., Takei, Y., Fujii, A., Hirose, C., Nakazawa, S., Hosoda, S., Mori, O., Shimada, T., Soldini, S., Iwata, T., Abe, M., Yano, H., Tsukizaki, R., Ozaki, M., Nishiyama, K., Saiki, T., Watanabe, S., and Tsuda, Y.: The Geomorphology, Color, and Thermal Properties of Ryugu: Implications for Parent-Body Processes, *Science*, **364** (2019), eaaw0422.
- 2) Watanabe, S., Hirabayashi, M., Hirata, N., Noguchi, R., Shimaki, Y., Ikeda, H., Tatsumi, E., Yoshikawa, M., Kikuchi, S., Yabuta, H., Nakamura, T., Tachibana, S., Ishihara, Y., Morota, T., Kitazato, K., Sakatani, N., Matsumoto, K., Wada, K., Senshu, H., Honda, C., Michikami, T., Takeuchi, H., Kouyama, T., Honda, R., Kameda, S., Fuse, T., Miyamoto, H., Komatsu, G., Sugita, S., Okada, T., Namiki, N., Arakawa, M., Ishiguro, M., Abe, M., Gaskell, R., Palmer, E., Barnouin, O. S., Michel, P., French, A. S., McMahon, J. W., Scheeres, D. J., Abell, P. A., Yamamoto, Y., Tanaka, S., Shirai, K., Matsuoka, M., Yamada, M., Yokota, Y., Suzuki, H., Yoshioka, K., Cho, Y., Nishikawa, N., Sugiyama, T., Kikuchi, H., Hemmi, R., Yamaguchi, T., Ogawa, N., Ono, G., Mimasu, Y., Yoshikawa, K., Takahashi, T., Takei, Y., Fujii, A., Hirose, C., Iwata, T., Hayakawa, M., Hosoda, S., Mori, O., Sawada, H., Shimada, T., Soldini, S., Yano, H., Tsukizaki, R., Ozaki, M., Iijima, Y., Ogawa, K., Fujimoto, M., Ho, T. M., Moussi, A., Jaumann, R., Bibring, J. P., Krause, C., Terui, F., Saiki, T., Nakazawa, S., and Tsuda, Y.: Hayabusa2 Arrives at the Carbonaceous Asteroid 162173 Ryugu—A Spinning Top-Shaped Rubble Pile, *Science*, **364** (2019), pp. 268–272.
- 3) Michikami, T., Honda, C., Miyamoto, H., Hirabayashi, M., Hagermann, A., Irie, T., Nomura, K., Ernst, C. M., Kawamura, M., Sugimoto, K., Tatsumi, E., Morota, T., Hirata, N., Noguchi, T., Cho, Y., Kameda, S., Kouyama, T., Yokota, Y., Noguchi, R., Hayakawa, M., Hirata, N., Honda, R., Matsuoka, M., Sakatani, N., Suzuki, H., Yamada, M., Yoshioka, K., Sawada, H., Hemmi, R., Kikuchi, H., Ogawa, K., Watanabe, S.-i., Tanaka, S., Yoshikawa, M., Tsuda, Y., and Sugita, S.: Boulder Size and Shape Distributions on Asteroid Ryugu, *Icarus*, **331** (2019), pp. 179–191.
- 4) Kuramoto, K., Kawakatsu, Y., Fujimoto, M., and MMX Study Team: Martian Moons Exploration (MMX) Conceptual Study Results, 48th Lunar and Planetary Science Conference, The Woodlands, Texas, 2086, 2017.
- 5) Kuramoto, K., Kawakatsu, Y., Fujimoto, M., Genda, H., Imamura, T., Kameda, S., Matsumoto, K., Miyamoto, H., Morota, T., and Nagaoka, H.: Martian Moons Exploration (MMX) Conceptual Study Update, 49th Lunar and Planetary Science Conference, The Woodlands, Texas, 2143, 2018.
- 6) Murchie, S. and Erard, S.: Spectral Properties and Heterogeneity of Phobos from Measurements by Phobos 2, *Icarus*, **123** (1996), pp. 63–86.
- 7) Rivkin, A. S., Brown, R. H., Trilling, D. E., Bell, J. F., and Plassmann, J. H.: Near-Infrared Spectrophotometry of Phobos and Deimos, *Icarus*,

- 156 (2002), pp. 64–75.
- 8) Fraeman, A. A., Arvidson, R. E., Murchie, S. L., Rivkin, A., Bibring, J. P., Choo, T. H., Gondet, B., Humm, D., Kuzmin, R. O., Manaud, N., and Zabalueva, E. V.: Analysis of Disk-Resolved OMEGA and CRISM Spectral Observations of Phobos and Deimos, *J. Geophys. Res. Planets*, **117** (2012), E00J15.
 - 9) Wilcox, B. B., Robinson, M. S., Thomas, P. C., and Hawke, B. R.: Constraints on the Depth and Variability of the Lunar Regolith, *Meteorit. Planet. Sci.*, **40** (2005), pp. 695–710.
 - 10) Bart, G. D.: The Quantitative Relationship between Small Impact Crater Morphology and Regolith Depth, *Icarus*, **235** (2014), pp. 130–135.
 - 11) Quaide, W. L. and Oberbeck, V. R.: Thickness Determinations of the Lunar Surface Layer from Lunar Impact Craters, *J. Geophys. Res.*, **73** (1968), pp. 5247–5270.
 - 12) Basilevsky, A. T., Lorenz, C. A., Shingareva, T. V., Head, J. W., Ramsley, K. R., and Zubarev, A. E.: The Surface Geology and Geomorphology of Phobos, *Planet. Space Sci.*, **102** (2014), pp. 95–118.
 - 13) Salamunićar, G., Lončarić, S., Pina, P., Bandeira, L., and Saraiva, J.: Integrated Method for Crater Detection from Topography and Optical Images and the New PH9224GT Catalogue of Phobos Impact Craters, *Adv. Space Res.*, **53** (2014), pp. 1798–1809.
 - 14) Thomas, P. C., Veverka, J., Sullivan, R., Simonelli, D. P., Malin, M. C., Caplinger, M., Hartmann, W. K., and James, P. B.: Phobos: Regolith and Ejecta Blocks Investigated with Mars Orbiter Camera Images, *J. Geophys. Res. Planets*, **105** (2000), pp. 15091–15106.
 - 15) Shingareva, T. V. and Kuzmin, R. O.: Mass-Wasting Processes on the Surface of Phobos, *Solar Syst. Res.*, **35** (2001), pp. 431–443.
 - 16) Shi, X., Oberst, J., and Willner, K.: Mass Wasting on Phobos Triggered by an Evolving Tidal Environment, *Geophys. Res. Lett.*, **43** (2016), pp. 12,371–12,379.
 - 17) Ramsley, K. R. and Head, J. W.: Mars Impact Ejecta in the Regolith of Phobos: Bulk Concentration and Distribution, *Planet. Space Sci.*, **87** (2013), pp. 115–129.
 - 18) Beyer, R. A., Alexandrov, O., and McMichael, S.: The Ames Stereo Pipeline: NASA's Open Source Software for Deriving and Processing Terrain Data, *Earth Space Sci.*, **5** (2018), pp. 537–548.
 - 19) Hemmi, R. and Miyamoto, H.: Distribution, Morphology, and Morphometry of Circular Mounds in the Elongated Basin of Northern Terra Sirenum, Mars, *Prog. Earth Planet. Sci.*, **4** (2017), 26.
 - 20) Hemmi, R. and Miyamoto, H.: High-Resolution Topographic Analyses of Mounds in Southern Acidalia Planitia, Mars: Implications for Possible Mud Volcanism in Submarine and Subaerial Environments, *Geosciences*, **8** (2018), 152.
 - 21) Hemmi, R. and Miyamoto, H.: HiRISE Digital Elevation Model of Phobos: Implications for Morphological Analysis of Grooves, 50th Lunar and Planetary Science Conference, The Woodlands, Texas, 1759, 2019.
 - 22) Willner, K., Shi, X., and Oberst, J.: Phobos' Shape and Topography Models, *Planet. Space Sci.*, **102** (2014), pp. 51–59.
 - 23) Wählisch, M., Stooke, P. J., Karachevtseva, I. P., Kirk, R., Oberst, J., Willner, K., Nadejdina, I. A., Zubarev, A. E., Konopikhin, A. A., and Shingareva, K. B.: Phobos and Deimos Cartography, *Planet. Space Sci.*, **102** (2014), pp. 60–73.
 - 24) Kneissl, T., Schmedemann, N., Neesemann, A., Raymond, C. A., and Russell, C. T.: Crater Counting on Small Bodies—The Influence of Topography-Related Distortions, 45th Lunar and Planetary Science Conference, The Woodlands, Texas, 2398, 2018.
 - 25) Thomas, N., Stelter, R., Ivanov, A., Bridges, N. T., Herkenhoff, K. E., and McEwen, A. S.: Spectral Heterogeneity on Phobos and Deimos: HiRISE Observations and Comparisons to Mars Pathfinder Results, *Planet. Space Sci.*, **59** (2011), pp. 1281–1292.
 - 26) Hirata, N., Barnouin-Jha, O. S., Honda, C., Nakamura, R., Miyamoto, H., Sasaki, S., Demura, H., Nakamura, A. M., Michikami, T., Gaskell, R. W., and Saito, J.: A Survey of Possible Impact Structures on 25143 Itokawa, *Icarus*, **200** (2009), pp. 486–502.
 - 27) Cho, Y., Morota, T., Kanamaru, M., Ernst, C. M., Barnouin, O. S., Tatsumi, E., Hirabayashi, M., Otto, K. A., Schmitz, N., and Wagner, R. J.: Spatial Distribution and Morphology of Craters on Ryugu: Implications for Surface Processes on the C-Type Asteroid, 50th Lunar and Planetary Science Conference, The Woodlands, Texas, 1751, 2019.
 - 28) Karachevtseva, I. P., Oberst, J., Zubarev, A. E., Nadezhkina, I. E., Kokhanov, A. A., Garov, A. S., Uchaev, D. V., Uchaev, Dm. V., Malinnikov, V. A., and Klimkin, N. D.: The Phobos Information System, *Planet. Space Sci.*, **102** (2014), pp. 74–85.
 - 29) Melosh, H. J.: *Impact Cratering: a Geologic Process*, Oxford University Press, New York, 1989, pp. 82–84.
 - 30) Shimizu, Y., Kamiyoshihara, H., Niihara, T., and Miyamoto, H.: Experimental Study to Determine the Best Compression Ratio of High-Resolution Images of Small Bodies for Martian Moons eXploration Mission, *Trans. Jpn. Soc. Aeronaut. Space Sci.*, in press.

Tatsuaki Okada
Associate Editor

Chapter 6

Summary and Outlook

6.1 Summary

This thesis focuses on the importance and scientific values of high-resolution DEMs and presents the new framework to develop high-accuracy DEMs from high-resolution stereo-pair images. This can have broader applicability to not only Mars and Phobos but other bodies, such as the Moon, the other satellites, small bodies, etc, which will be explored by future explorations.

In Chapter 1, I overviewed the current status of the topographic mapping of Mars and Phobos. From the 2020s, NASA/ESA's Mars landing/sample return and JAXA's Phobos sample return missions are scheduled and underway. Past remote observations have already achieved global image and topography mapping of Mars and Phobos. In particular, visible images taken by the HiRISE camera aboard MRO are acquired at about 25 cm per pixel about 6 m per pixel for the surfaces of Mars and Phobos, respectively. However, the number of publicly available HiRISE DTMs is very small (less than 6% of all stereo DEMs out of more than 13,000 stereo pairs), and no public HiRISE DEM exists for Phobos, which is critical for future mission planning. This is mainly due to the existing HiRISE image data processing process, which should be improved in terms of spacecraft/camera position/pointing.

In Chapter 2, I presented a new HiRISE data processing pipeline to improve the accuracy of the DEM. For the Mars image processing, the new pipeline includes the generation of CTX stereo DEMs aligned to the MOLA footprints, the acquisition of GCPs between CTX and HiRISE images, the correction of HiRISE camera position and orientation, etc. For the Phobos image processing, its pipeline includes derived from the extraction of the GCPs using global HRSC DEM/orthoimage, the update on the SPICE data of the HiRISE stereo pair, etc.

In Chapter 3, by using the four high-accuracy DEMs, I investigated the distribution, morphology, and morphometry of circular mounds in the elongated basin of northern Terra Sirenum, Mars. These characteristics are consistent with the deposition and extension of mud slurries with mud breccia and gases extruded from the subsurface, almost equivalent to terrestrial mud volcanism. If so, the abundance of groundwater, with the abrupt increase in pore fluid pressure, is necessary for triggering mud eruption. Based on their absolute crater retention ages and geological mapping results, the mounds superposed on the Late Hesperian-aged basin floor, and the faults and fissures (part of Memnonia Fossae) are thought to have formed during and/or after the period of mound formation. This suggests a high hydrological potential, which is significant for landing site selections and resource utilization of future Mars missions. Further study, or perhaps future sample return, will reveal whether the mounds are composed of igneous or sedimentary source materials, as well as the frequency/timing/flux of their depositional/erosional events.

In Chapter 4, based on newly developed DEMs, I showed high-resolution topographic analyses of pitted mounds in southern Acidalia Planitia of Martian northern lowlands, which is a purported paleo-ocean during the Noachian and/or Hesperian times. The densely distributed mounds in Chryse and Acidalia Planitia were suggested to be ancient mud volcanoes formed in an aqueous setting, which was controversial (i.e., mud vs. igneous and submarine vs. subaerial). I accurately measured the heights and diameters of ~1300 mounds resulted in good accordance with those of mud and igneous volcanoes in submarine/subaerial settings on Earth in terms of depths of their source reservoirs and the estimated rheological properties of mound-forming materials. The conditions of possible submarine mud or igneous volcanoes may have harbored less hazardous environments for past life on Mars than those on an ocean-free surface, which is significant for

astrobiological studies of future Mars missions. An in-situ investigation will reveal the origin of pitted mounds (e.g., the Chinese Mars rover will approach the mounds in Utopia Planitia on the northern lowlands of Mars, which were interpreted as mud volcanoes).

In Chapter 5, I showed the morphology and morphometry of sub-kilometer craters on the nearside of Phobos. Estimating the regolith properties of Phobos' surface is of critical importance for the landing and performance of the Martian Moons eXploration (MMX) sample return mission. By developing a new high-resolution (20m/pixel) DEM of the nearside (or the sub-Mars side) of Phobos, I investigated the topographic profiles of the sub-kilometer craters, showing the presence of crater rims, and bowl-shaped, central-mound, and flat-floored crater geometries. The topography of one flat-floored crater is consistent with a boundary of regolith layers at a depth of ~160–180 meters. Morphometric measurements of 35 sub-kilometer craters show that their depth-to-diameter (d/D) ratios could have resulted from either the presence of an initial surface layer dissipating impact energy, subsequent resurfacing events, or terrain degradation.

Original data products, e.g., my new HiRISE/CTX DEMs and orthoimages, along with relevant command lines (ISIS3, ASP, GDAL), will be provided in the online repository or my forthcoming publication.

6.2 Outlook

Finally, the improvements of the DEM extraction pipeline can be commonly applied to the line-scan images of the other planetary surfaces. A good example is the Lunar Reconnaissance Orbiter Camera (LROC) Narrow Angle Cameras (NACs) (Robinson et al., 2010) images and their stereo-derived DEMs (Henriksen et al., 2017). I have demonstrated the increase in the NAC DEM precision by the manual co-registration of the NAC-Left/Right EDRs (Hemmi et al., 2020), which will be applied to the CCD image-to-image registration of ten HiRISE RED CCD images.

A series of image processing steps (i.e., the combination of co-registration, transformation, and mosaicking) has not been performed to date and not tested in this thesis. However, it is required for minimizing DEM precision issues (e.g., Figure 1.5), which have to be addressed in the future. Additionally, refined spacecraft interior orientations (camera distortions, CCD seams) and exterior orientations (spacecraft position and pointing) will improve the precision of SfS-derived DEMs of planetary surfaces (e.g., Hemmi, 2020; Hemmi et al., 2020), which have three or more times better grid spacings than those of stereo-derived DEMs.

For the improvement of computation efficiency, the automation of GCP generation with high accuracy is another issue to be addressed in the future, especially for producing the GCPs tying the MRO HiRISE images to the MRO CTX/Mars Express HRSC/MOLA base map and the GCPs tying the LROC NAC images to the LROC WAC/Kaguya Terrain Camera/Lunar Orbiter Laser Altimeter base map.

The methodology and resultant products developed in the thesis have already been used for the preliminary study of two forthcoming missions, MMX and Lunar Polar Exploration (LUPEX). From the 2020s, there is no doubt that high-accuracy DEM products, DEM extraction methods, geospatial data analysis, geological mapping, etc. will greatly help scientists, engineers, and perhaps astronauts on planetary surfaces, who will be involved in future deep-space exploration missions to the solar system bodies.

References for Chapters 1, 2, and 6

- Aati, S., Avouac, J.-P., 2020. Optimization of Optical Image Geometric Modeling, Application to Topography Extraction and Topographic Change Measurements Using PlanetScope and SkySat Imagery. *Remote Sensing*. 12, 3418.
- Acton, C., Bachman, N., Semenov, B., Wright, E., 2018. A look towards the future in the handling of space science mission geometry. *Planetary and Space Science*. 150, 9-12.
- Acton, C. H., 1996. Ancillary data services of NASA's Navigation and Ancillary Information Facility. *Planetary and Space Science*. 44, 65-70.
- Baker, D. M. H., Head, J. W., 2015. Extensive Middle Amazonian mantling of debris aprons and plains in Deuteronilus Mensae, Mars: Implications for the record of mid-latitude glaciation. *Icarus*. 260, 269-288.
- Becker, K. J., et al., 2015. Criteria for automated identification of stereo image pairs. 46th Lunar and Planetary Science Conference, The Woodlands, Texas.
- Beyer, R. A., Alexandrov, O., McMichael, S., 2018. The Ames Stereo Pipeline: NASA's Open Source Software for Deriving and Processing Terrain Data. *Earth and Space Science*. 5, 537-548.
- Beyer, R. A., Alexandrov, O., Moratto, Z. M., 2014. Aligning terrain model and laser altimeter point clouds with the Ames Stereo Pipeline. 45th Lunar and Planetary Science Conference, The Woodlands, Texas.
- Bhardwaj, A., Sam, L., Martin-Torres, F. J., Zorzano, M.-P., 2019. Distribution and Morphologies of Transverse Aeolian Ridges in ExoMars 2020 Rover Landing Site. *Remote Sensing*. 11, 912.
- Bridges, N. T., Ayoub, F., Avouac, J. P., Leprince, S., Lucas, A., Mattson, S., 2012. Earth-like sand fluxes on Mars. *Nature*. 485, 339.
- Broxton, M. J., Edwards, L. J., 2008. The Ames Stereo Pipeline: Automated 3D surface reconstruction from orbital imagery. 39th Lunar and Planetary Science Conference, League City, Texas.
- Carr, M. H., 2007. *The Surface of Mars*. Cambridge University Press, Cambridge.
- Carrivick, J. L., Smith, M. W., Quincey, D. J., 2016. *Structure from Motion in the Geosciences*. John Wiley & Sons.
- Chojnacki, M., Banks, M., Urso, A., 2018. Wind-Driven Erosion and Exposure Potential at Mars 2020 Rover Candidate-Landing Sites. *Journal of Geophysical Research: Planets*. 123, 468-488.
- Edmundson, K. L., Cook, D. A., Thomas, O. H., Archinal, B. A., Kirk, R. L., 2012. Jigsaw: The ISIS3 bundle adjustment for extraterrestrial photogrammetry. *ISPRS Ann. Photogramm. Remote Sens. Spatial Inf. Sci.* I-4, 203-208.
- Ehlmann, B. L., Edwards, C. S., 2014. Mineralogy of the Martian Surface. *Annual Review of Earth and Planetary Sciences*. 42, 291-315.
- Eliason, E., Castalia, B., Leis, R., Becker, K., 2007. Software Interface Specification for HiRISE Experimental Data Record Products. Jet Propulsion Laboratory, NASA.
- Ernst, C. M., Gaskell, R. W., Barnouin, O. S., Daly, R. T., 2018. A Complete, Coregistered, and Searchable Collection of Phobos and Deimos Images from 1975—2016. 49th Lunar and Planetary Science Conference, The Woodlands, Texas.
- Ernst, C. M., Gaskell, R. W., Kahn, E. G., Barnouin, O. S., Roberts, J. H., Wilcomb, K. K., 2015. Updated Shape Models of Phobos and Deimos from Stereophotoclinometry. 46th Lunar and Planetary Science Conference, The Woodlands, Texas.
- Farr, T. G., et al., 2007. The Shuttle Radar Topography Mission. *Reviews of Geophysics*. 45.
- Ferguson, R. L., et al., 2020. Mars 2020 Terrain Relative Navigation Flight Product Generation: Digital Terrain Model and Orthorectified Image Mosaic. 51st Lunar and Planetary Science Conference, The Woodlands, Texas, pp. 2020.

- Ferguson, R. L., et al., 2017. Analysis of Local Slopes at the InSight Landing Site on Mars. *Space Science Reviews*. 211, 109-133.
- Ferguson, R. L., Lee, E. M., Weller, L., 2013. THEMIS geodetically controlled mosaics of Mars. 44th Lunar and Planetary Science Conference, The Woodlands, Texas.
- Ferguson, R. L., Weller, L., 2018. The Importance of Geodetically Controlled Data Sets: THEMIS Controlled Mosaics of Mars, a Case Study. *Planetary Science Informatics and Data Analytics Conference*, Vol. 2082, St. Louis, Missouri.
- Gaskell, R. W., 2011. Phobos Shape Model V1.0. NASA Planetary Data System. VO1-SA-VISA/VISB-5-PHOBOSSHAPE-V1.0.
- Geng, X., Xu, Q., Xing, S., Lan, C., 2019. A Robust Ground-to-Image Transformation Algorithm and Its Applications in the Geometric Processing of Linear Pushbroom Images. *Earth and Space Science*. 6, 1805-1830.
- Geng, X., Xu, Q., Xing, S., Lan, C., 2020. A Generic Pushbroom Sensor Model for Planetary Photogrammetry. *Earth and Space Science*. 7, e2019EA001014.
- Giese, B., Oberst, J., Scholten, F., Hoffmann, H., Spiegel, M., Neukum, G., 2005. Ein hoch auflösendes digitales Oberflächenmodell des Marsmondes Phobos. *Photogrammetrie Fernerkundung Geoinformation*. 435-440.
- Golombek, M., et al., 2017. Selection of the InSight Landing Site. *Space Science Reviews*. 211, 5-95.
- Gwinner, K., et al., 2010. Topography of Mars from global mapping by HRSC high-resolution digital terrain models and orthoimages: Characteristics and performance. *Earth and Planetary Science Letters*. 294, 506-519.
- Gwinner, K., et al., 2009. Derivation and Validation of High-Resolution Digital Terrain Models from Mars Express HRSC Data. *Photogrammetric Engineering & Remote Sensing*. 75, 1127-1142.
- Hargitai, H., Willner, K., Buchroithner, M., 2019 Methods in Planetary Topographic Mapping: A Review. In: H. Hargitai, (Ed.), *Planetary Cartography and GIS*. Springer International Publishing, Cham, pp. 147-174.
- Harrison, S. K., Balme, M. R., Hagermann, A., Murray, J. B., Muller, J. P., Wilson, A., 2013. A branching, positive relief network in the middle member of the Medusae Fossae Formation, equatorial Mars—Evidence for sapping? *Planetary and Space Science*. 85, 142-163.
- Hemmi, R., 2020. Small craters on the nearside of Phobos: Morphology and degradation. *AGU Fall Meeting Abstracts*, Vol. 2020, pp. P034-0006.
- Hemmi, R., Miyamoto, H., 2019. HiRISE digital elevation model of Phobos: Implications for morphological analysis of grooves. 50th Lunar and Planetary Science Conference, The Woodlands, Texas.
- Hemmi, R., et al., 2020. High-Precision Digital Terrain Model of a Candidate Landing Site Near Lunar South Pole Using Multi-Image Shape-from-Shading. 51st Lunar and Planetary Science Conference, The Woodlands, Texas.
- Hemmi, R., Miyamoto, H., Parsons, R., 2018. Geological activities on present-day Mars and implications for future Mars missions [in Japanese]. *Planetary People - The Japanese Society for Planetary Sciences*. 27, 152-162.
- Henriksen, M. R., et al., 2017. Extracting accurate and precise topography from LROC narrow angle camera stereo observations. *Icarus*. 283, 122-137.
- Hepburn, A. J., Holt, T., Hubbard, B., Ng, F., 2019. Creating HiRISE digital elevation models for Mars using the open-source Ames Stereo Pipeline. *Geosci. Instrum. Method. Data Syst*. 8, 293-313.
- International Space Exploration Coordination Group, 2018. The Global Exploration Roadmap. National Aeronautics and Space Administration.
- Ivanov, A. B., Thomas, N., 2010. Reconstruction of a digital elevation model for Phobos from HiRISE Data. 41st Lunar and Planetary Science Conference, The Woodlands, Texas.

- Jacobsen, K., Topan, H., 2015. DEM GENERATION WITH SHORT BASE LENGTH PLEIADES TRIPLET. *Int. Arch. Photogramm. Remote Sens. Spatial Inf. Sci.* XL-3/W2, 81-86.
- Johnson, A. E., Cheng, Y., Montgomery, J. F., Trawny, N., Tweddle, B., Zheng, J. X., 2015 Real-Time Terrain Relative Navigation Test Results from a Relevant Environment for Mars Landing. *AIAA Guidance, Navigation, and Control Conference*. American Institute of Aeronautics and Astronautics.
- Johnson, A. E., Huertas, A., Werner, R. A., Montgomery, J. F., 2008. Analysis of On-Board Hazard Detection and Avoidance for Safe Lunar Landing. *2008 IEEE Aerospace Conference*, pp. 1-9.
- Kikuchi, S., et al., 2020. Design and Reconstruction of the Hayabusa2 Precision Landing on Ryugu. *Journal of Spacecraft and Rockets*. 57, 1033-1060.
- Kim, J. R., Muller, J. P., 2009. Multi-resolution topographic data extraction from Martian stereo imagery. *Planetary and Space Science*. 57, 2095-2112.
- Kirk, R. L., et al., 2020. Evaluating stereo DTM quality at Jezero Crater, Mars with HRSC, CTX, and HiRISE images. *Int. Arch. Photogramm. Remote Sens. Spatial Inf. Sci.* XLIII-B3-2020, 1129-1136.
- Kirk, R. L., et al., 2017. COMMUNITY TOOLS FOR CARTOGRAPHIC AND PHOTOGRAMMETRIC PROCESSING OF MARS EXPRESS HRSC IMAGES. *Int. Arch. Photogramm. Remote Sens. Spatial Inf. Sci.* XLII-3/W1, 69-76.
- Kirk, R. L., et al., 2003. High-resolution topomapping of candidate MER landing sites with Mars Orbiter Camera narrow-angle images. *Journal of Geophysical Research: Planets*. 108.
- Kirk, R. L., Howington-Kraus, E., Rosiek, M. R., 2009. Build Your Own Topographic Model: A Photogrammetry Guest Facility for Planetary Researchers. *40th Lunar and Planetary Science Conference*, The Woodlands, Texas.
- Kirk, R. L., et al., 2008. Ultrahigh resolution topographic mapping of Mars with MRO HiRISE stereo images: Meter-scale slopes of candidate Phoenix landing sites. *Journal of Geophysical Research: Planets*. 113, E00A24.
- Kirk, R. L., Soderblom, L. A., Howington-Kraus, E., Archinal, B. A., 2002. USGS high resolution topo-mapping of Mars with Mars Orbiter Camera Narrow-Angle images. *Geospatial Theory, Processing and Applications: ISPRS Commission IV*, Ottawa, Canada.
- Lefort, A., Burr, D. M., Beyer, R. A., Howard, A. D., 2012. Inverted fluvial features in the Aeolis-Zephyria Plana, western Medusae Fossae Formation, Mars: Evidence for post-formation modification. *Journal of Geophysical Research: Planets*. 117.
- Levy, J. S., Goudge, T. A., Head, J. W., Fassett, C. I., 2017. Candidate volcanic and impact-induced ice depressions on Mars. *Icarus*. 285, 185-194.
- Lewis, K. W., Aharonson, O., Grotzinger, J. P., Kirk, R. L., McEwen, A. S., Suer, T.-A., 2008. Quasi-Periodic Bedding in the Sedimentary Rock Record of Mars. *Science*. 322, 1532.
- Malin, M. C., et al., 2007. Context Camera Investigation on board the Mars Reconnaissance Orbiter. *Journal of Geophysical Research: Planets*. 112, E05S04.
- Malin, M. C., et al., 1992. Mars Observer camera. *Journal of Geophysical Research: Planets*. 97, 7699-7718.
- Malin, M. C., Edgett, K. S., 2001. Mars Global Surveyor Mars Orbiter Camera: Interplanetary cruise through primary mission. *Journal of Geophysical Research: Planets*. 106, 23429-23570.
- Mayer, D. P., Kite, E. S., 2016. An Integrated Workflow for Producing Digital Terrain Models of Mars from CTX and HiRISE Stereo Data Using the NASA Ames Stereo Pipeline. *47th Lunar and Planetary Science Conference*, The Woodlands, Texas.
- McEwen, A. S., et al., 2010. The High Resolution Imaging Science Experiment (HiRISE) during MRO's Primary Science Phase (PSP). *Icarus*. 205, 2-37.

- McEwen, A. S., et al., 2007. Mars Reconnaissance Orbiter's High Resolution Imaging Science Experiment (HiRISE). *Journal of Geophysical Research: Planets*. 112, E05S02.
- McEwen, A. S., et al., 2011. Seasonal flows on warm Martian slopes. *Science*. 333, 740-743.
- McEwen, A. S., the HiRISE Science and Operations Team, 2018. The Future of MRO/HiRISE. 49th Lunar and Planetary Science Conference, The Woodlands, Texas, pp. 1301.
- Melosh, H. J., 2011. *Planetary Surface Processes*. Cambridge University Press, Cambridge.
- Miyamoto, H., Komatsu, G., Dohm, J., Hemmi, R., Usui, T., Yamagishi, A., 2016. Geomorphological View of the Environmental History of Mars and Candidate Habitable Environments [in Japanese]. *Journal of Geography (Chigaku Zasshi)*. 125, 171-184.
- Moratto, Z. M., Broxton, M. J., Beyer, R. A., Lundy, M., Husmann, K., 2010. Ames Stereo Pipeline, NASA's open source automated stereogrammetry software. 41st Lunar and Planetary Science Conference, The Woodlands, Texas.
- Neukum, G., Jaumann, R., 2004 HRSC: The High Resolution Stereo Camera of Mars Express. *Mars Express: The Scientific Payload*. ESA, pp. 17-35.
- Neumann, G. A., Rowlands, D. D., Lemoine, F. G., Smith, D. E., Zuber, M. T., 2001. Crossover analysis of Mars Orbiter Laser Altimeter data. *Journal of Geophysical Research: Planets*. 106, 23753-23768.
- Polidori, L., El Hage, M., 2020. Digital Elevation Model Quality Assessment Methods: A Critical Review. *Remote Sensing*. 12, 3522.
- Quantin-Nataf, C., et al., 2018. MarsSI: Martian surface data processing information system. *Planetary and Space Science*. 150, 157-170.
- Ramsley, K. R., Head, J. W., 2013. Mars impact ejecta in the regolith of Phobos: Bulk concentration and distribution. *Planetary and Space Science*. 87, 115-129.
- Robinson, M. S., et al., 2010. Lunar Reconnaissance Orbiter Camera (LROC) Instrument Overview. *Space Science Reviews*. 150, 81-124.
- Scholten, F., et al., 2005. Mars Express HRSC Data Processing – Methods and Operational Aspects. *Photogrammetric Engineering & Remote Sensing*. 71, 1143-1152.
- Schorghofer, N., Levy, J. S., Goudge, T. A., 2019. High-Resolution Thermal Environment of Recurring Slope Lineae in Palikir Crater, Mars, and Its Implications for Volatiles. *Journal of Geophysical Research: Planets*. 124, 2852-2862.
- Slatton, K. C., Carter, W. E., Shrestha, R. L., Dietrich, W., 2007. Airborne Laser Swath Mapping: Achieving the resolution and accuracy required for geosurficial research. *Geophysical Research Letters*. 34.
- Smith, D. E., Zuber, M. T., 1998. The relationship between MOLA northern hemisphere topography and the 6.1-Mbar atmospheric pressure surface of Mars. *Geophysical Research Letters*. 25, 4397-4400.
- Smith, D. E., et al., 2001. Mars Orbiter Laser Altimeter: Experiment summary after the first year of global mapping of Mars. *Journal of Geophysical Research: Planets*. 106, 23689-23722.
- Smith, D. E., et al., 1999. The Global Topography of Mars and Implications for Surface Evolution. *Science*. 284, 1495.
- Stucky de Quay, G., Kite, E. S., Mayer, D. P., 2019. Prolonged Fluvial Activity From Channel-Fan Systems on Mars. *Journal of Geophysical Research: Planets*. 124, 3119-3139.
- Tao, Y., Muller, J.-P., Poole, W., 2016. Automated localisation of Mars rovers using co-registered HiRISE-CTX-HRSC orthorectified images and wide baseline Navcam orthorectified mosaics. *Icarus*. 280, 139-157.
- Tao, Y., et al., 2018. Massive stereo-based DTM production for Mars on cloud computers. *Planetary and Space Science*. 154, 30-58.
- Tarolli, P., 2014. High-resolution topography for understanding Earth surface processes: Opportunities and challenges. *Geomorphology*. 216, 295-312.

- Thomas, N., Stelter, R., Ivanov, A., Bridges, N. T., Herkenhoff, K. E., McEwen, A. S., 2011. Spectral heterogeneity on Phobos and Deimos: HiRISE observations and comparisons to Mars Pathfinder results. *Planetary and Space Science*. 59, 1281-1292.
- Thomas, P. C., 1993. Gravity, Tides, and Topography on Small Satellites and Asteroids: Application to Surface Features of the Martian Satellites. *Icarus*. 105, 326-344.
- Triggs, B., McLauchlan, P. F., Hartley, R. I., Fitzgibbon, A. W., 2000. Bundle Adjustment — A Modern Synthesis. In: B. Triggs, A. Zisserman, R. Szeliski, (Eds.), *Vision Algorithms: Theory and Practice*. Springer Berlin Heidelberg, Berlin, Heidelberg, pp. 298-372.
- Ulaby, F. T., et al., 2014. *Microwave radar and radiometric remote sensing*. University of Michigan Press Ann Arbor.
- Usui, T., et al., 2020. The Importance of Phobos Sample Return for Understanding the Mars-Moon System. *Space Science Reviews*. 216, 49.
- Willner, K., et al., 2010. Phobos control point network, rotation, and shape. *Earth and Planetary Science Letters*. 294, 541-546.
- Willner, K., Shi, X., Oberst, J., 2014. Phobos' shape and topography models. *Planetary and Space Science*. 102, 51-59.
- Wählisch, M., et al., 2014. Phobos and Deimos cartography. *Planetary and Space Science*. 102, 60-73.
- Wählisch, M., et al., 2010. A new topographic image atlas of Phobos. *Earth and Planetary Science Letters*. 294, 547-553.
- Öhman, T., McGovern, P. J., 2014. Circumferential graben and the structural evolution of Alba Mons, Mars. *Icarus*. 233, 114-125.

Appendix

The content of this appendix was peer-reviewed and published as a review article in *Planetary People* (遊星人) by the Japanese Society for Planetary Sciences (JSPS) (日本惑星科学会) in 2018, and its copyright is held by the JSPS. The JSPS allows the use of the paper in the author's dissertation, and its published version can be deposited in the author's institutional repository.

Article information:

Hemmi, R., Miyamoto, H., Parsons, R., 2018. Geological activities on present-day Mars and implications for future Mars missions (地形変化から見る現在の火星の地質現象と将来の火星探査の展望). *Planetary People - The Japanese Society for Planetary Sciences* (日本惑星科学会誌遊星人). 27(3), 152-162, DOI: 10.14909/yuseijin.27.3_152.

特集「火星圏のサイエンス」

地形変化から見る現在の火星の地質現象と
将来の火星探査の展望逸見 良道¹, 宮本 英昭^{1,2}, Reid Parsons¹

2018年6月29日受領, 査読を経て2018年7月31日受理.

(要旨) 火星の表面進化史の理解に重要となる地質区分のうち、アマゾニアンは約30億年前から現在までに相当する。しかし、現在の地質現象はアマゾニアンに分類されない地域でも活発に起こっている。現在の火星の活動度を理解するには、まずこうした個々の現象の詳細を理解することが重要である。そこで本稿では、火星周回機によって近年観測された現在の表面変化を概観する。さらに現在の帯水層やメタンの放出に関与する可能性がある地形的特徴を検討し今後の火星探査ミッションの展望を概観する。

1. これまでの火星の地質学

バイキング計画以降の火星周回機が、火星表面全体について1画素あたり数十～数百mのリモートセンシングデータを得たことで、全球的な地質マッピングが可能になった。火星表面はクレーター年代学と層序関係に基づき地域ごとに表面更新の時系列が整理され、古い順にノアキアン(Noachian)、ヘスペリアン(Hesperian)、アマゾニアン(Amazonian)と分類された(e.g.[1])。特にクレーター年代学に関しては、各地質ユニットの表面に残された直径16 km, 5 km, 2, 1, 0.5 kmでのクレーター数密度の累積サイズ頻度分布とクレーター年代関数との比較[2]から、ノアキアン-ヘスペリアン境界は約37億年前、ヘスペリアン-アマゾニアン境界は約33-29億年前に相当すると考えられている。

ノアキアンでは、温暖湿潤な気候による表層水・地下水と活発な火山活動・熱水活動の環境条件の下、天体衝突による巨大盆地、巨大火山帯であるターシス山群(Tharsis Montes)やオリンポス山(Olympus Mons)一帯の大部分、バレーネットワークが生じた。ノアキアンに形成した表面の大部分は現在の南部高地に残されている。

ヘスペリアンでも引き続き火山活動と表層水の影響が大きく、大規模な溶岩平原、アウトフローチャネル、峡谷が形成した。北部低地の大部分と南部高地の一部の火山地域と衝突盆地の底がヘスペリアンに対応する。

こうした時代に対し、アマゾニアンでは火山活動は火山地帯の局所的な地域に限られ、テクトニクスや天体衝突の頻度、表層水の活動度は時間とともに著しく低下し、地形変化の規模は極めて小さくなったと考えられた。

図1に米国地質調査所(USGS)が作成した最新の地質図[2]のうち、アマゾニアンとして分類された地域を示した。特に最も新しいアマゾニアン後期(約3億年前～現在)に分類される地域は、南北極冠のみである。

その一方で、高い時間分解能・空間分解能をもつ近年の火星周回機の観測データの増大に伴い、現在の火星表面で生じる多様な地質現象の詳細が明らかになりつつある。アマゾニアンは定義の上では現在を含む一方で、現在の地質現象の観測地点を地図上にプロットすると、アマゾニアンに分類された地域とは必ずしも一致しない(図1)。これは、数kmに満たない範囲で発生する地形変化が、地質区分に用いられる直径数km以上のクレーター数に影響を与えないことに起因しており、これまで使用されてきた地質区分が「表面年代」ではなく、どちらかという地殻あるいは上部地殻の形成年代に相当することを表している。

このような背景を考慮すると、現在の地質現象を理

1. 東京大学総合研究博物館

2. 東京大学大学院工学系研究科
hemmi@seed.um.u-tokyo.ac.jp

解するには従来の巨視的な表層進化史とは異なる時間軸や空間スケールでの見方を必要とする。また、現在でも活動度の高い領域は、将来の火星探査ミッションにおいても重要度の高い探査対象となる。

そこで本稿では、現在の火星表面の地質現象の詳細(地形的特徴、発生地域、生成プロセスなど)を概説し、アマゾニアン以前には無視できるほど小規模だった地質現象が現在の表面では地形変化の主因であることを明らかにする。

次に、近年観測された季節変動する大気メタンがどのようなプロセスを経て発生しているのか、また帯水層がどのような形で地下に現存するかというテーマに対して、特定の地形や現在の表面変化との関係性について筆者らが行った予備的研究の結果を踏まえながら検討する。

最後に、今後の火星探査計画ではどのような地質現象の観測が期待されるか概説する。なお、ダスト・デビルと呼ばれる塵旋風が通過した跡や、表面ダスト粒子が風で飛ばされて生じるウィンド・ストリークのような表面変化は、地下深部との相互作用や地形変化への寄与が比較的乏しいため本稿では扱わない。

2. 大規模な表面変化

規模という点で現在の表面変化で突出するのは、アマゾニアン後期の地域に分類された、季節により変化する南極冠表面と砂丘地帯である。

2.1 南極冠

火星の南極冠は下位から順に、 H_2O 氷とダストを主体とする層状堆積物(直径約1000 km、厚さ数km)、 CO_2 氷に覆われた(その下は H_2O 氷)残留極冠(幅約400 km、厚さ5-10 m)で構成される。さらに南極冠は毎年冬に CO_2 の霜でできた季節性極冠(最大直径約5000 km、厚さ数m以下)に覆われる[3]。

季節性極冠は、 CO_2 の昇華によって、南半球の秋から春にかけて南極冠の表面に生じ、夏季になると後退(消失)する(消失しきらなかった部分が残留極冠となる)という現象を1火星年ごとに繰り返す。そのため、残留極冠や季節性極冠の表面では、不規則形状の地形的変化が観察される。

残留極冠に生じる虫食い状の凹地(その形態から「ス

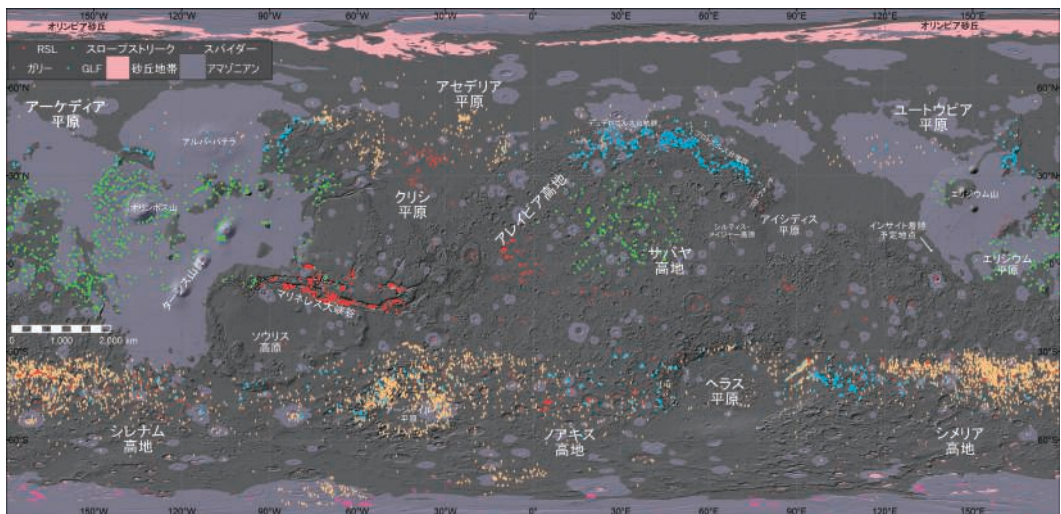


図1：現在生じている地質現象の観測された地点およびアマゾニアンに分類された地域と代表的な地名¹。背景画像は火星全球のマーズ・グローバル・サーベイヤーのレーザ高度計MOLAの標高図に基づく陰影起伏図。カラーの図は電子版を参照されたい。Courtesy USGS Astrogeology Science Center, <http://astrogeology.usgs.gov>

注1：筆者らは昨年度、大学院講義にてIAU Gazetteer of Planetary Nomenclatureに掲載されている火星の各地名に対応する日本語表記の一覧を独自に作成した。本稿の本文中・図中ではそれらを使用して記載している。なお、各地形(Feature Types)は元来の定義や代表的な産状を反映させるため、Chasmaは「大峡谷」、Mensaeは「台地群」、Mons (Montes)は「山(山群)」、Planitiaは「平原」、Planumは「高原」、Terraは「高地」、Vallesは「大峡谷」と訳した。固有名詞については、欧米の出身者が大半を占める火星研究者コミュニティの間で最も頻繁に発話される発音に近い形でカタカナ表記した。

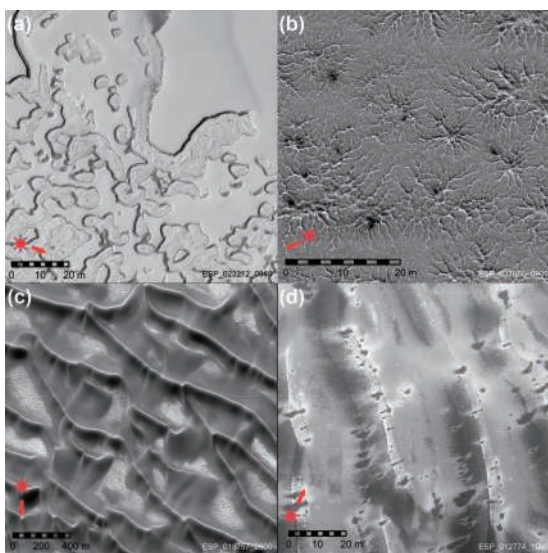


図2：大規模に変化する表面を撮像したHiRISE画像。

(a) 一部昇華した南極冠(0.94° W, 85.84° S), (b) スパイダー (127.42° E, 87.01° S), (c) オリンピア砂丘(116.03° E, 79.94° N), (d) ダーク・デューン・スポット(179.32° E, 71.97° S). 画像提供: NASA/JPL/University of Arizona.

イス・チーズ」(Swiss cheese)とも表現される)が時間とともに個々の窪地が広がり互いにつながってゆく(図2a)[4]. これは昇華に伴う体積の減少で説明される。

季節性極冠の表面に生じる特徴として、樹枝状の亀裂からの暗い物質の放出現象である「スパイダー」(蜘蛛状の形状から英語ではspiderあるいはaraneiformと表現する)も知られる(図2b) [5]. 図1にスパイダーの最新の分布データを示した[6]. これは透明な氷の層を透過した太陽光が地下のCO₂氷を昇華し圧力上昇を経て上面を突破してジェットとして噴出する現象によって生じたと解釈される。いずれにしても、極冠は地形変化が数千kmの範囲で見られるものの、せいぜい深さ数mでドライアイスが太陽光輻射を受けて相変化することで生じている現象と考えられている。

2.2 砂丘地帯

火星には大小さまざまな規模の砂丘が存在するが、ここではUSGSの火星全球砂丘データベース[6]に基づき、個々の砂丘が集まり砂丘地帯となった面積1 km²以上の大規模な砂丘地帯(図1)を紹介する。砂丘地帯の分布は、北極冠の周囲に発達するものが目立つが、高緯度域から赤道域においても、局所的に衝突盆

地やカルデラの底といった地形的に周囲より低い地域に点在する傾向がある。地球上で見られる砂漠の見かけと類似した形状(バルハン、星型、長細いもの等を含む)を持つ。構成粒子は石英粒子でなく玄武岩質の母岩が風化した暗色の粒子と考えられている。

砂丘地帯は全体が移動しており、例えばニリ・パテラ(Nili Patera; シルティス・メイジャー高原の火山カルデラ)の底に分布する砂丘一帯の移動速度から推測される砂のフラックスは、地球上の南極ビクトリア谷の砂丘地帯と同程度である[7]. これは大気圧がわずか4.0-8.7 hPa(地球大気の約150分の1)とはいえ、大気と表面の相互作用が活発なことを示しており、ダスト・ストームやダスト・デビルといった全球的に生じるダスト粒子の頻繁な巻き上げ現象からも推察できる。ただし、火星表面でもダストの被覆量が多い地域と砂丘地帯は必ずしも一致しない。

北極冠を取り囲むように分布する砂丘地帯はオリンピア砂丘(Olympia Undae; 図2c)と呼ばれ、分光観測から石こう(gypsum)が検出された[9]. 北極冠あるいは基盤岩から流れ出した硫酸を含む融水が表面水あるいは地下水としてこの地域に流入・沈殿し、西向き(時計回り)の卓越風により風食し風下方向に向かって濃度が減少するように堆積したと考えられている。しかし、現在までこの一帯にだけ砂丘が留まり続けている理由はわかっていない。

緯度60度以上の高緯度域の砂丘では、代表的な表面変化としてダーク・デューン・スポット(dark dune spot)が見られる(図2d). 秋から冬にかけて砂丘全体がCO₂の霜(季節性極冠)に覆われ白くなるが、これが春になり昇華すると幅数m～数十mの暗い斑点模様が砂丘の峰や谷に発生する。これは、先述のスパイダーと同様のプロセスで形成されたと考えられている。砂丘の斜面では粒子流を引き起こし後述のデューン・ガリーに類似する地形を形成する[10].

3. 斜面上での変化

火星の表面には衝突クレーターや火山、丘、風成地形、谷などが存在し、それにともない大小さまざまな斜面が無数に存在する。そうした斜面上では、火星周回機が取得した高解像度画像から現在も新たに生じている表面変化が確認されている。ここでは特によく知

られたスロープ・ストリーク、RSL、ガリーの特徴を詳説する。

3.1 スロープ・ストリーク

スロープ・ストリークあるいはダーク・スロープ・ストリーク((dark) slope streak)は、幅数十m～数百m、長さ数百m～数十kmに及ぶ、周囲よりも暗い筋状の特徴である(図3a) [11]。同様の形状で周囲より明るいものも一部存在し、ブライツ・スロープ・ストリーク(bright slope streak)と区別することもある。バイキング探査機の観測によりその存在は知られていたものの、現在も発生していることはマーズ・グローバル・サーバイヤー探査機の高解像度カメラMOCによる観測で判明した。

斜面上の微地形の影響を受けて屈曲・分岐・合流しながら、重力方向に流れ下る形状を持ち、発生地点は数m以内に収まるほど極端に小さい。発生以降は形状を変えないが、時間の経過とともに暗い色が薄まり周囲の色に近づく。

形成プロセスとして現在有力視される乾燥粒子流モデル(dry granular flow)では、一定量以上に堆積したダストが表層数m以内の層理面で閾値を超えてダストなだれ(dust avalanche)として流れ去り、地下の新鮮な暗い面を露出するマス・ムーブメントと考えられた。

一方で、高々数度の傾斜角しかない斜面でも生じるスロープ・ストリークを粒子流のみで説明するのは困難であるため[12]、液体の水が関与する可能性も排除できない。そこで提案された「湿った」流体モデルのうち代表的なものでは、斜面表層下の塩化物(水和塩)により大気中の水分が融解して塩水となり、斜面を不安定化させて流動を引き起こすと解釈された[13]。

類似の現象は地球の南極大陸で観測されている。スロープ・ストリークの全球的な分布[14](図1)については、ダストの被覆量が多いターシス(Tharsis)地域やエリジウム(Elysium)地域、アレイピア高地(Arabia Terra)に集中する一方で、こうした地域は水蒸気圧の高い地域ともよく一致するため[15]、どちらの仮説(あるいは両方の組み合わせによる可能性)もいまだに有力である。

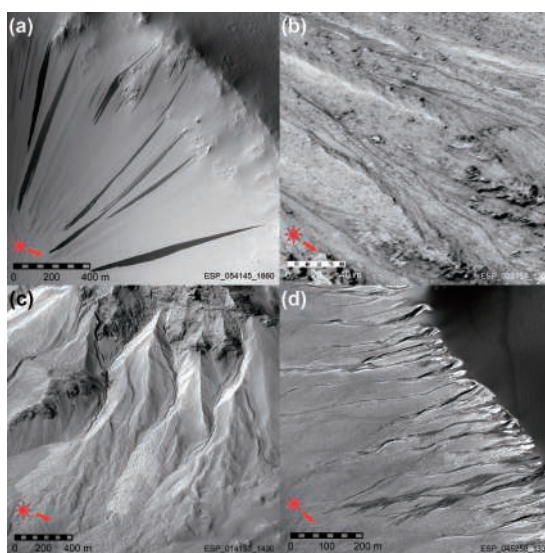


図3：斜面上の変化を撮像したHiRISE画像。(a)スロープ・ストリーク(17.96°E, 5.8°S), (b)RSL(9.54°E, 45.95°S), (c)ガリー(37.27°W, 36.49°S), (d)デューン・ガリー(20.13°E, 46.73°S)。画像提供：NASA/JPL/University of Arizona。

3.2 RSL

Recurring Slope Lineae(RSL)は、斜面上で季節ごとに変化する、線状に暗くなる特徴(幅数m、長さ数百m程度)である(図3b)。最高解像度25 cm/pixelのマーズ・リコネッサンス・オービター(MRO)のHiRISEカメラで撮像された複数の高解像度写真を比較することによって初めて発見された[16]。

春から夏にかけて長さが時間とともに斜面下方向に徐々に伸びるように成長し、秋から冬にかけては逆に徐々に後退してゆく(先端側から消失する)というパターンを毎火星年に同一地点で繰り返す。スロープ・ストリークと異なり、1火星年の間に形状を変えるだけでなく、個々の線状の地形が分岐や合流を繰り返す特徴が見られる。

2火星年以上の複数回の観測によって、長さの漸増、同一地点での複数年の発生、冬季の消失という3つの条件を満たすものは、特にコンファームドRSL(confirmed RSL)として判別され、これまでに南部高地の南緯30-60度の範囲、赤道域のマリネレス大峡谷(Valles Marineris)やアレイピア平原(Arabia Terra)、北部低地のアセデリア平原(Acidalia Planitia)に位置

する、衝突クレーターの内壁や中央丘、および谷をなす側面の崖や底面の残丘において確認された[17]. 図1に示したのは、これまでに報告された(コンファームド) RSLおよびRSLの条件を1つでも満たす類似の地形が発見された地点である.

高解像度の分光観測によるRSL発生箇所で水和塩(特に過塩素酸塩・塩素酸塩・塩化物の水和物)が発見され[18], 凝固点効果により一時的に液体になった塩水が斜面を流れ下ったと解釈された.

さらに、火星大気圧下で水氷から融解した水を砂でできた傾斜面に浸透させる室内実験では、沸騰した水が表面の砂粒子を吹き飛ばしながら前進する現象が確認された[19]. 水和塩の潮解によって土壌の反射率の低さを再現した実験結果[20]とともに、液体の水の影響が有力視されている.

その一方、高解像度数値標高モデルの解析からRSL末端部の勾配が乾燥した粒子流によってできた安息角と調和的という研究が昨年発表された[21].

一部の地域のRSLについてはTHEMIS表面温度データの解析結果が水の関与が非常に小さいことを示しており[22], 完全に乾燥した環境での形成も排除しきれない. また、発見地域の地質学的産状が大きく異なるためRSLの生成プロセスが地域ごとに異なる可能性すらある.

3.3 ガリー

ガリーは、幅数m~数百m、長さ100 m~数km、深さ数十m未満の削剥された小規模な谷地形である(図3c). ガリーは次の3つの要素で構成される[23]. (1)削剥の起点となった崖上部でシャープな輪郭を持つ峰に挟まれた「アルコーヴ」(alcove), (2)削剥された物質を運搬する「チャンネル」(channel), (3)崖下部に運搬された物質が堆積し緩斜面になった「エプロン」(apron). エプロンの形状からガリーの大半は単独のイベントではなく多数の堆積イベントによって現在みられる地形を形成したと考えられる. 高解像度カメラ画像の比較から、特にエプロン部において明るい物質が現在も近年新たに堆積する様子が報告されている.

図1に示すように、ガリーの多くは南北両半球の緯度30-60度の範囲に位置するクレーター内の壁面や中央丘に見られ、南半球の方が北半球に比べて発見数が多く、緯度が高くなるにつれて赤道向きに流下するガ

リーが増加する傾向にある[24].

これまで南半球では南緯30度よりも高緯度域で小規模な表面ラフネスが減少し、これは厚さ数メートルの水氷主体の堆積物で高緯度域が覆われることが原因と考えられてきたが[25], これはガリーの数が南緯30度から増加する傾向とも調和的である.

地球のガリーと同様に火星表面でも液体の水が関与した土石流として、特に地下水(塩水を含む)の帯水層からの湧水、地軸傾斜角が大きい時期の雪解け水や地下水の融解が起源に挙げられたが、現在の気候条件では液体の水が持続的に存在することは難しい. そこで風成堆積物の乾燥粒子流や液体のCO₂に駆動される流れ等の水の関与しない説も提唱されてきた.

高い時間・空間分解能のリモートセンシングデータが充実してきた昨今、ガリーのチャンネル内にCO₂の霜が発生する様子が観測された. 熱力学に基づく数値計算から冬季に大気中から凝縮されるCO₂氷がレゴリスの表面を覆うだけでなくレゴリス内の間隙を満たし、昇華する際にCO₂ガスと土壌が混合して土石流が生じるという説も提案された[26].

上記とは異なる特徴を持つガリーとして分類されたのが、砂丘の峰から風下斜面に分布するもので[27], 特にデューン・ガリー(dune gully)と呼ばれる(図3d). デューン・ガリーは幅数m程度で小規模なアルコーヴに対して、リムを持ったチャンネルが数百m~数kmと直線状あるいは屈曲を繰り返しながら延びる[28]. 末端部では明瞭なエプロンを持たない代わりに、ガリー先端から数mほど離れた地点に数m大の複数の穴(ターミナルピット; terminal pitと呼ばれる)を伴うことが多い.

通常のガリーと同様に土壌中のCO₂昇華により土石流が生じると考えられた. 低温低圧環境の下で砂で覆われた表面にドライアイスを設置する近年の実験では、ドライアイスが土壌内にもぐり込み、昇華に伴いリムを持つチャンネル状の構造ができるだけでなくターミナルピットに類似する穴を生じる現象が確認されている[29]. そのため、ドライアイスの関与が有力視されるが、実スケールで砂丘内部で数百m大のガリーと数m大のターミナルピットが生じうるのは、詳細な形成過程は今のところわかっていない.

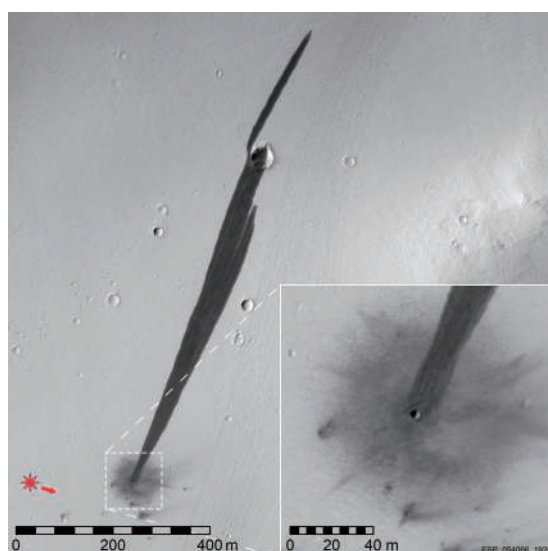


図4：衝突クレーター（拡大図）によって新たに生じたスロープ・ストリークを撮像したHiRISE画像(14.77° E, 11.81° N). 画像提供：NASA/JPL/University of Arizona.

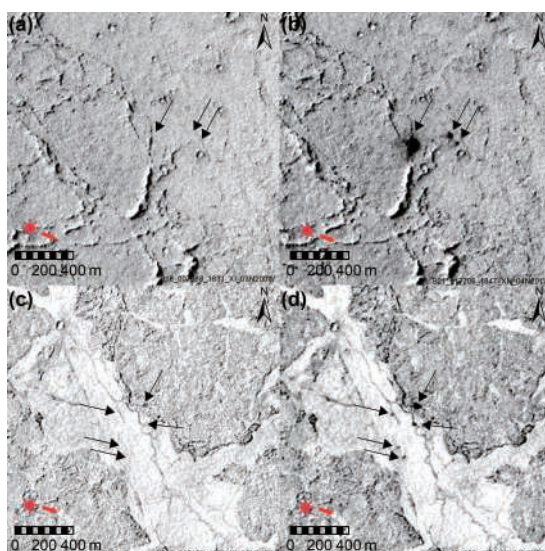


図5：エリジウム平原 (Elysium Planitia) にてリッジに沿って新しく生じた暗い斑点(矢印の地点)。aとb(158.94° E, 4.44° N), cとd(149.56° E, 5.23° N) がそれぞれ同じ場所での形成前後のCTX画像。画像提供：NASA/JPL-Caltech/MSSS.

4. 地下物質の放出

天体衝突は小規模ながら現在の火星表面で生じており、衝突によって生じるクレーターや放出物、衝突がもたらす衝撃や熱に誘発する地質現象(例:衝突によるスロープ・ストリークの発生; 図4)は現在の表面を変化させる[30].

現在の衝突クレーターは直径数m程度であったとしても放出物は直径数十～数百mの範囲に広がるため、MRO CTXカメラ画像(5～6 m/pixel)では大きさ数ピクセル以上の暗い斑点模様として観測できる。2006年から2012年までに同一地点を複数回観測したCTX画像を比較することで現在の衝突頻度が $1.65 \times 10^{-6}/\text{km}^2/\text{yr}$ と推定された[31]。これは理論計算に基づく衝突フラックスの値($10^{-8} - 10^{-6}/\text{km}^2/\text{yr}$) [32]と調和的であった。

しかし、筆者らは衝突以外の現象(たとえば揮発性物質の放出)によっても表面に同様の暗い模様が生じうるといふ仮説を立て[33]、のべ3万人以上の市民と20名以上のボランティア、4名の研究者の協力のもと、2017年までに撮像されたCTX画像を使用し、計3,549

組の画像ペアの解析を行った。

北半球の低緯度領域(総面積 $1.0 \times 10^7 \text{ km}^2$; 火星全体の7.06 %に相当)について調査し、計477個の新たに生じた暗い点を判別した。そこから推定した生成率は $1.3 \times 10^{-5}/\text{km}^2/\text{yr}$ で、過去の推定値よりも1桁大きい値が得られた。

過去の推定よりも調査面積が1桁小さく、画像の撮像期間や対象地域の違いから先行研究と単純に比較することは難しいが、過去の推定よりも多くの衝突が少なくともある領域では生じているという解釈が成り立つデータが得られた。

その一方で、天体衝突とは全く異なり、こうした現象のいくつかは火星の地下の活動度に起因する可能性も捨てきれない。具体的には、現在でも温度勾配が局所的に高い領域が存在することで、地下の氷や揮発性物質が短期間に表面に噴出し同様の陥没地形や放出物を形成するというものだ。言い換えれば低緯度域でもスパイダーやダーク・デューン・スポットと同様の現象が起きうるともいえる。

予察的な画像解析ではリッジのような構造地形に沿って生じているものも見つかった(図5)。引き続き対象領域・観測期間を広げ、より正確な統計データを得

るとともに、高解像度画像を用いた詳細な解析により衝突クレーター以外の成因がありえないか、今後慎重に検討する必要がある。

5. 地下に帯水層は現存するか？

前節までで、現在の火星表面の地質現象が理解されつつあり、液体の水の関与の可能性は排除されていないことを示した。本節では過去の水(氷)の挙動がどうに考えられてきたのか、現在の地下や表面の地形とどう関連しうるのかを整理する。

現在火星表面に露出する水氷の大部分は極冠として存在する。Cliffordは地殻表層が氷で飽和状態にあるのに対して、深部では氷が地熱によって溶融し帯水層として全球水循環に関わると提唱した[34]。地下水が赤道域に向かって流動し、赤道域では上昇して一部が表面に現れ気化して大気中へ移動し最終的には極冠として固定されるという説である。

マーズ・エクスプレスの地中レーダー MARSIS(周波数帯は1.3-2.3 MHz, 2.5-3.5 MHz, 3.5-4.5 MHz, 4.5-5.5 MHzの4バンド、自由空間での深さ方向の分解能は約150 m、地上でのフットプリントの大きさはアクロストラック方向に10-20 km、アロングトラック方向に5-10 km)は、2017年まで地下深部に帯水層の反射面を検出できていなかった。

これは少なくとも地下400 mの範囲には地下水面が存在しない可能性、あるいは存在する場合でも空間分解能以下のサイズである可能性を示す一方、深さ約300m以深でシグナルが減衰している可能性があり、より深部での地下水面の存在は否定できないと考えられてきた[35]。

そして、2018年7月、MARSIS観測データの解析によって、南極冠(193° E, 81° S)の層状堆積物(深さ1.5 km)の直下に周囲よりも極めて明るい反射面(幅20 km)が存在し、液体の水と調和的である(比誘電率 >15)と初めて報告された[36]。今後別の地域についても同様の報告が続く可能性がある。

数値モデルからは、火星の地殻熱流量に関して約44億年前の $60-70 \text{ mW/m}^2$ から現在の $10-20 \text{ mW/m}^2$ に減少したと考えられる[37]。しかしより最近の研究では、地殻の厚さの変動とマントルの熱フラックスの変動によって現在の熱フラックスには地域差が生じ

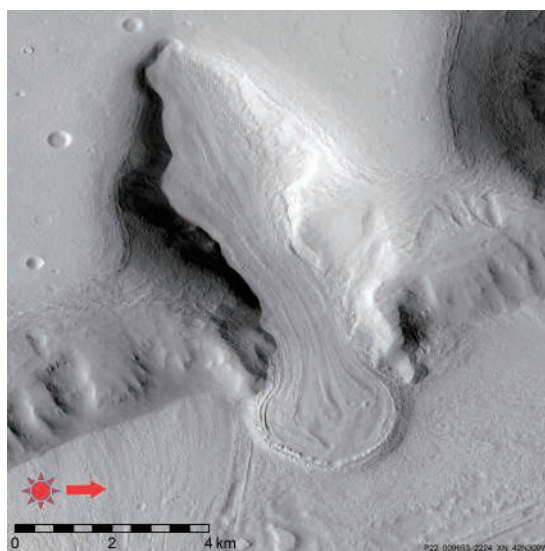


図6：プロトニルス台地群(Protonilus Mensae)にみられる典型的なGLFのCTX画像(50.53° E, 42.23° N)。画像提供：NASA/JPL-Caltech/MSSS。

るとも言われる[38]。こうした地域的な変動は火星レゴリス、特に低い透気係数で断熱材の役割を果たす未固結のダスト堆積物で覆われた地域では、永久凍土が溶融する深さを推定するのに重要といえよう。

最近両半球の高緯度域(約55度付近)の露頭に、氷水が大量に含まれる画像をHiRISEカメラが撮像したと報告された[39]。これは大量の水が火星の地下に貯留している可能性を示唆し、これが地下深部において溶融したり、地軸傾斜角が現在と異なる時期に溶融することで地形変化を引き起こす可能性がある。

中緯度域では、地下水の厚い堆積物(厚さ $\sim 700\text{m}$)が薄いレゴリス層(厚さ10m未満)に覆われてできた、過去の氷河流動の痕跡とされる地形が多数みられる。Viscous Flow Feature(VFF), Lobate Debris Aprons(LDA), Lineated Valley Fill(LVF)などと分類されたが、ここでは[40]にならい総称してGLF(Glacier-like Forms)とする(図6)。

図1にGLFの分布[40]を示すと、北半球ではデューロニルス台地群(Deuteronilus Mensae)、プロトニルス台地群(Protonilus Mensae)、南半球ではヘラス平原(Hellas Planitia)の東側に集中して見られた。70年代のバイキング探査機画像からLDAは氷水でできたと考えられ、MROのレーダーサウンダーSHARADによる観測では、最大のLDAがほぼ純粋な氷ででき

ているとわかったが[41]、水の純度や厚さについては不明である。

現在の気候条件下で水が不安定であるため、過去に地軸傾斜角の変化によって大量の水が極域から中緯度域に再配置されたと考えられている。この氷堆積物表面のクレーター数密度から、水の再堆積が起こったのはアマゾニアンの後半ごろ(約3億年前)と考えられるが、この堆積物が周期的に生じた可能性もある。

降雪の量や時期に制約を与えるため、水の蓄積と流れに関する数値シミュレーションがGLFに適用されたが[42]、統一的な結果は得られておらず、降雪量や岩屑物の変位量が地域的に変動するせいで、ごく限られた地域のみから地軸の変動史を制約するのは困難である。

以上のように、現在火星の地下に帯水層が存在するか否かは多角的な面から検討され、最新の観測データやモデル計算から少なくとも地下水の存在を否定する結果は出ていない。特に中緯度から高緯度域に見つかった地下水が溶融することで生じた地形は、地下水の供給源と関連が深い可能性がある。

6. メタンの放出源はどこなのか？

前節では地下の液体の水や氷の挙動が現在も表面地形の変化に影響を及ぼす可能性を述べた。本節では、揮発性物質の放出などの形で現在の地形変化に寄与する可能性がある揮発性物質の中でも特に重要視される大気メタンについて筆者らの予察的観察とともにこれまでの研究を概説する。

メタンは現在の火星大気中では比較的短命と考えられていて、供給されることがなければせいぜい約300年、場合によってはわずか200日間から数時間で分解されるといわれている[43]。

これまで火星大気中のメタンの検出は複数の火星周回機・探査車の機器を用いた観測および地上観測により報告された。特にキュリオシティ探査車は試料分析装置SAM (Sample Analysis at Mars)を用いてメタンのその場観測を行い、2015年の約1か月間に~7.2 ppbv [44](2014年3月から2017年5月のバックグラウンドレベルが平均して0.41 ppbv [45])という、短期間のメタン濃度の急上昇が観測された。

これは単にメタンの大気中への急速な放出を示唆す

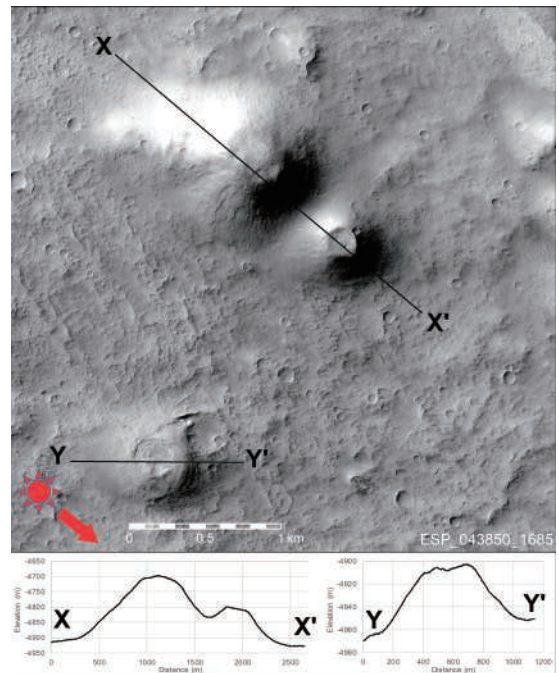


図7：メラス大峽谷(Melas Chasma)の丘状の地形(69.41° W, 11.52° S)のHiRISE画像と対応する数値地形モデルから抽出した2次元地形断面。頂上のくぼ地、直径約500–1000 m、高さ約50–150 mという特徴は地球の泥火山と調和的である。画像提供：NASA/JPL/University of Arizona。

るだけでなく、メタンの貯留や分解についてまだ知られていないプロセスが存在する可能性がある。あるいは濃度が急上昇した期間に、メタンの噴出がキュリオシティ探査車の近傍で連続して起こったことで噴出が停止して拡散する前に検出できたのかもしれない。

全球的にはMummaらの2003年のメタン濃度の観測[46]では、夏に最大45 ppbv程度のメタンの濃集域が赤道付近で検出された。これはサバヤ高地(Terra Sabaea)、ニリ・フォッサ(Nili Fossae)、シルティス・メイジャー高原(Syrtis Major Planum)の各地域にメタン源が存在する可能性を示唆している。しかし、こうした地上観測のデータに対しては地球大気のメタンの吸収が影響するとも反論されている[47]。

メタンの発生プロセスとしては有機物の紫外線による分解や岩石の熱水変成が考えられるが、生じたメタンはクラスレート(メタンハイドレート)として地下の永久凍土層に貯留し、ここから現在もメタンが表面へと漏れ出ている可能性がある。しかし、メタンが火星地殻中のメタン生成菌によって生じた可能性も排除で

きない。

メタン放出に伴う地形的特徴の探索も続いているが、今のところ決定的なものではなく、いくつかメタンガスの抜け穴(地球上ではmacroseepageやmicroseepageと呼ばれる)に類似する特徴が報告されている[43]。

また地球上のメタンガスの放出源として知られる泥火山(地下深部の細粒物質・液体の水・ガスの混合流体が過剰圧力を受けて噴出し堆積してできる山体)に類似する直径数十m～数kmの山体が火星の各地で多数報告されてきた[48]。

もしこうした地形からメタン放出に伴い形成されたとすると、その地下に貯留したメタンが今も地下から地上の噴出口へ直結する経路を通して放出を続けている可能性すらあるため[49]、地下深部の物質のサンプリングの容易さも考慮すると、将来の重要な探査対象になる。

実際、筆者らは将来の探査候補地点として、マリネレス大峡谷(Valles Marineris)内側のメラス大峡谷(Melas Chasma)東部を提案してきた[33]。メラス大峡谷では、RSL、泥火山状の丘(図7)、地すべり堆積物、水和した硫酸塩鉱物が全て観測できるため、各地形が相互にどのように関係するのかについて、より詳細な調査を現在進めている。

7. 火星探査の展望とまとめ

ここまでで列挙した現在の表面変化が地下物質の相変化や移動を反映している可能性を示唆している。現在活動中の火星探査機と将来の火星探査機は、こうした地質現象に対して、高い分解能(時間・空間・波長)で周回軌道上から観測したり、対象地形に接近しその場観測を行う絶好の機会を迎える。

2012年8月にゲール・クレーター(Gale crater)に着陸したキュリオシティは、現在クレーター中央丘の斜面を登りながら南下しているが、その予定進路にはHiRISE画像の観測からRSLが報告されている[50]。これまで探査車や着陸機によるRSLのその場観測の例はないため、RSLに接近し高解像度の画像やレーザー光を照射する化学分析カメラなどでの観測により液体の水の関与について制約を与えるような結果が期待される。

2016年10月に火星に到着したエクソマーズ計画の

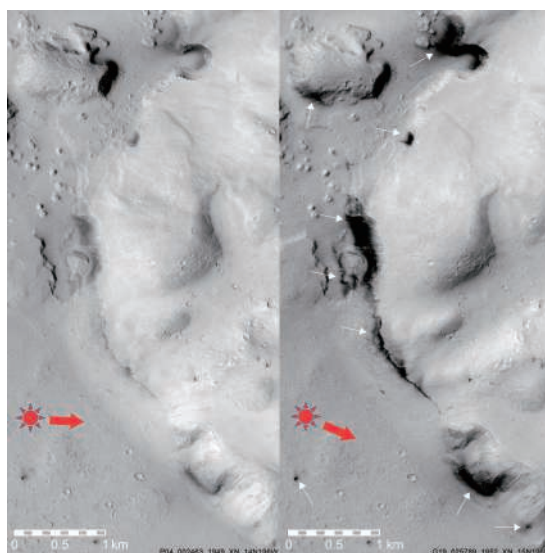


図8：エリジウム平原(Elysium Planitia)の斜面に近年生じた暗い表面(矢印の地点)のCTX画像(163.17° E, 14.85° N)。左が変化前、右が変化後。画像提供：NASA/JPL-Caltech/MSSS。

火星周回機トレース・ガス・オービター(TGO)は、軌道の調整期間を経て2018年5月から本格的に観測を開始した。TGOによってメタン放出イベントの時間・場所・濃度を高い分解能で観測できる。これにより火星表面のメタン放出の発生源や発生プロセスをより制約できると期待される。

また、2018年5月に打ち上げられた火星着陸機インサイトは2018年11月末にエリジウム平原(Elysium Planitia)に着陸し(図1)、内部構造や地殻熱流量、火震を計測する予定である。筆者らの予備的な観測では、エリジウム平原に存在する斜面上にて、近年アルベドが極端に低くなる現象がCTX画像の比較により確認された(図8)。

こうした特徴は一般的には砂丘を構成する暗い粒子の堆積として認識されてきた。しかし、なぜ周辺域一帯にではなく斜面上にのみ集中するのか説明がつかない。近傍には過去のスコリア丘あるいはルートレス・コーン(溶岩流と水の接触による爆発で生じる小丘)と類似する地形も観察できたため、局所的な温度勾配による液体の水の滲出と解釈することも可能である。インサイトによってこうした地質活動が観測されることが期待される。

また、筆者らはアレイビア平原でも同様の現象を確

認しているため、このような地形変化が全球規模でどのような地域に分布するのか、また他の地形変化とどう関連するのか、あるいは単なる表面ラフネスの変化で説明可能かを今後の研究課題として検討している。

最後に、現在の地質現象の発生日点を特定するには、周回機によって2回以上(可能であれば複数年にわたり複数の季節で)同じ地点を観測するデータが必要である。加えて数十mスケールの地形解析においては高い空間解像度をもつ画像や高解像度ステレオペア画像に基づく超高解像度(1画素あたり最高で1 m)の数値標高モデルが必要である[51]。

そのうえ、こうした地形変化の判別には、画像解析・惑星地質学・野外調査のエキスパートによる肉眼での徹底的な観察が欠かせない[52]。実際、RSLが報告されたのはHiRISEカメラの観測が開始されてから約5年が経過した時期であった。

今後こうした研究を続けていくことで、火星表面および地下環境についてより正確な地形変化の記載が可能になり、表面と大気および地下物質の相互作用や流動に関する理論モデルが進展し、Mars 2020をはじめとする将来の着陸探査計画に対して有望な着陸候補地が提案されると期待できそうだ。

謝 辞

ゲストエディターの玄田英典博士からは、本稿を執筆する機会と原稿への助言・コメントを頂きました。査読者の小川佳子博士からは、有益なコメントを頂きました。本稿の改訂を助けて頂いたことを深く感謝いたします。本研究は科研費16K13890、17H02953と株式会社東京ドーム／宇宙ミュージアムTeNQの支援を得ています。

参考文献

- [1] 後藤和久, 小松吾郎, 2012, 地質学雑誌 118, 618.
- [2] Tanaka, K. L. et al., 2014, USGS Sci. Inv. Map 3292.
- [3] Byrne, S., 2009, Annu. Rev. Earth Planet. Sci. 37, 535.
- [4] Thomas, P. C. et al., 2000, Nature 404, 161.
- [5] Kieffer, H. H. et al., 2006, Nature 442, 793.
- [6] Schwamb, M. E. et al., 2018, Icarus 308, 148.
- [7] The Mars Global Digital Dune Database (MGD³), <https://astrogeology.usgs.gov/geology/mars-dunes/the-mars-global-digital-dune-database>
- [8] Bridges, N. T. et al., 2012, Nature 485, 339.
- [9] Langevin, Y. et al., 2005, Science 307, 1584.
- [10] Hansen, C. J. et al., 2011, Science 331, 575.
- [11] Sullivan, R. et al., 2001, J. Geophys. Res. 106, 23607.
- [12] Miyamoto, H. et al., 2004, J. Geophys. Res. 109, E06008.
- [13] Kreslavsky, M. A. and Head, J. W., 2009, Icarus 201, 517.
- [14] Schorghofer, N., 2007, Icarus 191, 132.
- [15] Bhardwaj, A. et al., 2017, Sci. Rep. 7, 7074.
- [16] McEwen, A. S. et al., 2011, Science 333, 740.
- [17] Stillman, D. E. et al., 2017, Icarus 285, 195.
- [18] Ojha, L. et al., 2015, Nat. Geosci. 8, 829.
- [19] Massé, M. et al., 2016, Nat. Geosci. 9, 425.
- [20] Heinz, J. et al., 2016, Geophys. Res. Lett. 43, 4880.
- [21] Dundas, C. M. et al. 2017, Nat. Geosci. 10, 903.
- [22] Edwards, C. S. and Piqueux, S., 2016, Geophys. Res. Lett. 43, 8912.
- [23] Malin, M. C. and Edgett, K. S., 2000, Science 288, 2330.
- [24] Harrison, T. N. et al., 2015, Icarus 252, 236.
- [25] Kreslavsky, M. A. and Head, J. W., 2000, J. Geophys. Res. 105, 26695.
- [26] Piloget, C. and Forget, F., 2016, Nat. Geosci. 9, 65.
- [27] Mangold, N. et al., 2003, J. Geophys. Res. 108, 5027.
- [28] Miyamoto, H. et al., 2004, Geophys. Res. Lett. 31, L13701.
- [29] McKeown, L. E. et al., 2017, Sci. Rep. 7, 14181.
- [30] Malin, C. M. et al., 2006, Science 314, 1573.
- [31] Daubar, I. J. et al., 2013, Icarus 225, 506.
- [32] JeongAhn, Y. and Malhotra, R., 2015 Icarus 262, 140.
- [33] 宮本英昭ほか, 2016, 地学雑誌 125, 171.
- [34] Clifford, S. M., 1993, J. Geophys. Res. 98, 10973.
- [35] Farrell, W. M., 2009, Geophys. Res. Lett. 36, L15206.
- [36] Orosei, R. et al., 2018, Science 361, 490.
- [37] Hauck, S. A. and Phillips, R. J., 2002, J. Geophys. Res. 107, 5052.
- [38] Plesa, A. C. et al., 2016, J. Geophys. Res. 121, 2386.
- [39] Dundas, C. M. et al., 2018, Science 359, 199.
- [40] Souness, C. et al., 2012, Icarus 217, 243.

- [41] Holt, J. W., 2005, *Science* 322, 1235.
- [42] Parsons, R. and Holt, J., 2016, *J. Geophys. Res. Planets* 121, 432.
- [43] Oehler, D. Z. and Etiope, G., 2017, *Astrobiology* 17, 1233.
- [44] Webster, C. R. et al., 2015, *Science* 347, 415.
- [45] Webster, C. R. et al., 2018, *Science* 360, 1093.
- [46] Mumma, M. J. et al., 2009, *Science* 323, 1041.
- [47] 石丸亮ほか, 2012, *地質学雑誌* 118, 664.
- [48] Hemmi, R. and Miyamoto, H., 2017, *Prog. Earth Planet. Sci.* 4, 1.
- [49] Komatsu, G. et al., 2011, *Planet. Space Sci.* 59, 169.
- [50] Dundas, C. M. and McEwen, A. S., 2015, *Icarus* 254, 213.
- [51] Hemmi, R. and Miyamoto, H., 2018, *Geosciences* 8, 152.
- [52] 小松吾郎, 2012, *地質学雑誌* 118, 597.